University of Cincinnati

Date: 7/18/2016

I, Charles P Williams, hereby submit this original work as part of the requirements for the degree of Master of Science in Aerospace Engineering.

It is entitled:

Low Pressure Turbine Flow Control with Vortex Generator Jets

Student's name: **Charles P Williams**

This work and its defense approved by:

Committee chair: Kirti Ghia, Ph.D.

Committee member: Rolf Sondergaard, Ph.D.

Committee member: Shaaban Abdallah, Ph.D.

Committee member: Urmila Ghia, Ph.D.

UNIVERSITY OF Cincinnati

21074

Low Pressure Turbine Flow Control with Vortex Generator Jets

by

Charles Phillip Michael Williams

B.S., University of Cincinnati, 2010

A thesis submitted to the
Division of Research and Advanced Studies
of the University of Cincinnati

in partial fulfillment of the
requirements for the degree of

MASTER OF SCIENCE

in the Department of Aerospace Engineering and Engineering Mechanics
of the College of Engineering and Applied Science

Committee Chair: Dr. Kirti N. Ghia

15 July 2016

Abstract

In an aircraft engine at high altitude, the low-pressure turbine (LPT) section can experience low-Reynolds number (Re) flows making the turbine blades susceptible to large separation losses. These losses are detrimental to the performance of the turbine and lead to a roadblock for "higher-lift" blade designs. Accurate prediction of the separation characteristics and an understanding of mitigation techniques are of the utmost importance. The current study conducts simulations of flow control techniques for the Air Force Research Laboratory (AFRL) L2A turbine blade at low-Re of 10,000 based on inlet velocity and blade axial chord. This blade was selected for its "high-lift" characteristics coupled with massive separation on the blade at low-Re which provides an excellent test blade for flow control techniques. Flow control techniques involved various configurations of vortex generator jets (VGJs) using momentum injection (i.e. jet blowing). All computations were executed on dual-topology, multi-block, structured meshes and incorporated the use of a parallel computing platform using the message passing interface (MPI) communications. A high-order implicit large eddy simulation (ILES) approach was used in the simulations allowing for a seamless transition between laminar, transitional, and turbulent flow without changing flow solver parameters.

A validation study was conducted involving an AFRL L1A turbine blade which showed good agreement with experimental trends for cases which controlled separation in the experiments. The same cases showed good agreement between different grid sizes. The differences between experimental and numerical results are largely attributed to differences in the setup. That is, the simulation did not include freestream turbulence or wind-tunnel wall effects.

The flow control study conducted for the L2A blade showed a small degree of separation control for jets placed just downstream (DS) of the separation point. A limited study was conducted with jets moved upstream (US) of the natural separation point which showed an increase in effectiveness for one of the VGJs. This indicates a sensitivity of VGJ location relative to the point of separation. For the DS VGJs, separation control, increased as blowing ratio (BR) was increased and jet blowing frequency (F^+) decreased. The increase in jet efficacy with decreasing F^+ was unexpected and is mostly attributed to the jets being downstream of the separation location and having a low duty cycle (10%). Turbulent kinetic energy frequency spectra also show the presence of jet harmonics in the flow downstream of the best performing VGJs which dramatically increased in power when the VGJ was moved upstream. The most effective jet found in this study had $BR = 3.0$, $F^+ = 3.02$, and was located at $x/C_x = 0.53$. This VGJ provided a 42.1% reduction in normalized integrated wake loss.

One follow-on simulation was conducted taking the most effective VGJ and increasing the blowing ratio from $BR = 3.0$ to 8.0. This provided a decrease in the amount of separation, nearly eliminating separation with only a small separation bubble remaining. This VGJ was able to provide a 42.8% reduction in normalized integrated wake loss.

This work was conducted in coordination with the AFRL and has been approved for public release, case number: 88ABW-2016-1657.

Acknowledgements

I take this opportunity to express my sincerest gratitude to my faculty advisor, Dr. Kirti "Karman" Ghia. His guidance, patience, and encouragement largely made this thesis possible. The many conversations we had will be reflected upon beyond my academic career into my professional and personal life.

Additional thanks goes to several individuals that have helped tremendously in my understanding of the subject matter in this thesis. Many thanks go to Drs. Rolf Sondergaard and Eric Lyall of AFRL for helping me to understand the physical nature of turbine flow and Dr. Sondergaard in particular for agreeing to be on my committee and providing necessary computational resources to conduct this work. Thanks are in order for Dr. Urmila Ghia and Dr. Shaaban Abdallah for agreeing to be on my committee. Dr. Urmila Ghia also provided some of my earliest education on CFD which was a very enlightening experience. Thanks to Dr. Donald Rizzetta of AFRL and Dr. Ralph Volino of the U.S. Naval Academy for additional understanding of flow solver setup and experimental setup for the study. Also, my fellow graduate student William VonHagen provided many long discussions about numerical setup which proved invaluable. Finally, my co-worker John Roberts also provided many hints and techniques for software debugging and acted as a sounding board for many ideas.

Numerous organizations are also to thank for making this research possible. First and foremost, the Dayton Area Graduate Studies Institute for providing the opportunity to collaborate with AFRL scientists on this work and providing funding for my graduate studies. Secondly, the Air Force Research Laboratory for access to scientist knowledge and computer resources for simulations. Lastly, the Ohio Space Grant Consortium for additional funding for my graduate studies.

Finally, I must thank my family and friends for their continued support in this endeavor. My parents instilled a sense of curiosity about the physical world which has served me well. Without them I would not be who I am today. Foremost, I must express my greatest thanks to my wife Rachel and son Gale. It is their love and devotion which motivates me and helps me keep sight of what is important in life. I love you both dearly.

Table of Contents

List of Figures

List of Tables

Nomenclature

Roman Symbols

$a_1,\ a_2,\ a_3$	Direction cosines
$h_1,\ h_2,\ h_3$	Scale factors of curvilinear coordinate transformation
C_x	Axial Chord Length
E_t	Non-dimensional total specific energy
$F_I,\ G_I,\ H_I$	Invsicid flux vectors
$F_V,\ G_V,\ H_V$	Viscous flux vectors
R	Specific Gas Constant
J	Jacobian of the coordinate transformation
M	Mach Number
$\Delta s^+,\ \Delta n^+,\ \Delta z^+$	Streamwise, normal, and spanwise mesh spacing in wall units
M_∞	Reference Mach number, $U_\infty/\sqrt{\gamma R T_\infty}$
$\widehat{U},\ \widehat{V},\ \widehat{W}$	Physical contravariant velocity components
Pr	Prandtl Number
F^+	VGJ non-dimensional pulsing frequency, fC_x/U_{in}

F^+_∞	VGJ non-dimensional pulsing frequency based on reference velocity, fC_x/U_∞
F^+_{ssj}	VGJ non-dimensional pulsing frequency based on suction surface arclength and average freestream velocity from VGJ to trailing edge, fL_{ssj}/U_{ave}
Q	Vector of dependent variables
q_i	Heat flux vector
Re_{in}	Reynolds Number at the domain inlet
Re_∞	Reference Reynolds Number, $\rho_\infty U_\infty C_x/\mu_\infty$
Re	Reynolds Number
L_{ssj}	Suction surface length from VGJ to trailing edge
T	Non-dimensional static temperature
t	Non-dimensional time
E_ω	Turbulent Kinetic Energy Frequency Spectra
U	Non-dimensional velocity magnitude
U_{ave}	Averaged freestream velocity from VGJ to trailing edge
U_{in}	Average velocity magnitude at domain inlet
U_{jet}	Maximum velocity magnitude of VGJ
U_{local}	Local freestream velocity at VGJ location
$\widetilde{U},\ \widetilde{V},\ \widetilde{W}$	Contravariant velocity components

$u,\ v,\ w,$	Non-dimensional Cartesian velocity components in the x, y, z directions
Z_w	Incompressible Zweifel coefficient

Greek Symbols

α_1	Freestream pitch angle with respect to turbine axial direction
β_1	Freestream side-slip angle with respect to turbine axial direction
α_f	FDL3DI filter free parameter
γ	Ratio of specific heats, 1.4 for air
$\xi_t,\ \xi_x,\ \xi_y,\ \xi_z$ $\eta_t,\ \eta_x,\ \eta_y,\ \eta_z$ $\zeta_t,\ \zeta_x,\ \zeta_y,\ \zeta_z$	Grid metrics of coordinate transformation
μ	Non-dimensional molecular viscosity coefficient
θ	VGJ pitch angle
ρ	Non-dimensional density
ϕ	VGJ skew angle
τ_{ij}	Stress tensor
$\xi,\ \eta,\ \zeta$	Computational coordinates

Superscripts

$*$	Dimensional quantity
$'$	Fluctuating Component
$\overline{\ }$	Time-averaged quantity

Subscripts

$(\phi)_{x_i}$	Derivative of ϕ with respect to x_i
∞	Dimensional reference quantity
t	Total Quantity

Acronyms

AFRL	Air Force Research Laboratory
B, BR	Blowing Ratio, U_{jet}/U_{local}
DNS	Direct Numerical Simulation
DC	Jet Duty Cycle
FSTI	FreeStream Turbulence Intensity
ILES	Implicit Large Eddy Simulation
LPT	Low Pressure Turbine
MILES	Monotonically Integrated Large-Eddy Simulation
MPI	Message Passing Interface
RANS	Reynolds Averaged Navier-Stokes
SGS	Subgrid-Scale
URANS	Unsteady Reynolds Averaged Navier-Stokes
VGJ	Vortex Generator Jet
WPAFB	Wright-Patterson Air Force Base

Chapter 1

Introduction

The gas turbine engine has been one of the most important inventions of the 20th century. Its basic development occurred during the Second World War with parallel development between Hans von Ohain in Germany and Frank Whittle in England. The first jet engine propelled aircraft took flight on 27 August 1939 powered by a von Ohain engine, and followed closely by a Whittle engine powered aircraft on 15 May 1941 (Saravanamuttoo et al., 2009). Initial practical applications were for military aircraft with subsequent developments allowing for important advances in the military and civil vehicle propulsion industries. This has greatly benefited aircraft propulsion, but it has also provided great advances for power generation.

In the aviation industry, there has been a trend toward larger bypass-ratio turbofan engines putting increased demands on the Low-Pressure Turbine (LPT) which powers the large bypass fan. Howell et al. (2002) reported that the fan of a high-bypass-ratio turbofan produces up to 80% of the engine thrust and can be up to one-third of the total engine weight. Thus, the LPT is a significant driver in engine design from engine efficiency, cost, and weight perspectives. Typically, a 1% increase in LPT efficiency can increase overall engine efficiency by 0.7-0.9% (Wisler, 1998). Past research in LPT aerodynamics has resulted in efficiency increases of only 10% to reach current efficiencies of over 90%, as claimed by Howell et al. (2002). Gas turbine technology, the LPT in particular, has reached a position at which further increases in efficiency have become increasingly difficult.

1.1 Motivation

One avenue to improve the efficiency of LPTs is reducing weight, which can provide many benefits both to airlines and engine manufacturers. An approach to weight reduction is reducing the LPT blade count. This requires each blade to carry a greater load and underlies the motivation in recent years for creating turbine blades with "high-lift" characteristics. However, to achieve greater aerodynamic loads requires a highly curved airfoil shape which has the potential for very strong adverse pressure gradients on the suction surface of the blade. These strong adverse pressure gradients make the blade more susceptible to separation. This separation is particularly problematic at high altitudes where lower air density results in a lower Reynolds Number (Re) creating viscous boundary layers on the leading section of the blade. Mayle (1991), and Sharma et al. (1994) have shown that separation bubbles can lead to loss of lift and aerodynamic losses on the LPT blade. These losses can be very large in the case that the separation bubble never reattaches forming a completely separated boundary layer. Murawski et al. (1997), Dorney and Ashpis (1998) both documented severe drops in efficiency at high altitudes due to the separation losses on an LPT blade. A component efficiency drop on the order of 2 percent may occur between takeoff and cruise conditions, due to the lower-Reynolds numbers at altitude for large commercial transport engines, and could be as large as 7 percent for small military engines at high altitude, as stated by Volino and Hultgren (2001). Maintaining the "high-lift" aspects of these blades, while controlling or eliminating the losses associated with separated flow, is crucial for improvements to engine design. This creates the motivation for the current study in which flow control techniques are investigated for improved low-Re performance.

1.2 Past LPT Flow Research

Separation and separated flow transition have been studied extensively in the literature. Some experimental investigations include Volino (2010), Volino and Hultgren (2001), McQuilling et al. (2010), and Halstead et al. (1997). During takeoff and landing the LPT section of the engine experiences high-Reynolds numbers, but during cruise, the Reynolds numbers decrease significantly. In general, the studies mentioned above show these low-Reynolds numbers coupled with the strong acceleration of flow on the leading section of the turbine blade keeps the boundary layer thin and laminar, despite the fact there are elevated levels of freestream turbulence. When separation does occur, it is usually just downstream of the suction peak (Volino et al., 2009). This divides the flow into two regions. The separation bubble is a region of slow recirculation; comparatively, above this is the separated boundary layer or free shear layer. Transition usually occurs in this shear layer promoting rapid mixing and entrains high momentum fluid often causing the boundary layer to reattach. Bons et al. (2008) and Volino (2008) both discovered that with highly loaded LPT blades, transition may not be enough to cause reattachment. Figure 1.1 on the following page shows a diagram of a typical laminar separation bubble.

There have also been multiple numerical studies into the flow behavior of an LPT cascade. Dorney and Ashpis (1998) used a viscous, unsteady quasi-three-dimensional Navier-Stokes analysis to study the models available for simulating low-Reynolds number flows and to also investigate the effects of Reynolds number variation on the performance of LPT blade rows. Their simulations incorporated the use of two turbulence models. The first model was a two-layer algebraic turbulence model based

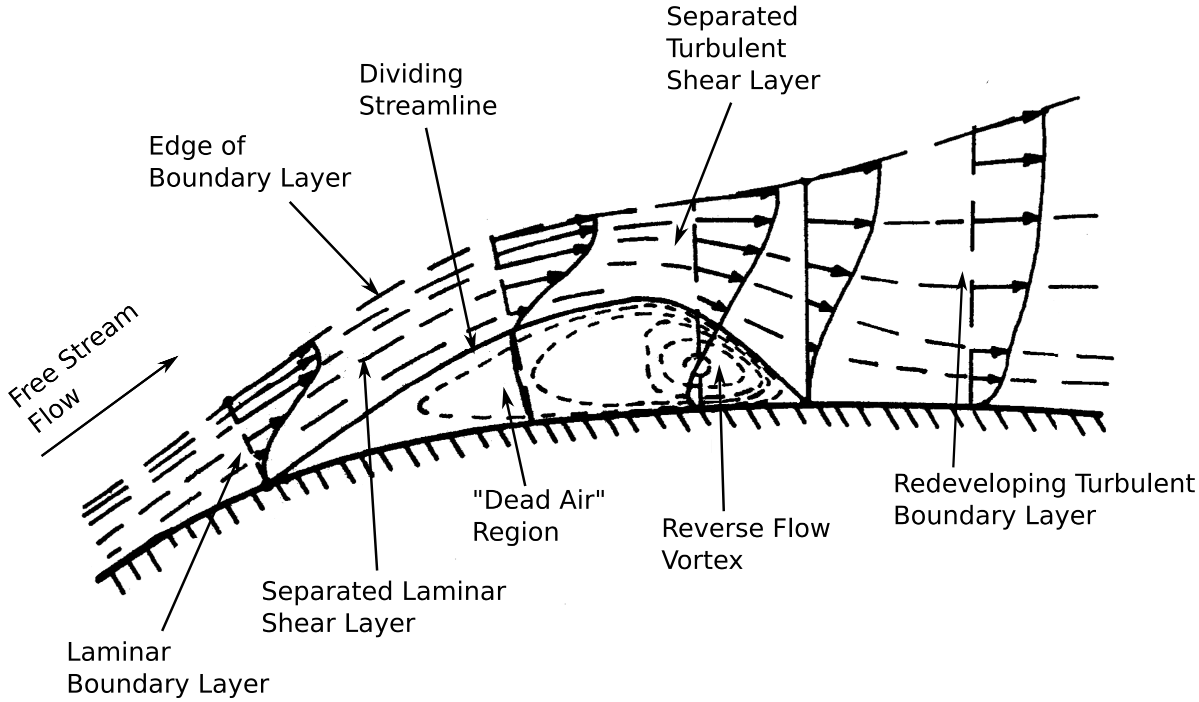

Figure 1.1: Typical Laminar Separation Bubble Behavior (after Horton, 1968)

on the work of Baldwin and Lomax (1978). The second model was a two-equation $k-\epsilon$ turbulence model based on the work of Towne et al. (1993) along with the low-Reynolds number approximation of Chien (1982). The natural transition was modeled using the transition model of Abu-Ghannam and Shaw (1980). The results of this study showed that the predicted losses and efficiency are highly dependent on the assumed state of the boundary layers (i.e. laminar, transitional, or turbulent). The transitional simulations also indicated that the location of transition was influenced by both the periodic and random unsteadiness in the flow.

Gross and Fasel (2008) used “coarse grid” direct numerical simulation (DNS), implicit large eddy simulation (ILES), and unsteady Reynolds averaged Navier-Stokes (URANS) models to predict Pack B, a research blade designed by Pratt and Whitney, flows. For sufficiently fine grids, the results of the DNS and ILES models were nearly identical. The coarse grid ILES caused the stronger numerical diffusion, which noticeably altered the flow dynamics. Some of the URANS models agreed but the authors cautioned that this success is likely a coincidence as the models are not tailored for separating transitional flows. DNS and ILES compared with experimental data provided moderate success; accordingly, these differences were attributed in part to differences between the experimental setup and the numerical simulations. Some of these setup differences may have included freestream turbulence and flow angle at the inflow and outflow.

Rizzetta and Visbal (2003*b*) conducted a thorough numerical investigation of subsonic low-Re LPT flow using the ILES technique. The ILES technique used by these authors is similar to the monotonically integrated large-eddy simulation (MILES) approach. Unlike MILES, which employs high-frequency filters built into numerical algorithms in order to provide implicit SGS models, ILES applies an explicit low-pass filter in lieu of the SGS model. They observed differences between the blade surface pressure distributions and attributed these discrepancies to details in the experimental configuration that were not accounted for in the simulations. They concluded that only large-eddy simulations obtained by high-order methods can be expected to provide an accurate description of the complex flow phenomena in LPT flows. RANS type approaches suffer from limitations and deficiencies of the turbulence models which prevent accurate calculation of transition and separation in the low-Re LPT flows.

1.3 Past Flow Control Research

Multiple techniques have been studied in attempting to reduce the separation losses in turbo-machinery applications. One approach to reducing these separation losses in LPT flows is designing blades which have pressure gradient profiles that are resistant to separation. This approach was used by Praisner and Clark (2007) in building a transition model. One example of such a design is the forward loading of an LPT blade. That is, the suction peak is located toward the front of the turbine blade's suction surface. Forward loading will expand the length of the suction surface in which an adverse pressure gradient exists. This effectively decreases the adverse pressure gradient over the suction surface at any given point, thus reducing the potential for separation. This also provides a long distance over which reattachment can occur in the case that separation does happen. However, there are some disadvantages of the front loaded blade design. Zhang et al. (2006) discussed that the longer region of turbulent flow on a forward loaded blade can cause increased profile losses. Wilson and Korakianitis (1998) noted that the front loaded design is more sensitive to small changes in geometry, and Weiss and Fottner (1995) showed that front loading can produce strong secondary flows and losses due to end-wall effects which generate strong transverse pressure gradients.

The passive blade pressure profile design can produce more desirable mid-span performance, but has the disadvantages discussed above. An aft-loaded blade profile can remedy the disadvantages of the fore-loaded blade but suffers in mid-span performance. This is the subject of the current study in which flow control devices are investigated in order to improve the mid-span loss characteristics of an aft-loaded blade at low-Reynolds numbers. This provides a blade that is resistant to separation and has low mid-span and end-wall losses over a range of low-Reynolds numbers. This same rationalization was used in the study of Bons et al. (2008) for investigating aft-loaded blade designs.

Nearly all separation control devices involve the introduction of longitudinal or stream-wise vortices in some form (Sondergaard, 2008). These vortices help to entrain the high momentum free-stream flow into the boundary layer thus energizing the boundary layer and reducing the separation inducing effects of the adverse pressure gradient. Early studies in flow control involved the use of passive techniques in external flows over airfoils to help prevent a stall. In external flow the point of separation has been often near the leading edge of the airfoil, however, for a turbine blade, the initial point of separation tends to occur near the point at which uncovered turning begins (Sondergaard, 2008) (i.e. the point where the adjacent blade no longer assists turning the flow). This separation point, usually occurs just downstream of the suction peak which has been shown to be about the optimal location for flow control devices (Volino et al., 2011). Due to this fact, flow control devices are often implemented near the point of separation for a turbine blade.

Passive flow control techniques involve the permanent modification of the blade to promote the formation of vortices. These techniques do not require power, hence the name "passive." Passive devices have been shown to be effective by Bohl and Volino (2006), Volino (2003*a*), Rivir et al. (2000), and Lake (1999). Lake (1999) investigated dimples, V-grooves, and boundary layer trips as passive control devices. Subsequently, he found that dimples were the most effective control device. Although these passive techniques are successful at increasing efficiency at the low-Reynolds numbers and are simple in design, they have the undesirable effect of increasing viscous losses at higher Reynolds numbers that will be encountered during take-off and landing. To address these issues, active flow control techniques can be used that would allow them to be shut-off during high-Re conditions and only activated when needed. Active control also has the potential of close-loop feedback control for more robust control authority.

1.3.1 Active Flow Control Research

The literature contains many examples of active flow control. Some of these techniques that have been applied to the LPT problem include plasma actuators (Huang et al., 2003), synthetic jets (Volino, 2003*b*), and vortex-generator jets (VGJs) (Bons et al., 1999). VGJs were introduced by Johnston and Nishi (1999) to control separation in a turbulent boundary layer. This methodology incorporates spanwise arrays of "small, skewed, and pitched jets from holes in the surface." Their study showed that the VGJs produced longitudinal streamwise vortices downstream of the jet injection site in a manner similar to solid vortex generators. They were able to substantially reduce the separated flow in their study. Figure 1.2 contains a diagram of the experimental setup for a VGJ. The most effective VGJs enter the boundary layer at shallow pitch angles (30 to 45 degrees) relative to the wall and a high skew angle (45 to 90 degrees) relative to the main flow Volino et al. (2009). VGJs have been successfully implemented for LPT flow control by many researchers. Bons et al. (2001) incorporated the use of pulsed VGJs and found them comparable to their steady counterpart. This allows for economical use of the bleed air required to power the VGJs. Continuing on the success of the pulsed VGJ, they are the subject of this study.

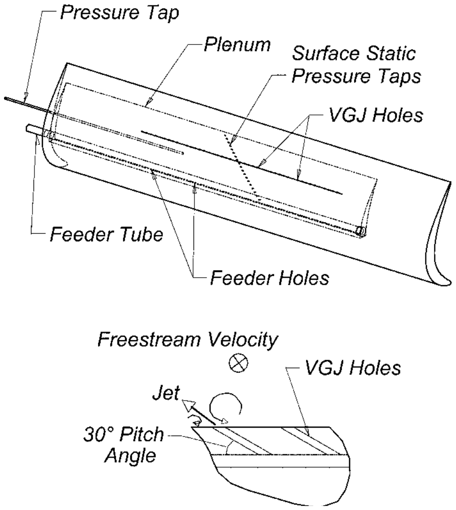

Figure 1.2: Experimental setup of Vortex Generator Jet (after Bons et al., 2001)

Numerical studies of LPT flow control with VGJs have also shown promising results. Gross and Fasel (2007) investigated both pulsed VGJs and harmonic blowing through a slot. Both techniques were shown to successfully control separation with the harmonic blowing being more effective than the pulsed VGJs.

Rizzetta and Visbal (2005) numerically investigated LPT flow control with pulsed VGJs. They incorporated an ILES approach and as in earlier studies noted that

Reynolds averaged Navier-Stokes (RANS) type approaches are inadequate for the study of this complex flow phenomena. The numerically simulated pulsed VGJs were able to mitigate the degree of separation, but there were differences when comparing to experimental results.

1.4 L1 and L2 Blade Series

Due to the interest in "high-lift" turbine blade designs, the Propulsion Directorate of the Air Force Research Laboratory (AFRL) has developed a series of LPT blades for studying low-Re flow. The blades have the same design gas angles as the Pratt & Whitney Pack B blade which has been investigated thoroughly. The first pair of blades, dubbed L1M and L1A (level one increase in lift, mid loaded and aft loaded, respectively), was designed with an incompressible Zweifel coefficient of 1.34, being 17% higher than the Zweifel coefficient of the Pack B blade ($Z_w = 1.15$). More recently, the second set of blades has been developed named L2F (McQuilling, 2007) and L2A. These blades have incompressible Zweifel coefficients of 1.59, being 38% higher than that of the Pack B blade, and maintain the same design gas angles of the Pack B. The L2F blade is front-loaded while the L2A blade is aft-loaded. As discussed earlier, aft-loaded blades have some advantages over front-loaded designs but suffer in mid-span performance at low-Re. With the incorporation of flow control, an aft-loaded blade can be more effective, so separation control of the L2A blade will be investigated in the current study.

1.5 Current Study Objectives

The literature review has shown that RANS type numerical simulations (Dorney and Ashpis, 1998, Gross and Fasel, 2008) suffer from limitations and deficiencies in turbulence modeling when simulating LPT flows. Rizzetta and Visbal (2005) reiterate this fact and look to advances in computer technology, which now enable the use of DNS and LES type approaches for simulating the complex LPT flow. Rizzetta and Visbal (2003b, 2005) both simulated complex LPT flow using a high-order LES type approach with moderate success when comparing to experimental results. The literature also shows that separation control of LPT flows is necessary for the "high-lift" turbine blade design. VGJs have been shown to be an effective means of controlling this separation both experimentally (Sondergaard et al., 2002 and Bons et al., 2001) and numerically (Rizzetta and Visbal, 2005), incorporating control for the Pratt and Whitney Pack-B research blade.

The present work seeks to use the ILES technique of Rizzetta and Visbal (2005) to simulate various VGJ configurations for the AFRL L2A turbine blade design at a low-Reynolds number. This work seeks to find the optimal jet configuration for this blade and will evaluate the flow physics of the problem in an effort to understand the complex fluid interaction of the VGJ. The ILES technique solves the Navier-Stokes equations directly without modeling any flow physics. This creates an important tie to the grid resolution, which now dictates the fidelity of the solution and accurate capture of flow separation and transition. The ILES approach is based on high-order compact schemes for spatial derivatives and Padé-type low-pass filtering for stability. The low-pass filter is used instead of an explicit sub-grid-scale (SGS) model for dissipation of the turbulent energy at the smallest flow scales.

A higher-order accurate, parallel, Chimera, ILES version of the FDL3DI (Gaitonde and Visbal, 1998) flow solver developed by AFRL is extended for the present application.

1.6 Organization of Thesis

This thesis is organized in the following manner. Chapter 1 beginning on page 1 has given a review of basic theory and methodologies having developed from seminal and contemporary studies. Chapter 2, beginning on the next page, gives details of the governing equations and numerical methodology that will be used for the current study. Chapter 3, beginning on page 47, contains information about the specific numerical approach used in this study. Chapter 4, beginning on page 61, compares preliminary results against experimental data for a grid study and flow solver validation. Chapter 5, beginning on page 92, presents results and discussion about the current L2A flow control study. Finally, Chapter 6, beginning on page 158, identifies significant findings from this study and recommendations for future research.

Chapter 2

Governing Equations and Solution Methodology

This chapter describes the mathematical formulation of the problem and the methodologies used in the current flow solver FDL3DI. The flow solver FDL3DI is a higher-order accurate, parallel, Chimera, ILES solver from AFRL at Wright-Patterson Air Force Base (WPAFB). FDL3DI has been used extensively for steady and unsteady fluid flow problems, including but not limited to, the following: Gordnier and Visbal (1998), Gordnier (1995), Rizzetta et al. (1999), Rizzetta et al. (2001), Rizzetta and Visbal (2002), Rizzetta et al. (2003), and Rizzetta and Visbal (2003*a*). For continuity, the following sections will describe the methodology used in FDL3DI for the current study.

2.1 Implicit LES

In LES, the flow problem under investigation is divided into two separate regions: large eddies containing most of the turbulent energy and the smallest scale eddies which are responsible for the dissipation of turbulent energy. The large scale eddies are difficult to model as they can vary considerably from one flow to another. Large scale unsteadiness is significant in problems that involve unsteady separation such as that in the current study. LES computes these large scale eddies directly while modeling the unresolved small-scale structures using a subgrid-scale (SGS) turbulence model. The small-scale eddies are believed to be isotropic and possess universal characteristics in turn making them amenable to modeling. LES provides a nice methodology between RANS and DNS type computations, addressing limitations of each of these approaches. The first and most popular SGS model was obtained by Smagorinsky (1963) and is commonly used in LES computations. LES formulations with SGS models contain additional terms in the Navier-Stokes equations referred to as the SGS stress tensor. These terms are obtained through a filtering operation, unlike the averaging operation used in RANS equations.

ILES differs from LES in that no additional SGS terms appear in the governing Navier-Stokes equations. Dissipation at higher wave numbers is provided through a high-order (up to 10th order) Padé-type low pass spatial filter (Gaitonde et al., 1997) which is applied numerically to the computed solution at each time step. Poondru (2007) investigated the use of ILES, LES with Smagorinsky, and LES with dynamic Smagorinsky for an LPT flow problem and found no significant differences between the different models. This was attributed to the low-Re flow being simulated. Thus, ILES was used because it required less computational resources. Visbal and Gaitonde (1999) also found that this ILES approach was superior to the use of an explicit SGS model for maintaining both stability and accuracy on a stretched curvilinear mesh. This high-order filter method carries the promise of both accuracy and computational efficiency. This ILES technique has been incorporated into FDL3DI and has been successfully applied to LPT flow problems by Rizzetta and Visbal (2003*b*), Rizzetta and Visbal (2005), Poondru (2007), and others.

2.2 Governing Equations

The FDL3DI solver using the ILES scheme solves the three-dimensional, unsteady, unfiltered, compressible Navier-Stokes equations expressed in curvilinear coordinates cast in the following non-dimensional conservative form:

$$\frac{\partial}{\partial t}\left(\frac{Q}{J}\right)+\frac{\partial F_I}{\partial \xi}+\frac{\partial G_I}{\partial \eta}+\frac{\partial H_I}{\partial \zeta}=\frac{1}{Re_\infty}\left[\frac{\partial F_V}{\partial \xi}+\frac{\partial G_V}{\partial \eta}+\frac{\partial H_V}{\partial \zeta}\right] \tag{2.1}$$

Here t is the time; $\xi,\ \eta,\ \zeta$ the computational coordinates; Q the vector of dependent variables; $F_I,\ G_I,\ H_I$ the inviscid flux vectors, and $F_V,\ G_V,\ H_V$ the viscous flux vectors. The vector of dependent variables is given as:

$$Q=\begin{bmatrix} \rho & \rho u & \rho v & \rho w & \rho E_t \end{bmatrix}^T \tag{2.2}$$

The inviscid flux vectors are given by:

$$F_I=\frac{1}{J}\begin{bmatrix} \rho\widetilde{U} \\ \rho u\widetilde{U}+\xi_x p \\ \rho v\widetilde{U}+\xi_y p \\ \rho w\widetilde{U}+\xi_z p \\ \rho E_t\widetilde{U}+\xi_{x_i}u_i p \end{bmatrix},\ G_I=\frac{1}{J}\begin{bmatrix} \rho\widetilde{V} \\ \rho u\widetilde{V}+\eta_x p \\ \rho v\widetilde{V}+\eta_y p \\ \rho w\widetilde{V}+\eta_z p \\ \rho E_t\widetilde{V}+\eta_{x_i}u_i p \end{bmatrix},\ H_I=\frac{1}{J}\begin{bmatrix} \rho\widetilde{W} \\ \rho u\widetilde{W}+\zeta_x p \\ \rho v\widetilde{W}+\zeta_y p \\ \rho w\widetilde{W}+\zeta_z p \\ \rho E_t\widetilde{W}+\zeta_{x_i}u_i p \end{bmatrix} \tag{2.3}$$

where:

$$\widetilde{U} = \xi_t + \xi_x u + \xi_y v + \xi_z w \tag{2.4}$$

$$\widetilde{V} = \eta_t + \eta_x u + \eta_y v + \eta_z w \tag{2.5}$$

$$\widetilde{W} = \zeta_t + \zeta_x u + \zeta_y v + \zeta_z w \tag{2.6}$$

$$E_t = \frac{T}{(\gamma - 1) M_\infty^2} + \frac{1}{2}\left(u^2 + v^2 + w^2\right) \tag{2.7}$$

In the expressions above, $u,\ v,\ w$ are the Cartesian velocity components, ρ the density, p the pressure, and T the temperature. Non-dimensionalization is shown in Eq. 2.13 on the following page. The viscous flux vectors are given by:

$$F_V = \frac{1}{J}\begin{bmatrix} 0 \\ \xi_{x_i}\tau_{i1} \\ \xi_{x_i}\tau_{i2} \\ \xi_{x_i}\tau_{i3} \\ \xi_{x_i}\left(u_j\tau_{ij} - q_i\right) \end{bmatrix}, G_V = \frac{1}{J}\begin{bmatrix} 0 \\ \eta_{x_i}\tau_{i1} \\ \eta_{x_i}\tau_{i2} \\ \eta_{x_i}\tau_{i3} \\ \eta_{x_i}\left(u_j\tau_{ij} - q_i\right) \end{bmatrix}, H_V = \frac{1}{J}\begin{bmatrix} 0 \\ \zeta_{x_i}\tau_{i1} \\ \zeta_{x_i}\tau_{i2} \\ \zeta_{x_i}\tau_{i3} \\ \zeta_{x_i}\left(u_j\tau_{ij} - q_i\right) \end{bmatrix} \tag{2.8}$$

where components of the heat flux vector and stress tensor are given by:

$$q_i = -\left[\frac{1}{(\gamma - 1) M_\infty^2}\right]\left(\frac{\mu}{Pr}\right)\frac{\partial \xi_j}{\partial x_i}\frac{\partial T}{\partial \xi_j} \tag{2.9}$$

$$\tau_{ij} = \mu\left(\frac{\partial \xi_k}{\partial x_j}\frac{\partial u_i}{\partial \xi_k} + \frac{\partial \xi_k}{\partial x_i}\frac{\partial u_j}{\partial \xi_k} - \frac{2}{3}\delta_{ij}\frac{\partial \xi_l}{\partial x_k}\frac{\partial u_k}{\partial \xi_l}\right) \tag{2.10}$$

Einstein summation notation is used to compactly represent $x,\ y,\ z$ as $x_i,\ i = 1, 2, 3$ and likewise for $\xi,\ \eta,\ \zeta$ as ξ_i. The Sutherland law for molecular viscosity:

$$\mu = T^{3/2}\left(\frac{1+S_1}{T+S_1}\right),\ \ S_1 = 0.38 \tag{2.11}$$

as well as the ideal gas law:

$$p = \frac{\rho T}{\gamma M_\infty^2} \tag{2.12}$$

were also used along with Stokes' hypothesis for the bulk viscosity coefficient. This closes the Navier-Stokes equations and provides the appropriate governing equations. These equations represent the original, unfiltered Navier-Stokes equations without changes for laminar, transitional, or turbulent boundary layer regions. This creates a seamless set of equations for the current problem which presents all three of these flow regions.

2.3 Non-dimensionalization

All flow variables used in the equations in the preceding section are considered to be non-dimensional unless otherwise specified. In the present study, the non-dimensionalization is given as follows (superscript * represents dimensional quantities)

$$\begin{gathered}
x = \frac{x^*}{C_x} \qquad y = \frac{y^*}{C_x} \qquad z = \frac{z^*}{C_x} \qquad t = \frac{t^* U_\infty}{C_x} \\
u = \frac{u^*}{U_\infty} \qquad v = \frac{v^*}{U_\infty} \qquad w = \frac{w^*}{U_\infty} \quad \mu = \frac{\mu^*}{\rho_\infty U_\infty C_x} \\
\rho = \frac{\rho^*}{\rho_\infty} \quad p = \frac{p^*}{\rho_\infty U_\infty^2} \quad T = \frac{T^*}{T_\infty}
\end{gathered} \tag{2.13}$$

2.4 Numerical Discretization

The current flow solver, FDL3DI, solves Eq. 2.1 on page 14 in time using the implicit, approximate-factorization algorithm of Beam and Warming (1978). This algorithm belongs to the class of Alternating-Direction Implicit (ADI) schemes, developed by Lindemuth and Killeen (1973) and McDonald and Briley (1975), where implicit methods are used for time integration. After the discretization of the governing partial differential equations, the ADI method applies one-dimensional sweeps in each spatial direction which efficiently solves the system of algebraic equations. This time integration algorithm is augmented with Newton-like subiterations to improve temporal accuracy and stability. Spatial derivatives are evaluated using the high-order, accurate, compact, central-difference scheme of Lele (1992). These compact difference schemes are non-dissipative which generates numerical instabilities. To improve numerical stability a high-order, non-dispersive spatial filter (up to 10th order) is used (Gaitonde et al., 1997). The following sections will describe in brief the time integration, spatial discretization, and spatial filtering. A more detailed treatment of the high-order compact schemes and spatial filtering can by found in the work of Gaitonde and Visbal (1998).

2.4.1 Time Integration

As mentioned before, time integration is accomplished through the implicit approximate-factorization algorithm of Beam and Warming (1978), augmented with Newton-like subiterations to help maintain second-order temporal accuracy. The implicit system is written in delta form as

$$\begin{aligned}&\left[\frac{1}{J}+\phi^{i}\Delta t\delta_{\xi 2}\left(\frac{\partial F_I^p}{\partial Q}-\frac{1}{Re_\infty}\frac{\partial F_V^p}{\partial Q}\right)\right]J\times\left[\frac{1}{J}+\phi^{i}\Delta t\delta_{\eta 2}\left(\frac{\partial G_I^p}{\partial Q}-\frac{1}{Re_\infty}\frac{\partial G_V^p}{\partial Q}\right)\right]J\\ &\times\left[\frac{1}{J}+\phi^{i}\Delta t\delta_{\zeta 2}\left(\frac{\partial H_I^p}{\partial Q}-\frac{1}{Re_\infty}\frac{\partial H_V^p}{\partial Q}\right)\right]\Delta Q=-\phi^{i}\Delta t\Bigg[\frac{(1+\phi)\,Q^p-(1+2\phi)\,Q^n+\phi Q^{n-1}}{J\Delta t}+\\ &\delta_\xi\left(F_I^p-\frac{1}{Re_\infty}F_V^p\right)+\delta_\eta\left(G_I^p-\frac{1}{Re_\infty}G_V^p\right)+\delta_\zeta\left(H_I^p-\frac{1}{Re_\infty}H_V^p\right)\Bigg]\end{aligned} \tag{2.14}$$

where $\phi^i = \frac{1}{1+\phi}$, with $\phi = 0$ and $\phi = 1/2$ for the first-order, Euler implicit and second-order, three-point backward schemes, respectively. The present computations used the second-order formulation for time integration. Newton-like subiterations are incorporated to help maintain temporal accuracy and reduce errors that arise from linearization, factorization, diagonalization and explicit implementation of the boundary conditions. Subiteration level in Eq. 2.14 is indicated by the superscript p, with $\Delta Q = Q^{p+1} - Q^p$, $Q^p = Q^n$ for $p = 1$, and $Q^p = Q^{n+1}$ as $p \to \infty$. For the current study, three subiterations were used at each time step. The left-hand side of the algorithm represents the implicit portion of the algorithm which uses second-order central differences for the spatial derivatives and incorporates non-linear artificial dissipation to improve stability (Jameson et al., 1981). The implicit algorithm is diagonalized to improve efficiency (Pulliam and Chaussee, 1981). The spatial derivatives on the right-hand side of Eq. 2.14 are evaluated with the high-order compact difference schemes discussed in Section 2.4.2 and are indicated by the δ operator with differentiation in each of the computational coordinates.

2.4.2 Spatial Discretization

The spatial derivatives on the right-hand side of Eq. 2.14 are discretized with the high-order, accurate, compact difference schemes of Lele (1992). These schemes are capable of achieving spectral-like resolution. Consider a one-dimensional mesh with N nodes, evenly spaced, as depicted in Fig. 2.1 on the next page. For a body-fitted mesh an appropriate coordinate transformation, $\xi = \xi(x)$, is required to transform the physical coordinates into the evenly spaced computational coordinates. Also, let $\phi = \phi(\xi)$ represent any scalar such as a metric, flux component, or flow variable. A five-point stencil is required for a 6th-order accurate scheme and can be maintained up to the 3rd node from the boundary (3, or $N-2$ in Fig. 2.1). Thus, boundary points are treated specially from the interior points. These schemes are referred to as "compact" since the stencil requirement is one node less than the order of accuracy. The following two sections will briefly describe the treatment of the interior and boundary points. More detail can be found in Gaitonde and Visbal (1998).

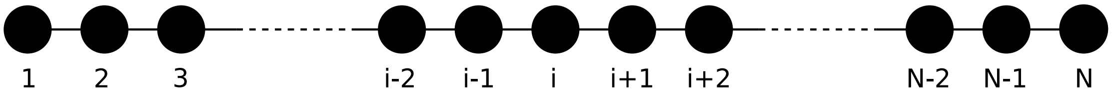

Figure 2.1: One-dimensional mesh of N points for spatial discretization stencil

Each of the formulas described in the following two sections are used to calculate the derivatives of the inviscid flux terms by first forming the fluxes at each node then differentiating with the selected formula. For viscous flux terms, the primitive variables, u, v, w, and T, are first differentiated to form the components of the heat flux vector and stress tensor, Equs. 2.9 and 2.10, respectively. The same difference scheme is then applied again in order to calculate the viscous flux derivatives.

2.4.2.1 Interior Points

The central difference scheme for interior points can be expressed in general terms as follows:

$$\alpha\left(\frac{\partial\phi}{\partial\xi}\right)_{j-1} + \left(\frac{\partial\phi}{\partial\xi}\right)_{j} + \alpha\left(\frac{\partial\phi}{\partial\xi}\right)_{j+1} = a\left(\frac{\phi_{j+1}-\phi_{j-1}}{2}\right) + b\left(\frac{\phi_{j+2}-\phi_{j-2}}{4}\right) \quad (2.15)$$

where α, a and b determine the accuracy of the scheme. Up to 6th order accuracy can be obtained through appropriate selection of these coefficients. In order to select these coefficients, Taylor series approximations are made around point j then inserted into Eq. 2.15 and appropriate terms are set equal to zero. This will produce the following system of equations (Gaitonde and Visbal, 1998):

$$\begin{aligned} \mathcal{O}\left(h^2\right): &\quad 1 - a + 2\alpha - b &= 0 \\ \mathcal{O}\left(h^4\right): &\quad -a + 6\alpha - 4b &= 0 \\ \mathcal{O}\left(h^6\right): &\quad -a + 10\alpha - 16b &= 0 \end{aligned} \tag{2.16}$$

where satisfying the first equation will produce a 2nd order scheme and satisfying the next equation, as well as the previous, will increase the accuracy up to 6th order.

Equation 2.16 allows for both explicit and implicit schemes by appropriately selecting $\alpha = 0$ and $\alpha \neq 0$, respectively. Selection of $\alpha = 0$ will decouple the derivative values from each other around point j and allows for two explicit schemes. Solving only the first equation of Eq. 2.16 will produce a second order, explicit scheme (E2, "E" referring to explicit) while additionally solving the second equation will produce a fourth order, explicit scheme (E4). If $\alpha \neq 0$, then a tridiagonal system must be solved for the implicit equation. This allows for the solution of a fourth order, implicit scheme (C4, "C" referring to compact) and a sixth order, implicit scheme (C6). All of these spatial schemes are centered schemes which are non-dissipative, producing dispersive errors exclusively. An analysis of the error properties of this scheme is carried out in Lele (1992) and Gaitonde and Visbal (1998).

Table 2.1 on the following page contains a summary of the coefficients used for the various interior schemes along with the corresponding stencil size and order of accuracy.

Modified wave number analysis can be used to analyze how well each of these schemes resolve the various wave numbers present in the flow solution. For this

Table 2.1: Coefficients for interior compact difference schemes

Scheme	α	a	b	Stencil	$\mathcal{O}(h)$
E2	0	1	0	3	2
E4	0	$4/3$	$-1/3$	5	4
C4	$1/4$	$3/2$	0	3	4
C6	$1/3$	$14/9$	$1/9$	5	6

analysis, a discrete spectral representation is considered for the function in question, ϕ. Assuming a domain length of L, at N equally spaced points the following discrete Fourier series can be defined (where $i = \sqrt{-1}$):

$$\phi_j = \frac{1}{N}\sum_{k=0}^{N-1} c_k e^{2\pi ikj/N} \tag{2.17}$$

Now define the wave number $\omega = {}^{2\pi k}/_{L}$, $\xi_j = j\Delta\xi$, and $\Delta\xi = {}^{L}/_{N}$. Reform the equation above and drop the summation for simplicity (considering only one Fourier component):

$$\phi_j = c_k e^{i\omega\xi_j} \tag{2.18}$$

where the exact derivative can be solved as:

$$\frac{\partial\phi_j}{\partial\xi} = i\omega c_k e^{i\omega\xi_j} = i\omega\phi_j \tag{2.19}$$

Modified wave number analysis can be used to evaluate how well a particular finite-difference operator, δ_ξ, approximates the exact derivative using the following equation:

$$\delta_\xi\phi_j = i\omega^*\phi_j \tag{2.20}$$

where $i\omega^*$ represents the modified wave number. The modified wave number is a complex number where the imaginary component represents dispersive errors in the finite-difference scheme, while the real component represents amplification errors. Using the additional definition:

$$\delta_\xi \phi_{j+m} = i\omega^* c_k e^{i\omega(j+m)\Delta\xi} = i\omega^* e^{mi\omega\Delta\xi} c_k e^{i\omega\xi_j} = i\omega^* e^{mi\omega\Delta\xi}\phi_j \tag{2.21}$$

Equs. 2.18, 2.20, and 2.21 can be substituted into Eq. 2.15 in order to analyze the modified wave number. After algebraic manipulation, this results in the following modified wave number

$$i\omega^*(\omega) = 0 + i\frac{a\sin(\omega) + \frac{b}{2}\sin(2\omega)}{1 + 2\alpha\cos(\omega)} \tag{2.22}$$

This modified wave number only has an imaginary part, indicating that the interior spatial discretization schemes are all non-dissipative owing to the central-difference nature of these schemes. Figure 2.2 shows a plot of the modified wave number versus the exact wave number. How well a scheme follows the exact solution indicates how well it can resolve the wave numbers in the flow solution. The higher-order schemes lead to better resolution of the higher wave numbers. Deviation from the exact solution indicates dispersive errors in the finite-difference scheme.

2.4.2.2 Boundary Points

Near the boundaries the stencil and scheme must change in order to retain the tridiagonal form of the interior scheme. The general formula for the first boundary point (1 in Fig. 2.1) is:

$$\left(\frac{\partial\phi}{\partial\xi}\right)_1 + \alpha_1\left(\frac{\partial\phi}{\partial\xi}\right)_2 = a_1\phi_1 + b_1\phi_2 + c_1\phi_3 + d_1\phi_4 + e_1\phi_5 + f_1\phi_6 + g_1\phi_7 \tag{2.23}$$

Similar to the interior scheme, Taylor series approximations are made about the

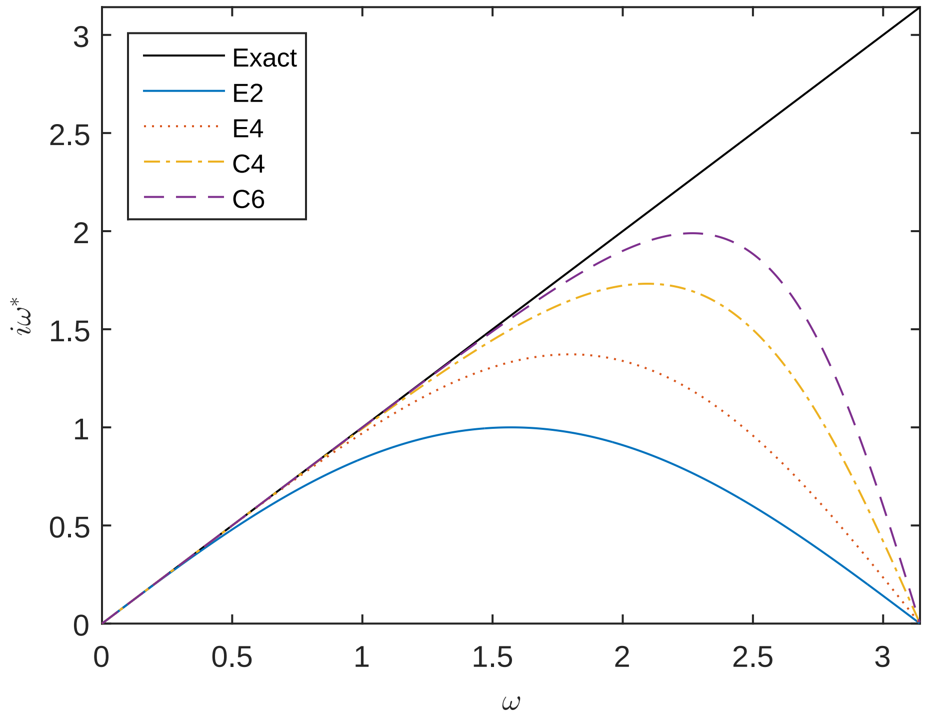

Figure 2.2: Interior Spatial Discretization Modified Wave Number

point 1 and inserted into Eq. 2.23. The resulting equations can be solved to develop the various schemes available at boundary point 1. These coefficients are shown in Table 2.2 on the next page.

The formula for the first point away from the boundary (2 in Fig. 2.1) is:

$$\alpha_{21}\left(\frac{\partial\phi}{\partial\xi}\right)_1+\left(\frac{\partial\phi}{\partial\xi}\right)_2+\alpha_{22}\left(\frac{\partial\phi}{\partial\xi}\right)_3=a_2\phi_1+b_2\phi_2+c_2\phi_3+d_2\phi_4+e_2\phi_5+f_2\phi_6+g_2\phi_7 \tag{2.24}$$

In the general sense, both sides of Eq. 2.24 are asymmetric about point 2. Applying Taylor series approximations to this equation, there are several possible solutions that depend on the relationship between α_{21} and α_{22}. Four possible relationships are given in Table 2.3 on the following page.

No methodical comparison has been made between these different methods, but

Table 2.2: Boundary Coefficients for Boundary Point 1

Scheme	α_1	a_1	b_1	c_1	d_1	e_1	f_1	g_1	$\mathcal{O}(h)$
E1	0	-1	1	0	0	0	0	0	1
E2	0	$-3/2$	2	$-1/2$	0	0	0	0	2
E3	0	$-11/6$	3	$-3/2$	$1/3$	0	0	0	3
E4	0	$-25/12$	4	-3	$4/3$	$-1/4$	0	0	4
E5	0	$-137/60$	5	-5	$10/3$	$-5/4$	$1/5$	0	5
E6	0	$-49/20$	6	$-15/2$	$20/3$	$-15/4$	$6/5$	$-1/6$	6
C2	1	-2	2	0	0	0	0	0	2
C3	2	$-5/2$	2	$1/2$	0	0	0	0	3
C4	3	$-17/6$	$3/2$	$3/2$	$-1/6$	0	0	0	4
C5	4	$-37/12$	$2/3$	3	$-2/3$	$1/12$	0	0	5
C6	5	$-197/60$	$-5/12$	5	$-5/3$	$5/12$	$-1/20$	0	6

Table 2.3: Possible relationships between α_{21} and α_{22}

Options	Relationship	Description
A	$\alpha_{21} = \alpha_{22} \neq 0$	This case makes the left-hand side of Eq. 2.24 symmetric.
B	$\alpha_{21} \neq \alpha_{22} \neq 0$	There is an extra degree of freedom, so the same stencil size can achieve one degree higher order of accuracy than in Option A.
C	$\alpha_{21} = 0,\ \alpha_{22} \neq 0$	This relationship will exclude the derivative at the actual boundary point.
D	$\alpha_{21} = \alpha_{22} = 0$	This produces an explicit scheme.

traditionally FDL3DI has been used with Option A, see Galbraith (2009). Thus, Option A will also be used in this study due to historical precedence. The coefficients for Option A are given in Table 2.4.

Table 2.4: Boundary Coefficient for Point 2 with Option A: $\alpha_{21} = \alpha_{22} \neq 0$

Scheme	α_{21}	α_{22}	a_2	b_2	c_2	d_2	e_2	f_2	g_2	$\mathcal{O}(h)$
AC4	$1/4$	$1/4$	$-3/4$	0	$3/4$	0	0	0	0	4
AC5	$3/14$	$3/14$	$-19/28$	$-5/42$	$6/7$	$-1/14$	$1/84$	0	0	5
AC6	$2/11$	$2/11$	$-20/33$	$-35/132$	$34/33$	$-7/33$	$2/33$	$-1/132$	0	6

For the second to last boundary point (point $N-1$ in Fig. 2.1) the general formula is very similar to that at the second boundary point:

$$\alpha_{M1}\left(\frac{\partial\phi}{\partial\xi}\right)_{N-2} + \left(\frac{\partial\phi}{\partial\xi}\right)_{N-1} + \alpha_{M2}\left(\frac{\partial\phi}{\partial\xi}\right)_{N} = a_M\phi_N + b_M\phi_{N-1} + c_M\phi_{N-2} + d_M\phi_{N-3} + e_M\phi_{N-4} + f_M\phi_{N-5} + g_M\phi_{N-6} \quad (2.25)$$

The same options that were available for point 2 can also be used here. Because of the similarities between Equs. 2.24 and 2.25, Table 2.4 can be used for assigning the coefficient values given the following modifications:

1. $\alpha_{M1} = \alpha_{22}$
2. $\alpha_{M2} = \alpha_{21}$
3. the signs of coefficients a through g are reversed, i.e. $a_M = -a_2$, $b_M = -b_2$, ...

The general formula for the last boundary point (point N in Fig. 2.1) is very similar to that at the first boundary point:

$$\alpha_N \left(\frac{\partial \phi}{\partial \xi}\right)_{N-1} + \left(\frac{\partial \phi}{\partial \xi}\right)_N =$$
$$a_N\phi_N + b_N\phi_{N-1} + c_N\phi_{N-2} + d_N\phi_{N-3} + e_N\phi_{N-4} + f_N\phi_{N-5} + g_N\phi_{N-6} \quad (2.26)$$

Due to the similarity with the same formula at the first boundary point, the coefficients in Table 2.2 can be used, given the following modifications:

1. $\alpha_N = \alpha_1$
2. the signs of each of the coefficients a through g are reversed, i.e. $a_N = -a_1$, $b_N = -b_1$, ...

2.4.3 Low Pass Spatial Filtering

The previous section covered the implementation of spatial discretization for the governing equations which address the issue of accuracy with the high-order, compact schemes. An equally important subject in a simulation is numerical stability. The spatial discretization schemes presented herein are central difference schemes which are non-dissipative but are subject to dispersive errors which can allow the growth of unstable high-frequency modes. Theoretical analysis of numerical stability is difficult to apply to practical engineering problems. Often this type of analysis is limited to simple cases such as linear governing equations, uniform meshes, and explicit time-integration techniques. None of these characteristics encompass the current problem.

Additionally, stability analysis rarely accounts for the implementation of physical boundary conditions. These boundary conditions typically involve making approximations to the physical flow; for example, the zero-pressure gradient ($\partial p/\partial n = 0$) is often imposed at solid walls. This condition is derived from boundary layer theory and is used quite extensively; however, this approximation can induce appreciable errors near points of flow separation and reattachment. Furthermore, this boundary condition is commonly implemented as $\partial p/\partial n \approx \partial p/\partial \eta = 0$, where η is the computational coordinate emanating from the wall and may not point along the true wall normal. The impact on the numerical stability of such approximations has not been well researched (Gaitonde and Visbal, 1998). Mesh quality can also play a vital role in the stability of the present scheme. Boundary conditions derived from a uniform mesh spacing have been shown to exhibit instability on body-fitted meshes (Jurgens and W., 1995) where mesh spacing is non-uniform.

The aforementioned difficulties preclude a theoretical treatment of the stability analysis of the current scheme. Stability is usually augmented through the addition of artificial damping, but in the current study, the conservative variables are passed through the non-dispersive, low-pass spatial filter of Gaitonde et al. (1997). This filter is applied to the solution vector of the conservative variables following each sub-iteration. These low-pass filters will only apply dissipation at the high modified wave numbers where the spatial discretization scheme is poorly resolved. This provides dissipation where needed, in contrast with artificially added dissipation which can introduce dissipation across a wide range of frequencies. This technique, which also provides the spatial filtering of the ILES method, has been shown to be superior in maintaining accuracy and stability on stretched curvilinear meshes by Visbal and Gaitonde (1999). These filters have been developed in keeping with the interior spatial discretization scheme and are limited to tridiagonal-based schemes with up to 10th order accuracy. The following two sections briefly describe the filtering technique. More detail can be found in Gaitonde and Visbal (1998).

2.4.3.1 Interior Points

The interior filter updates the value of ϕ with the filtered values, $\bar{\phi}$, according to the following equation:

$$\alpha_f \bar{\phi}_{j-1} + \bar{\phi}_j + \alpha_f \bar{\phi}_{j+1} = \sum_{n=0}^{N} \frac{a_n}{2} \left(\phi_{j+n} + \phi_{j-n}\right) \tag{2.27}$$

This equation will produce a $2N$-order accurate filter with a $2N+1$ sized stencil. Similar to the interior spatial discretization, this equation is generally implicit and tridiagonal. Using a similar Fourier series expansion of the function about j, as in Section 2.4.2.1, the ratio of the filtered function $\left(\bar{\phi}\right)$ to the function before the filter application (ϕ) can be derived. Using this approach the spectral function of the filter is:

$$SF\left(\omega\right) = \frac{\sum_{n=0}^{N} a_n \cos\left(n\omega\right)}{1 + 2\alpha_f \cos\left(\omega\right)} \tag{2.28}$$

This function represents the level of attenuation the filter will apply to a given wave number. The coefficients of Eq. 2.28 can now be determined in order to obtain the attenuation of high under-resolved wave numbers. The equation has $N+2$ unknowns (i.e. α_f, a_0, a_1, ..., a_N). To obtain these coefficients, the highest frequency mode is first eliminated by enforcing $SF\left(\pi\right) = 0$ (see Lele, 1992 and Vichnevetsky, 1974). The remaining $N+1$ equations can be derived by matching Taylor series approximation of ϕ about point j. Eq. 2.27 is symmetric indicating that $SF\left(\omega\right)$ is real and only modified the amplitude of each wave component. Odd-order terms cancel, leaving only filters with increasing even-ordered accuracies. The resulting system of equations could be solved uniquely, but instead the parameter α_f is allowed to vary offering a single degree of freedom. This allows the freedom to de-couple the left-hand side of Eq. 2.27 ($\alpha_f = 0$), thus producing an explicit filter. An upper bound of $|\alpha_f| < 0.5$ must be imposed to avoid division by zero in Eq. 2.28. Imposing this single degree of freedom limits the highest order filter to a 10th order filter with a corresponding 11-point stencil. The coefficients for the various filters are shown in Table 2.5 . The order of accuracy of each filter is indicative of its level of low-wave number attenuation

Table 2.5: Coefficient for Interior Filter Formula ($|\alpha_f| < 0.5$)

Scheme	a_0	a_1	a_2	a_3	a_4	a_5	Stencil	$\mathcal{O}(h)$
F2	$\frac{1}{2}+\alpha_f$	$\frac{1}{2}+\alpha_f$	0	0	0	0	3	2
F4	$\frac{5}{8}+\frac{3\alpha_f}{4}$	$\frac{1}{2}+\alpha_f$	$\frac{-1}{8}+\frac{\alpha_f}{4}$	0	0	0	5	4
F6	$\frac{11}{16}+\frac{5\alpha_f}{8}$	$\frac{15}{32}+\frac{17\alpha_f}{16}$	$\frac{-3}{16}+\frac{3\alpha_f}{8}$	$\frac{1}{32}-\frac{\alpha_f}{16}$	0	0	7	6
F8	$\frac{93+70\alpha_f}{128}$	$\frac{7+18\alpha_f}{16}$	$\frac{-7+14\alpha_f}{32}$	$\frac{1}{16}-\frac{\alpha_f}{8}$	$\frac{-1}{128}+\frac{\alpha_f}{64}$	0	9	8
F10	$\frac{193+126\alpha_f}{256}$	$\frac{105+302\alpha_f}{256}$	$\frac{-15+30\alpha_f}{64}$	$\frac{45-90\alpha_f}{512}$	$\frac{-5+10\alpha_f}{256}$	$\frac{1-2\alpha_f}{512}$	11	10

with higher order filters containing less attenuation of the lower wave numbers. The spectral function for each order of accuracy is shown in Fig. 2.3 with a free parameter value of $\alpha_f = 0.35$. Deviation from unity indicates the level of damping the filter exerts on the flow solution for the respective wave number. Higher values of α_f also

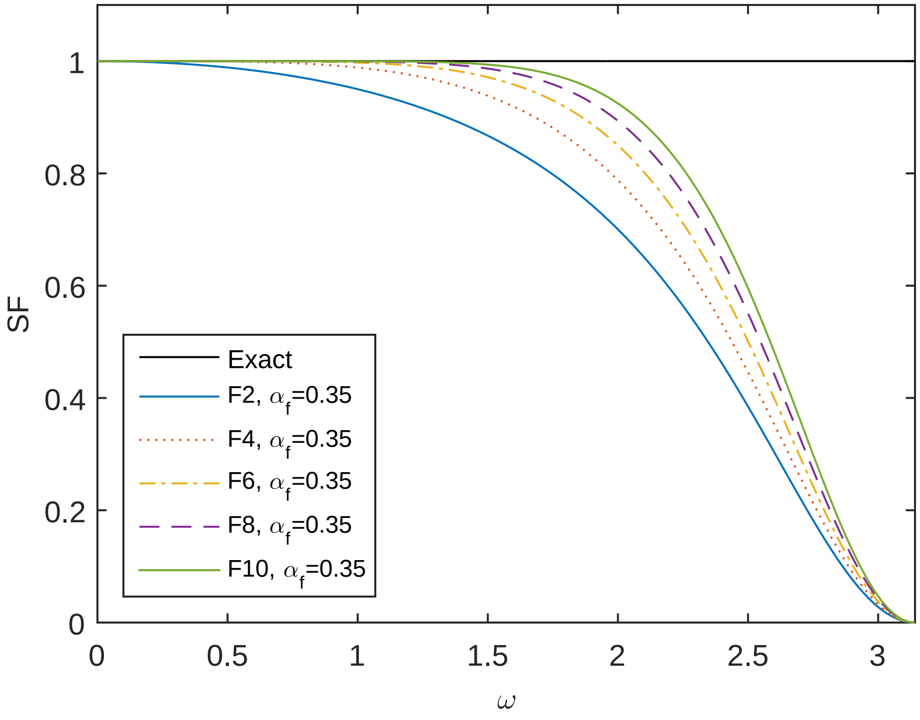

Figure 2.3: Filtering Effect with Order of Accuracy ($\alpha_f = 0.35$)

provide less damping limited by the upper bound mentioned previously. This trend can be seen for a 6th order filter in Fig. 2.4 .

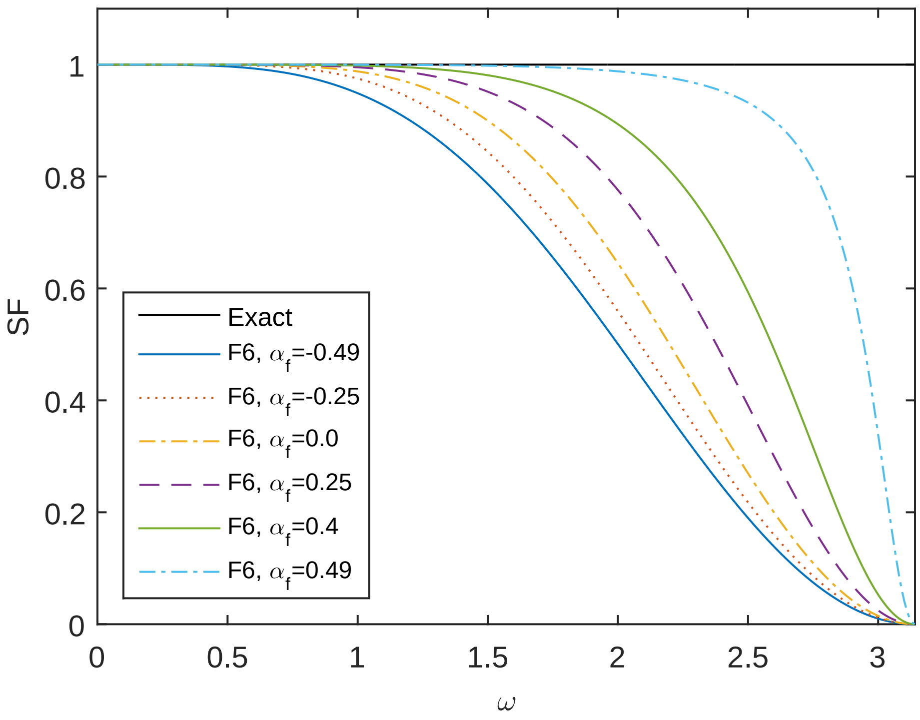

Figure 2.4: Filter effect of increasing α_f for a 6th order filter, F6

Combining the interior spatial discretization schemes with the spatial filter described herein gives the desired effect of resolving the lower wave numbers with no damping, while attenuating the higher unresolved wave numbers. Figure 2.5 illustrates this approach combining the 6th order interior spatial discretization scheme with a 10th order spatial filter ($\alpha_f = 0.35$).

2.4.3.2 Boundary Points

The interior spatial filtering scheme can use up to an 11-point stencil for the 10th order scheme. This requires special treatment at the boundaries of the solution domain where the stencil would extend beyond the boundaries. Points 1, ..., 5 and $N-4$, ..., N must change the stencil in order to avoid this problem. Points 1 and N are left out

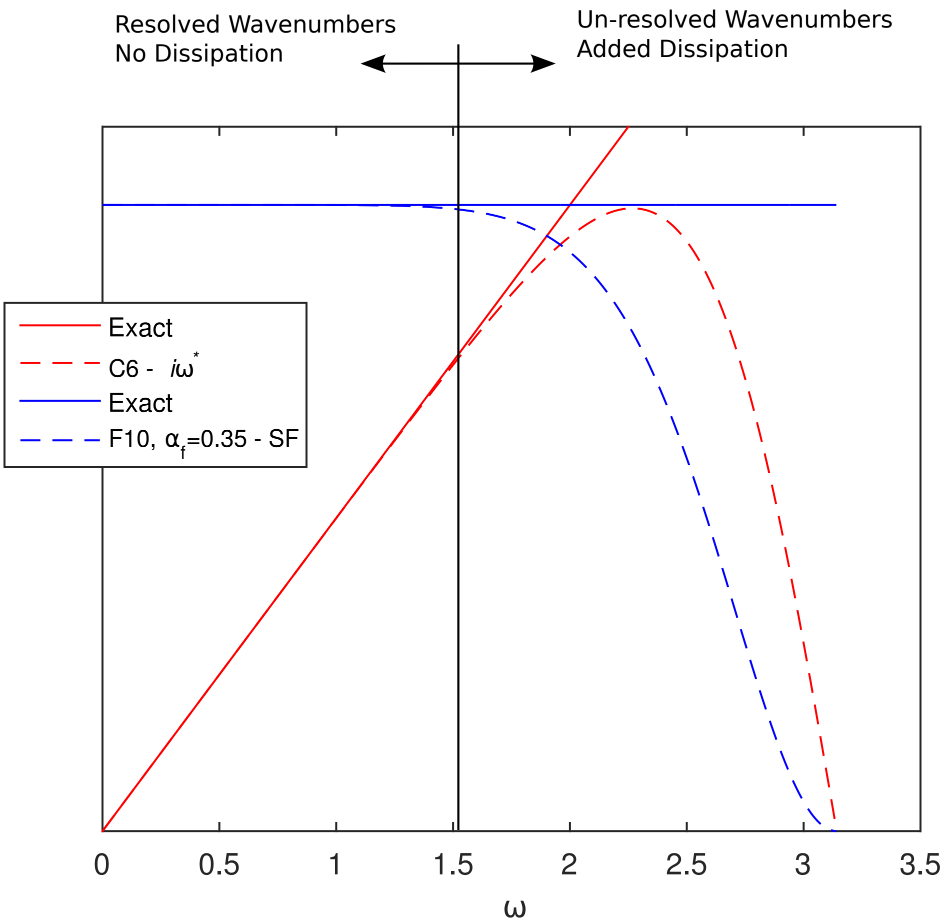

Figure 2.5: Combined 6th order compact difference scheme and 10th order spatial filter ($\alpha_f = 0.35$)

since there is no filtering at the boundaries due to the implementation of boundary conditions. There are two approaches to this problem that have been developed for FDL3DI.

The first approach involves using one-sided filter formulas while maintaining the tridiagonal structure of the interior, filter scheme. These formulas still require that $|\alpha_f| < 0.5$, but, in general, their spectral functions are complex. Thus, the one-sided filters can introduce artificial dispersion and for select wave numbers the real component is greater than unity indicating that certain wave numbers will be amplified. As α_f is increased, the amount of dispersion and degree of amplification, as opposed to attenuation, diminishes; therefore, a value of α_f as close as possible to 0.5 is suggested. Care must be taken to balance the larger values of α_f with the stability of the numerical scheme. The one-sided formulas and coefficients for these equations are given in Gaitonde and Visbal (1998).

The second approach maintains the centered scheme presented for the interior filtering, but reduces the order of the filter approaching the domain boundary. At the jth point from the boundary a filter with order $2j - 2$ would be used. It has been shown that as α_f approaches 0.5 a low-order filter scheme can have a similar dissipative effect to the higher-order filters in Visbal and Gaitonde (1998). This trend is shown in Fig. 2.6 and shows that the lowest order, F2, filter has very similar behavior to the highest order, F10, filter although the F2 filter begins dissipating the lower wave numbers more quickly than the F10 filter. This second approach will be used in this study to prevent potential amplification of wave numbers close to the boundaries.

2.4.4 Neumann Boundary Conditions

Dirichlet-type boundary conditions at the domain endpoints (point 1 and N) are straightforward to implement with the present compact difference schemes. Although,

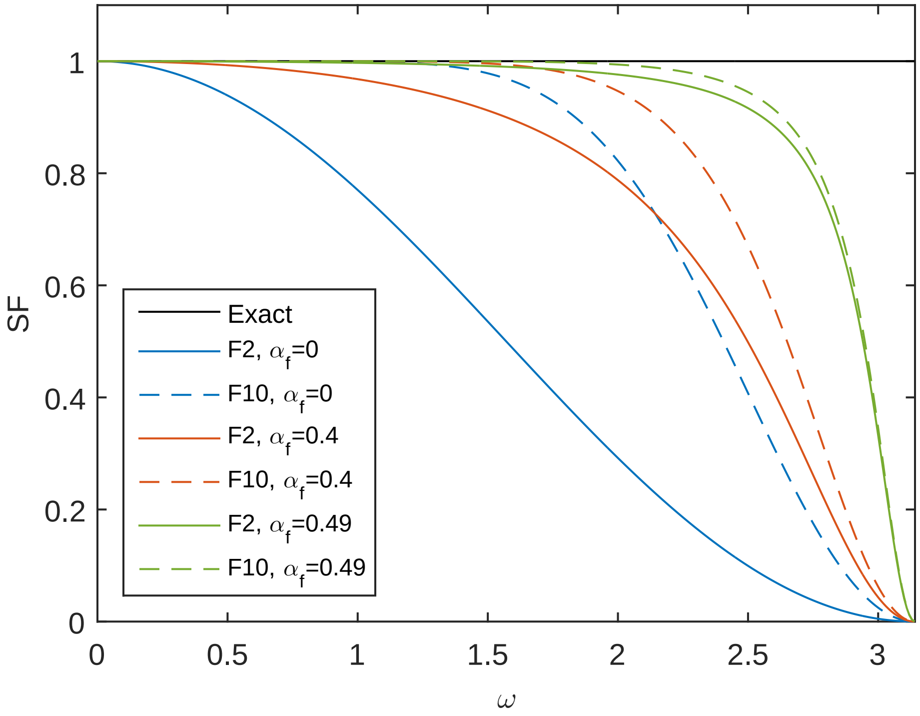

Figure 2.6: Comparison of low-order and high-order filter scheme with increasing α_f

Neumann conditions, such as the zero pressure gradient at a solid wall, require the use of higher order formulas. The following formulas can be used to set the value of a general scalar ϕ_1 and ϕ_N in terms of interior points to enforce the zero-gradient condition ($\partial\phi/\partial n = 0$). Selection of the coefficients can give up to 6th order accurate formulations.

For point 1 the formula is given as

$$\phi_1 = \frac{a\phi_2 + b\phi_3 + c\phi_4 + d\phi_5 + e\phi_6 + \phi_7}{A} \tag{2.29}$$

For point N the formula is given as

$$\phi_N = \frac{a\phi_{N-1} + b\phi_{N-2} + c\phi_{N-3} + d\phi_{N-4} + e\phi_{N-5} + f\phi_{N-6}}{A} \tag{2.30}$$

The value of the various coefficients and their corresponding order of accuracy are given in Table 2.6.

Table 2.6: Coefficients for the general formulation of $\partial\phi/\partial n$

$\mathcal{O}(h)$	a	b	c	d	e	f	A
6	360	-450	400	-225	72	-10	147
5	300	-300	200	-75	12	0	137
4	48	-36	16	-3	0	0	25
3	18	-9	2	0	0	0	11
2	4	-1	0	0	0	0	3
1	1	0	0	0	0	0	1

2.5 Grid Metric Calculations

Freestream preservation and metric cancellation are two important concepts that must be addressed for the high-order compact schemes used herein. These errors arise from the finite-difference formulations used for the governing equations in strong-conservation form, and they can cause large errors essentially destroying the accuracy of the higher-order compact schemes. Analytically the grid metrics are given as

$$\begin{aligned}
\frac{\xi_x}{J} &= y_\eta z_\zeta - y_\zeta z_\eta & \frac{\xi_y}{J} &= z_\eta x_\zeta - z_\zeta x_\eta & \frac{\xi_z}{J} &= x_\eta y_\zeta - x_\zeta y_\eta \\
\frac{\eta_x}{J} &= y_\zeta z_\xi - y_\xi z_\zeta & \frac{\eta_y}{J} &= z_\zeta x_\xi - z_\xi x_\zeta & \frac{\eta_z}{J} &= x_\zeta y_\xi - x_\xi y_\zeta \\
\frac{\zeta_x}{J} &= y_\xi z_\eta - y_\eta z_\xi & \frac{\zeta_y}{J} &= z_\xi x_\eta - z_\eta x_\xi & \frac{\zeta_z}{J} &= x_\xi y_\eta - x_\eta y_\xi
\end{aligned} \tag{2.31}$$

where J is the Jacobian of the coordinate transformation, which can be evaluated as

$$J = \left[x_\xi \left(y_\eta z_\zeta - z_\eta y_\zeta\right) - x_\eta \left(y_\xi z_\zeta - z_\xi y_\zeta\right) + x_\zeta \left(y_\xi z_\eta - z_\xi y_\eta\right)\right]^{-1} \tag{2.32}$$

In deriving the strong-conservation form of the governing equations, the following metric identities have been implicitly invoked

$$\begin{aligned}
\left(\frac{\xi_x}{J}\right)_\xi + \left(\frac{\eta_x}{J}\right)_\eta + \left(\frac{\zeta_x}{J}\right)_\zeta &= 0 \\
\left(\frac{\xi_y}{J}\right)_\xi + \left(\frac{\eta_y}{J}\right)_\eta + \left(\frac{\zeta_y}{J}\right)_\zeta &= 0 \\
\left(\frac{\xi_z}{J}\right)_\xi + \left(\frac{\eta_z}{J}\right)_\eta + \left(\frac{\zeta_z}{J}\right)_\zeta &= 0 \\
\left(\frac{1}{J}\right)_t + \left(\frac{\xi_t}{J}\right)_\xi + \left(\frac{\eta_t}{J}\right)_\eta + \left(\frac{\zeta_t}{J}\right)_\zeta &= 0
\end{aligned} \tag{2.33}$$

For a finite-difference formulation, all of these identities must be satisfied numerically in order to ensure freestream preservation. For a time-invariant coordinate transformation, only the first three identities apply since the last identity would automatically be fulfilled. Visbal and Gaitonde (1999) showed that a highly distorted curvilinear 2D mesh exhibited very small metric cancellation errors when the metrics were evaluated with the same compact difference schemes that were used for evaluating the spatial flux terms of the governing equations. The freestream preservation of the compact schemes was found to be very similar to that of a standard second-order central difference method (Steger, 1978). The curvilinear mesh was also generated analytically allowing for the analytical solution of the grid metrics. This resulted in significant errors and thus, should be avoided.

While the compact difference schemes can be accurately applied to solve for the metric values in Eq. 2.31 for the two-dimensional case, this cannot be extended to the three-dimensional case where special metric evaluation techniques are necessary (Pulliam and Steger 1980, Vinokur 1989, and Steger 1978). Application of either explicit or compact difference schemes to solve for Eq. 2.31 will not satisfy the identities in Eq. 2.33. For lower-order schemes this issue has been addressed by

Pulliam and Steger (1980) by introducing a simple averaging procedure while Vinokur (1989) suggested the use of finite-volume concepts. However, these techniques are not readily extensible to the higher-order compact difference schemes used in this study.

An alternative method for meeting the required identities was demonstrated by Thomas and Lombard (1978). In lieu of an averaging process or use of geometric concepts, the metric equations are reformed prior to discretization in an equivalent "conservative" form

$$\begin{aligned}
\frac{\xi_x}{J} &= (y_\eta z)_\zeta - (y_\zeta z)_\eta & \frac{\xi_y}{J} &= (z_\eta x)_\zeta - (z_\zeta x)_\eta & \frac{\xi_z}{J} &= (x_\eta y)_\zeta - (x_\zeta y)_\eta \\
\frac{\eta_x}{J} &= (y_\zeta z)_\xi - (y_\xi z)_\zeta & \frac{\eta_y}{J} &= (z_\zeta x)_\xi - (z_\xi x)_\zeta & \frac{\eta_z}{J} &= (x_\zeta y)_\xi - (x_\xi y)_\zeta \\
\frac{\zeta_x}{J} &= (y_\xi z)_\eta - (y_\eta z)_\xi & \frac{\zeta_y}{J} &= (z_\xi x)_\eta - (z_\eta x)_\xi & \frac{\zeta_z}{J} &= (x_\xi y)_\eta - (x_\eta y)_\xi
\end{aligned} \tag{2.34}$$

This method was used in the context of lower-order methods but did not receive wide use due to the simpler averaging process of Pulliam and Steger (1980). Although Eq. 2.34 was not originally intended for higher-order compact difference schemes, it was shown to satisfy freestream preservation and metric cancellation on a general three-dimensional curvilinear mesh by Visbal and Gaitonde (2002). This technique is used in the current study incorporating the same discretization as the spatial fluxes for solving the "conservative" grid metric equations.

2.6 Chimera Overset Mesh and Hole Cutting

Structured mesh approaches, in general, are more efficient and accurate than their unstructured counterparts. The "structure" of the structured mesh makes it easier to identify neighboring points and allows creating a mesh that is aligned with the flow and normal to features such as a wall. For the current schemes used in FDL3DI, a structured mesh approach is also ideal. The disadvantages of structured meshes become apparent when attempting to create a computational domain for a complex geometry. This is often impossible with a single structured mesh, or if possible, can result in grid points clustered in regions of small gradients and thus wasted computational resources. To address some of the limitations of a structured mesh, Steger et al. (1983) introduced the idea of a "Chimera" overset mesh. This technique involves the overlap of multiple structured meshes. A complex geometry can be broken down into small, simple geometries in which an ideally structured mesh can be created. These simple structured meshes are then overlapped with one another and usually connected with a large background mesh. In the overlapped regions, information is transferred from one mesh to another, usually through an interpolation process. This allows for continuity of the flow solution across the various overlapped meshes. This approach was originally developed to address complex geometries (Murman et al. 2000, Gomez et al. 2004), but can also be useful in simulating bodies in relative motion (Prewitt et al. 2000), providing grid adaptation abilities, or used in the construction of a massively parallel computing paradigm. The application to parallel computing is discussed in Section 2.7. An example of a Chimera mesh for the current LPT application is presented in Fig. 2.7 . This figure shows a body-fitted O-grid that encompasses the turbine blade which allows for easy grid refinement at the turbine wall and a background H-grid that connects the O-grid to flow through the entire channel.

Two issues are evident in the Chimera mesh approach:

1. The "background" H-grid will solve for a flow solution inside the turbine blade solid walls where there is no flow.
2. The two solutions will exist where the O-grid and H-grid overlap each other.

To address both of these issues, Benek et al. (1983) presented a hole-cutting technique which expands the flexibility and usefulness of the Chimera mesh approach. This

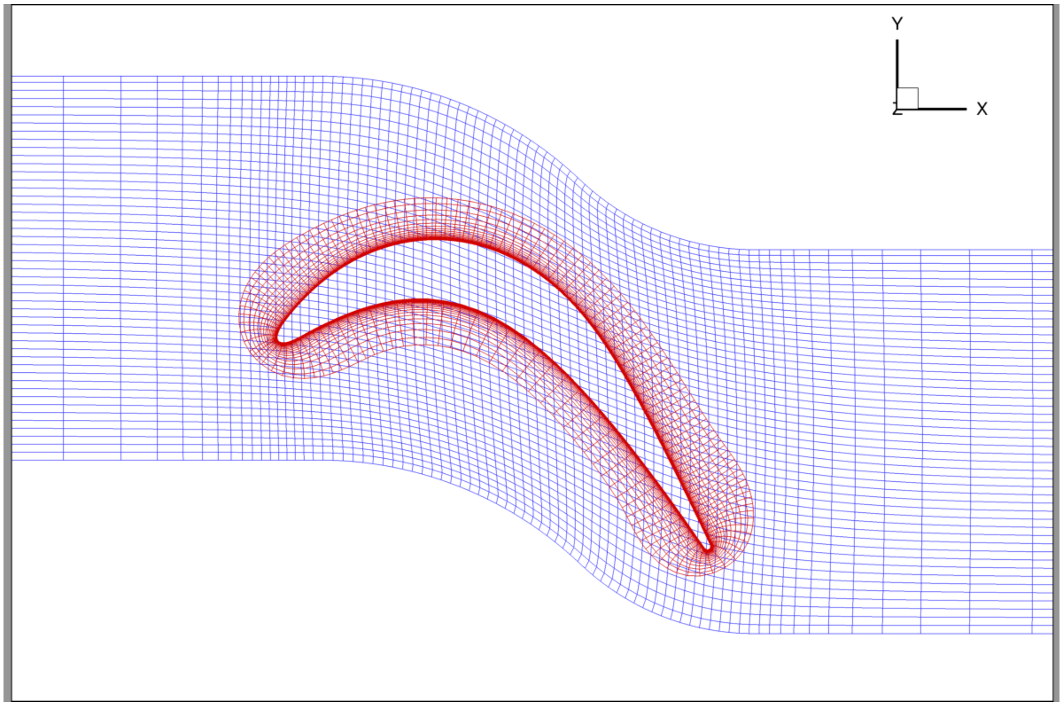

Figure 2.7: Example Chimera Mesh for LPT (representative Pack-B blade)

approach is used to remove computational nodes from background meshes inside of solid objects (such as the turbine blade for the current problem), and to remove nodes from coarser meshes that overlap with a more refined mesh. This addresses both of the concerns mentioned previously. It is important to note that “removing” points does not completely eliminate them in the solver algorithms. These points will still exist, but are de-coupled from the other nodes so that they do not influence the flow solution. This means that the hole will incur a computational overhead where redundant calculations are being made; therefore, a user should wisely incorporate the use of hole-cutting to prevent large overhead.

During the differencing or filtering sweeps of the FDL3DI solver, holes create new “hole boundaries” that were not present in the original mesh and must be handled appropriately. Assuming a five-point stencil for the spatial discretization points located within two points of the hole boundary must have their differencing scheme modified to the selected boundary point formulation that was set for the computational coordinate. Figure 2.8 shows a 1-D diagram of how this change influences the points next to the hole boundary. A similar approach must be incorporated into the filtering scheme depending on the stencil size. For an 11-point stencil, a node 5 points within the hole boundary must have its corresponding formulation modified . Points inside the hole boundary are de-coupled from the surrounding flow solution through modification of the coefficient given in the general form of the spatial discretization or filter formulations given in Equs. 2.15 and 2.27. In order to decouple these points, the implicit, left-hand side of both derivative and filter formulations are modified, setting α and α_f to 0, respectively. The coefficients of the right-hand side are also set to 0 to remove its contribution to the solution. Equs. 2.35 and 2.36 demonstrate the coefficient matrix of a general compact difference scheme before and after the creation of the hole. Notice the insertion of the coefficients for the boundary point spatial discretization schemes from Equs. 2.23, 2.24, 2.25, and 2.26. This is a result of the computational boundary created by the hole boundary. The hole breaks what was a continuous implicit domain into three de-coupled regions with a hole region between two implicit domains. This modification maintains the tridiagonal nature of the equations so that it may be efficiently solved.

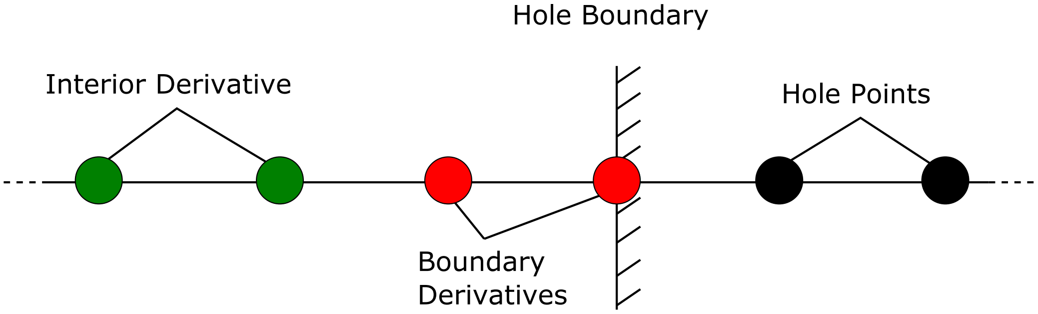

Figure 2.8: Hole Boundary modification

$$\left[\begin{array}{ccccccccccccc}
\ddots & \ddots & \ddots & & & & & & & & & & \\
 & \alpha & 1 & \alpha & & & & & & & & & \\
 & & \alpha & 1 & \alpha & & & & & & & & \\
 & & & \alpha & 1 & \alpha & & & & & & & \\
\hline
 & & & & \alpha & 1 & \alpha & & & & & & \\
 & & & & & \ddots & \ddots & \ddots & & & & & \\
 & & & & & & \alpha & 1 & \alpha & & & & \\
\hline
 & & & & & & & \alpha & 1 & \alpha & & & \\
 & & & & & & & & \alpha & 1 & \alpha & & \\
 & & & & & & & & & \alpha & 1 & \alpha & \\
 & & & & & & & & & & \ddots & \ddots & \ddots
\end{array}\right] \quad \text{Before Hole Cutting} \tag{2.35}$$

$$\left[\begin{array}{ccccccccccccc}
\ddots & \ddots & \ddots & & & & & & & & & & \\
 & \alpha & 1 & \alpha & & & & & & & & & \\
 & & \alpha_{M1} & 1 & \alpha_{M2} & & & & & & & & \\
 & & & \alpha_N & 1 & 0 & & & & & & & \\
\hline
 & & & & 0 & 1 & 0 & & & & & & \\
 & & & & & \ddots & \ddots & \ddots & & & & & \\
 & & & & & & 0 & 1 & 0 & & & & \\
\hline
 & & & & & & & 0 & 1 & \alpha_1 & & & \\
 & & & & & & & & \alpha_{21} & 1 & \alpha_{22} & & \\
 & & & & & & & & & \alpha & 1 & \alpha & \\
 & & & & & & & & & & \ddots & \ddots & \ddots
\end{array}\right] \quad \text{After Hole Cutting} \tag{2.36}$$

An area of concern when combining hole cutting and the high-order spatial algorithms used in FDL3DI is maintaining the minimum-stencil size for the differencing and filtering operations. A 10th-order filter is the most restricting with an 11-point stencil. For the current problem, difficulties can be encountered on the pressure side of the blade where the blade curvature can produce a hole where the ξ-computational direction will not have enough points. Likewise, problems can occur near the trailing edge and at the peak of the suction surface where the O-grid of the blade can extend close to the walls of the H-grid channel. This could result in a hole which creates stencil problems in the η-computational coordinate. Figure 2.9 shows an H-grid which has been hole-cut to remove grid points where the turbine blade occupies the passage. Shown in this diagram are the three locations where minimum stencil requirements must be considered during the hole-cutting process. For the current study a 10th order filter was incorporated, thus requiring a minimum 11-point stencil. Care was taken in the hole cutting process to ensure the minimum stencil was satisfied.

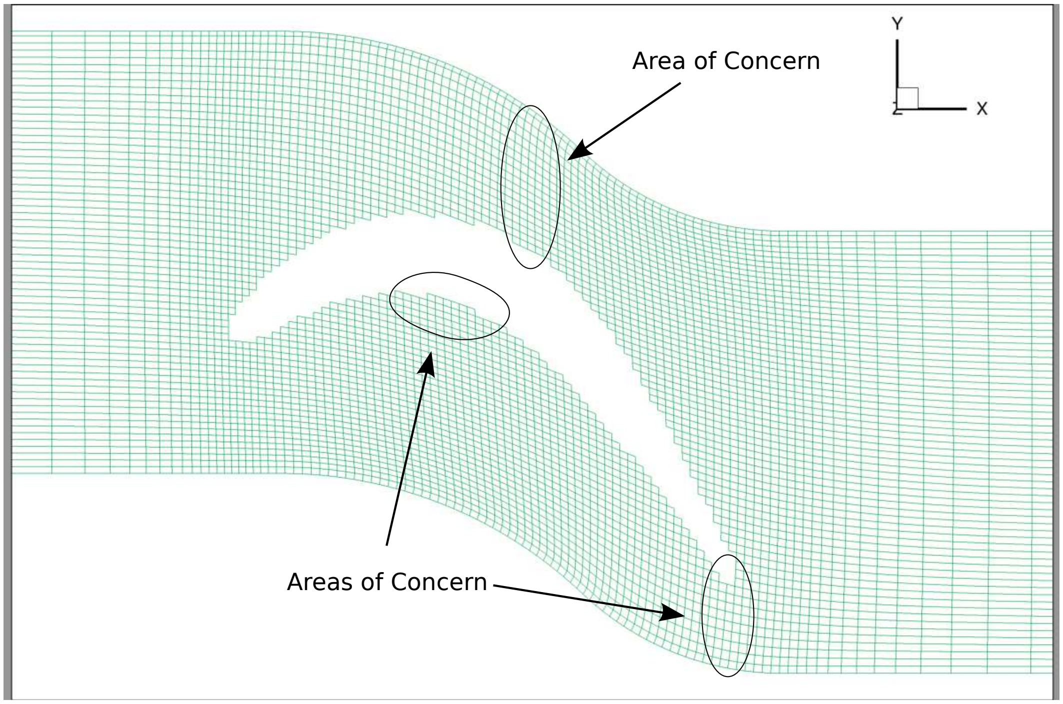

Figure 2.9: Areas of potential minimum stencil violation for hole cutting

As mentioned before, the overlapping meshes that are created as a result of the Chimera technique require appropriate boundary conditions, including hole type boundaries. Rarely will these overlapping meshes have points that coincide with each other, thus an interpolation of the solution from one mesh to the other must be made. The process of hole-cutting and interpolation are implemented in the current study with the pre-processing software PEGASUS 1.5k (Rogers et al., 2003) a NASA Ames software package, and BELLERO (Sherer et al., 2006) an AFRL code. PEGASUS handles the hole-cutting and sets up donor and receiver grid point stencils for mesh interpolation. The interpolation setup by PEGASUS is spatially second-order accurate (Benek et al., 1986). BELLERO is then used for two purposes. First, it decomposes the computational domain into blocks for parallel computation (discussed in the next Section 2.7), and secondly, starts with the interpolation stencils setup with PEGASUS and calculates higher-order interpolation coefficients for use in FDL3DI. This higher-order interpolation is a 6th order accurate scheme used to mitigate the degradation of the spatial accuracy of the compact difference schemes. This interpolation requires that each receiving mesh overlap has, at least, two points in the interior of the donor mesh (fringe points or points which must be interpolated). BELLERO will automatically check that the minimum stencil size is met and will provide feedback if it is unable to produce the high-order stencil due to the configuration of overlapping meshes and any hole-cutting.

2.7 Parallel Computation

The previous section mainly discussed the use of the Chimera overset grid method to accommodate the meshing of complex geometries. Another potential use of the Chimera technique is subdividing the mesh into smaller “blocks” which can be assigned to separate computer processors in order to create a parallel processing system.

Each processor can solve the governing equations simultaneously and has the potential to greatly reduce computer processing time. The Chimera technique allows the computational domain to be decomposed into blocks which overlap each other in order to transfer information between blocks. Figure 2.10 shows a diagram of this decomposition process for a 1D mesh (the 1D case can easily be extended to higher dimensions). The original mesh is divided at point j into two separate blocks. Gaitonde and Visbal (2000) showed that a five-point overlap is sufficient for maintaining the interior higher-order differencing and filtering of the original non-decomposed mesh. This requires that all overlaps have two fringe points (points where interpolation from another grid occurs). This overlap creates additional grid points and increases computational overhead. The decomposition process necessitates the balancing of the number of processors, memory available for each processor, and load balancing between processors.

The decomposed grid, requires an extra step in the solver algorithm where the flow solution can be transferred from the donor mesh to the receiving mesh. The transfer of information is shown in Fig. 2.10 with arrows indicating the flow of information. Information transferred from block 1 to block 2 acts as boundary conditions on block 2 and vice versa. This allows for a seamless transition between overlapping blocks and maintains the formal order of accuracy of the interior schemes. The transfer of information at boundaries is implemented with a message passing interface (MPI) library (Message Passing Interface Forum (1994)). MPI updates occur twice during each sub-iteration for the time integration and then again after application of the filtering scheme.

The decomposition process differs slightly from the general Chimera method described in the previous section. In general, when overlapping different meshes, grid points will not coincide, which requires interpolation for transferring data from one grid to another. In the decomposition process of a grid, the five overlapping points

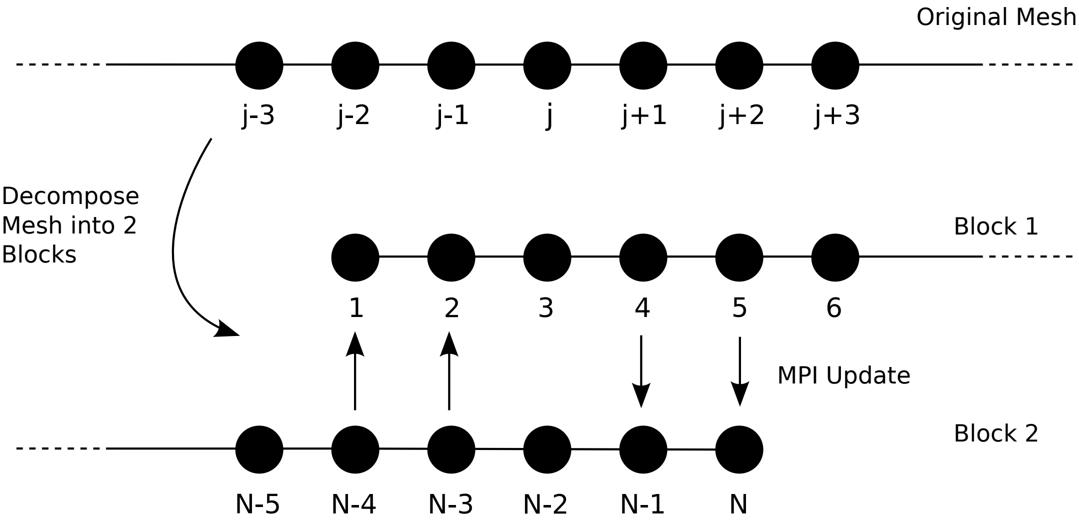

Figure 2.10: MPI update at grid overlap region

are coincident so no interpolation is necessary and values can be “directly injected” into the receiving mesh. Both methods require an extra step in the flow solution algorithm for the MPI update to occur and “sync” the meshes. The AFRL code BELLERO was used for automatic decomposition of meshes. BELLERO will try to maximize the load balance between different blocks limited by the configuration of overlapping meshes, hole-cutting, and minimum stencil requirements.

2.8 Present Numerical Scheme

Much of the selection of schemes here was based on the stability of the solver and past user experience. Selections were made in a way to avoid amplification of wave numbers and provide dissipation at appropriate levels depending on how resolved the higher wave numbers were for a given differencing scheme. Past user experiences with FDL3DI (Poondru, 2007, Galbraith, 2009, and VonHagen, 2011) were all considered in deciding which schemes to use.

The solver has the capability to use different differencing schemes in each computational direction (ξ, η, ζ) and for the grid metrics. For the current study, the same schemes will be used for all computational directions and the grid metrics. The current study will incorporate the 6th-order compact differencing schemes for interior points. Approaching the domain boundaries, a one-sided 5th-order scheme is used at the second boundary point and a one-sided 4th order scheme at the first boundary point. The current differencing scheme selection is shown in Table 2.7 using the acronyms for the various schemes corresponding to Tables 2.1, 2.4, and 2.2.

Table 2.7: Compact difference schemes of current study

	Domain Location				
Coordinate	1	2	Interior	$N-1$	N
ξ	C4	AC5	C6	AC5	C4
η	C4	AC5	C6	AC5	C4
ζ	C4	AC5	C6	AC5	C4
Metrics	C4	AC5	C6	AC5	C4

The filtering schemes also have the capability of being selected individually for each computational direction. For this study, all computational directions incorporated the same filtering scheme. A 10th-order filter was used for all interior points with $\alpha_f = 0.35$. This selection provides a good balance between the resolution of lower wave numbers and dissipation of the higher, unresolved wave numbers. The second method described in Section 2.4.3.2 was used for filters closer to the boundaries in order to prevent amplification of wave numbers near boundaries. Therefore, the filter order was decreased to keep a central filtering scheme for each boundary point. The free parameter, α_f, was kept constant except at boundary point 2 ($N-1$), where a higher value ($\alpha_f = 0.49$) was used to maintain accuracy as shown by Visbal and Gaitonde (1998). The current filtering selection is shown in Table 2.8 using acronyms corresponding to those in Table 2.5.

Table 2.8: Filtering schemes of current study

		Domain Location					
Coordinate		1, N	2, $N-1$	3, $N-2$	4, $N-3$	5, $N-4$	Interior
ξ	Filter	0	F2	F4	F6	F8	F10
	α_f	0.0	0.49	0.35	0.35	0.35	0.35
η	Filter	0	F2	F4	F6	F8	F10
	α_f	0.0	0.49	0.35	0.35	0.35	0.35
ζ	Filter	0	F2	F4	F6	F8	F10
	α_f	0.0	0.49	0.35	0.35	0.35	0.35

Chapter 3

Numerical Setup

This chapter presents a discussion of the overall numerical setup for the current LPT flow simulation. In later chapters, any information specific to the simulations discussed will be included. The discussion here serves as a general overview of the numerical approach.

3.1 Time Averaging

For all simulations, the initial conditions were set up by interpolation from a baseline mesh solution which was used in the Reynolds number iterations (described in Section 3.5) to improve the initial solution estimate. From these initial conditions, the solution was allowed to develop for a given number of non-dimensional time units, referred to as the “transient” run. After allowing the solution to develop it was averaged over each simulation iteration in order to calculate the time-averaged flow solution. This second run is referred to as the “data” run.

3.2 Turbulence Frequency Spectra

The calculation of turbulence frequency spectra requires the time history of fluctuating velocity components. For these calculations, the solution was allowed to develop a time-averaged solution before starting the collection of time histories of fluctuating velocities. Fluctuating velocities were calculated as follows

$$u_i^{'} = u_i - \overline{u_i} \tag{3.1}$$

where $\overline{u_i}$ represents the time-average of the various Cartesian velocity components. Given the time histories of the fluctuating component of the velocity, the Fourier modes of each velocity component could be calculated as

$$\hat{u}_i^{'}\left(x_i, \omega\right) = \mathcal{F}\left\{u_i^{'}\left(x_i, t\right)\right\} \tag{3.2}$$

where $\mathcal{F}\left\{\right\}$ is the Fourier transform and x_i is the Cartesian spatial coordinates. Subsequently, the turbulent frequency spectra can be calculated as follows

$$E_\omega\left(x_i, \omega\right) = \frac{1}{2}\left(\hat{u}_i^{'} \cdot \hat{u}_i^{'*}\right) \tag{3.3}$$

where $\hat{u}_i^{'*}$ is the complex conjugate of $\hat{u}_i^{'}$.

For the current LPT simulations, there were two general types of simulations. The first case was without any form of flow control referred to as a “baseline” flow case, and the second being the “flow control” case which incorporated the use of VGJs in order to mitigate separation. For baseline cases, the turbulent frequency spectra was calculated along a line in the spanwise direction of the blade. The frequency spectra were then spanwise-averaged due to the homogeneous nature of the baseline case. In the flow control cases, the frequency spectra were only calculated at a single point on the end of the domain (between jets when considering periodic boundaries). A detailed treatment of the derivations for turbulence frequency spectra can be found in the work of Pope (2000).

3.3 H-O Meshing Technique

All computational meshes were generated with the commercial software Pointwise®. In order to conserve computational resources, only a single turbine blade was considered for all simulations in the current study. This necessitates periodic boundary conditions in the cross-flow direction to simulate an entire turbine cascade. Ideally, a structured mesh should be aligned with the flow direction, and for the current problem would require a grid that is aligned with the inflow and outflow angles of the flow as shown in Fig. 3.1. The issue with such a mesh is that the highly curved blade, along with the need for periodic cross-flow boundaries will produce a highly skewed mesh through the flow channel. Thompson et al. (1985) discussed that a non-dissipative scheme coupled with grid skewness, streamwise grid stretching, and large cross-flow velocity can lead to large dispersive errors and instability.

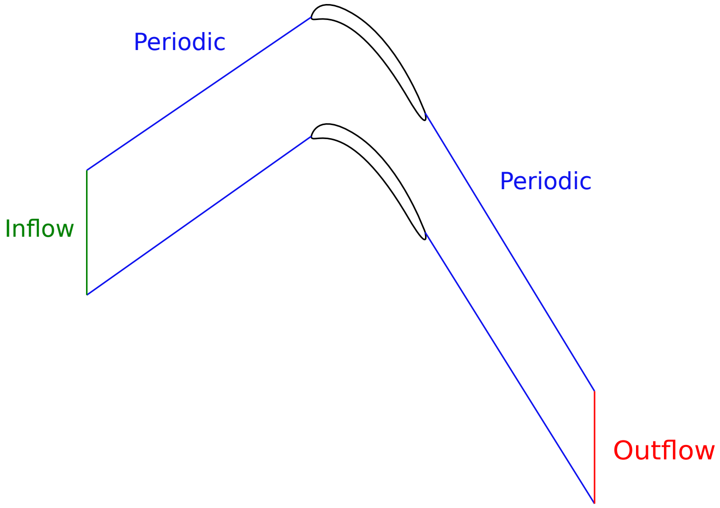

Figure 3.1: Outline of flow aligned turbine cascade mesh

To alleviate these issues with the flow-aligned mesh, the current study uses an approach, similar to that of Rizzetta and Visbal (2003*b*). In this approach, the inflow and outflow are captured with a background H-grid, while detailed flow features around the blade are captured with a body-fitted O-grid. A representative example is shown in Fig. 3.2. This approach will incorporate the Chimera and hole-cutting techniques discussed in Section 2.6.

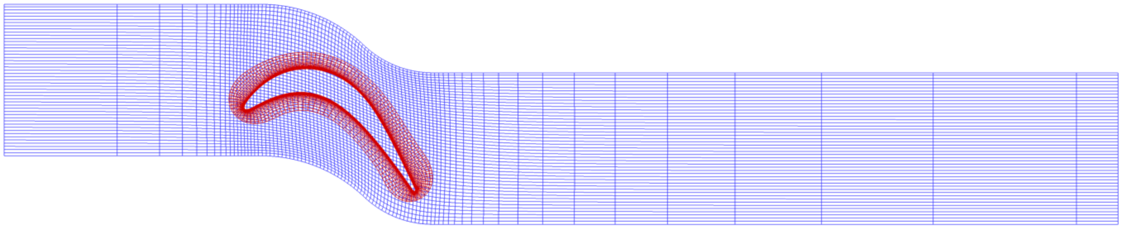

Figure 3.2: H-O grid topology meshing technique (representative Pack-B)

To further save on computational resources, the upstream inflow and downstream outflow boundaries were positioned close to the blade. The inflow was located $1.5C_x$ in front of the blade leading edge while the outflow was $5.0C_x$ downstream of the trailing edge.

Shown in Fig. 3.2, the mesh is stretched near the outflow boundary. This stretching prevents the reflection of pressure waves back into the computational flow domain. This technique takes advantage of the characteristics of the low-pass spatial filter to help prevent this reflection. The rapid mesh stretching promotes the reflection of energy at the interface between mesh cells that are very different in size. This reflected energy is then transferred into high-frequencies which are then filtered from the solution, using the low-pass, high-order filtering, without affecting the true flow solution. This technique was utilized for various aeroacoustic problems by Visbal and Gaitonde (2001).

3.4 Mesh Spanwise Extent

To additionally save on computational resources, the spanwise extent of the mesh was reduced and periodic boundary conditions invoked in the spanwise direction. This effectively created an infinite span blade for the simulation. If the span is too small the solution will be artificially constrained and effectively become two-dimensional. Rizzetta and Visbal (2003*b*) and Galbraith (2009) both found that a spanwise extent of $0.2C_x$ was sufficient to allow the development of large-scale flow structures. Therefore, the $0.2C_x$ spanwise extent was used for all baseline simulations, i.e. computations without flow control measures. For the cases where VGJs were incorporated for flow control, the spanwise extent of the mesh was fixed to the spacing in-between jets. This effectively creates an infinite span blade with jet holes along the entire span of the blade.

3.5 Reynolds Number Iteration

In trying to match other numerical simulations and experiments for LPT cascades the Reynolds Number is often specified at the inlet or outlet of the flow domain or wind tunnel. This presents an issue with the current setup because the inflow and outflow boundaries are close enough to the turbine blade that the velocities at these boundaries evolve as part of the solution. Thus, an iterative approach is used to get the appropriate inflow Reynolds number.

In the FDL3DI solver, the user will set the reference Reynolds number as part of the input. Then a simulation must be allowed to evolve and time-averaged values must be calculated. From these time-averaged values the average Reynolds number at the inlet can be matched with the desired value. Therefore, this approach requires iterating on the value of the reference Reynolds number to get the appropriate inflow conditions. This approach has been successfully used by Rizzetta and Visbal (2003*b*), Rizzetta and Visbal (2005), and Poondru (2007). The inlet Reynolds number (Re_{in}) can be calculated from Re_∞ using the following formula

$$Re_{in} = \frac{\rho_{in} U_{in}}{\mu_{in}} Re_\infty \tag{3.4}$$

3.6 Mach Number

Most experimental investigations of LPT cascade flow are conducted with low-speed wind tunnels. Thus, the experiments are conducted under incompressible flow conditions. As presented in Chapter 2, FDL3DI solves the compressible Navier-Stokes equations and must have a reference Mach number specified. However, with compressible flow solvers, a Mach number near zero can cause numerical instability. There are methods to address this issue but none has been incorporated into FDL3DI. Other studies involving LPT flow and FDL3DI have all used $M_\infty = 0.1$ to approximate incompressible flow. This same value is used for all the simulations of the current study.

3.7 Boundary Conditions

The boundary conditions discussed here were used for all simulations. Baseline flow cases did not incorporate the use of the VGJ boundary condition and maintained the wall boundary condition over the entire turbine blade.

3.7.1 Wall Boundary Conditions

The turbine blade surface was implemented with a no-slip, adiabatic wall, and a zero normal pressure gradient. The no-slip condition is specified by setting all velocity components to zero. Density is calculated assuming that its normal gradient is zero.

This is a result of the zero normal pressure gradient and the adiabatic wall (zero normal temperature gradient) which results in the zero normal gradient of density through the ideal gas law. All normal gradients are calculated with the 4th order explicit differencing formula given in Section 2.4.4; accordingly, the η computational coordinate is assumed to be aligned with the wall normal to facilitate this calculation.

3.7.2 Periodic Boundary Conditions

Periodic boundary conditions were used in the current problem to help minimize the use of computational resources. The turbine blade was assumed to have an infinite span which was implemented with spanwise periodic boundary conditions. This boundary required a five-point overlap as discussed in Sections 2.6 and 2.7.

Also, to implement periodicity between turbine blades of a true linear cascade, periodic conditions were used in the cross-flow direction. Again, this required the use of a five-point overlap at the mesh boundary for proper implementation.

Periodic conditions and the required extension of the meshes to create the necessary overlap was automatically executed by BELLERO during the grid decomposition process.

3.7.3 Inflow/Outflow Boundary Conditions

Inflow and outflow boundaries are specified following a characteristics analysis. For a three-dimensional, subsonic flow, the inlet will have four characteristics entering the computational domain while one is leaving. Conversely, the outlet will have one characteristic entering with four leaving (Poinsot and Lele, 1992). Kreiss (1970) suggested that the number of “physical” boundary conditions should be equal to the number of incoming characteristics; therefore, four physical values will be specified at the inlet and one at the outlet. Total pressure (p_t), total temperature (T_t), and two flow angles (α, β) will be specified at the inlet. Static pressure will be specified at the exit. All other values will be specified through numerical boundary conditions that extrapolate information from the interior flow domain. This same method of boundary conditions has been implemented by Rizzetta and Visbal (2003*b*). Specifics of the numerical boundary condition implementation follows the method used by Poondru (2007).

At the inlet it is important to maintain the flow angle to allow for the correct formation of the leading-edge stagnation point. The following procedure is used to specify u, v, w, p, and ρ at the inlet. First, consider the isentropic relation for total temperature

$$T_t = T\left(1 + \left(\frac{\gamma - 1}{2}\right) M^2\right) \tag{3.5}$$

in which M is the local Mach Number. Substituting the local Mach Number in terms of dimensional quantities, the following is obtained

$$T_t = T\left(1 + \left(\frac{\gamma - 1}{2}\right) \frac{U^{*2}}{\gamma R T^*}\right) \tag{3.6}$$

where U^* is the local dimensional velocity magnitude. Furthermore, this equation can be defined in terms of reference Mach Number by incorporating the definitions of the non-dimensional velocity and temperature, inserting the reference Mach number and canceling terms

$$\begin{aligned} T_t &= T\left(1 + \left(\frac{\gamma - 1}{2}\right) \frac{U^2 U_\infty^2}{\gamma R T T_\infty}\right) \\ &= T\left(1 + \left(\frac{\gamma - 1}{2}\right) \frac{U^2}{\gamma R T} \frac{\gamma R T_\infty M_\infty^2}{T_\infty}\right) \\ &= T\left(1 + \left(\frac{\gamma - 1}{2}\right) \frac{U^2 M_\infty^2}{T}\right) \end{aligned} \tag{3.7}$$

Now rearrange terms to get the static temperature in terms of the total temperature

$$T = T_t - \left(\frac{\gamma-1}{2}\right) U^2 M_\infty^2 \tag{3.8}$$

The velocity magnitude is evaluated assuming the first-order derivative of the velocity is zero at the inflow boundary. Now the static temperature can be calculated at the inflow boundary; subsequently, the square of the local Mach Number can be calculated by rearranging Eq. 3.5

$$M^2 = \frac{2}{\gamma-1}\left(\frac{T_t}{T} - 1\right) \tag{3.9}$$

The isentropic relation for pressure can now be used to calculate the inflow static pressure

$$p = p_t\left(1 + \frac{\gamma-1}{2} M^2\right)^{\frac{-\gamma}{\gamma-1}} \tag{3.10}$$

Density can now be calculated using the ideal gas law

$$\rho = \frac{\gamma M_\infty^2 p}{T} \tag{3.11}$$

Cartesian velocities can also be calculated from their respective direction cosines as

$$u = Ua_1, \quad v = Ua_2, \quad w = Ua_3 \tag{3.12}$$

where the direction cosines are given by

$$\begin{aligned} a_1 &= \frac{1}{\sqrt{1 + \tan^2\alpha_1 + \tan^2\beta_1}} \\ a_2 &= \frac{\tan\alpha_1}{\sqrt{1 + \tan^2\alpha_1 + \tan^2\beta_1}} \\ a_3 &= \frac{\tan\beta_1}{\sqrt{1 + \tan^2\alpha_1 + \tan^2\beta_1}} \end{aligned} \tag{3.13}$$

and α_1 is the incoming flow pitch angle or angle of attack, with respect to the turbine axial chord. Also, β_1 is the side-slip angle of the incoming flow with respect to the turbine axial chord.

At the outflow boundary, the static pressure is specified. All other variables (u, v, w, ρ) are extrapolated from the interior domain assuming a zero first-order derivative at the exit.

3.7.4 VGJ Boundary Conditions

The current study seeks to implement flow control through the use of VGJs. VGJs can be defined, in part, by the angles of the jet. When considering the main flow direction, streamwise in the current problem, the "skew" angle (ϕ) of the jet is the angle measured from the main flow direction. Thus, a 90° skew would result in a jet that is perpendicular to the main flow. The "pitch" angle (θ) of the jet is defined with respect to the local turbine blade surface; for example, a 90° pitch would result in a "normal" jet that is perpendicular to the blade surface. In experimental testing, a VGJ is often implemented by drilling a hole into the blade surface that connects to a large plenum cavity where pressure can be controlled to influence the jet speed at the blade surface. In a numerical simulation, one would ideally simulate the entire cavity, allowing the velocity profile of the VGJ to develop realistically through the entire VGJ hole. In this study, to save on computational resources, VGJs will be simulated by defining a velocity profile on the turbine blade surface consistent with that of a fully developed VGJ velocity profile. This approach has been successfully applied in multiple studies (Kral et al. 1997, Poondru 2007, Memory et al. 2010). This approach also carries the benefit of easily changing the skew and pitch angles for potential parametric studies without having to recreate the computational mesh for each simulation.

The jet velocity is first defined through the Blowing Ratio (BR):

$$BR = \frac{U_{jet}}{U_{local}} \tag{3.14}$$

where U_{jet} is the maximum jet velocity of the VGJ and U_{local} is the local freestream velocity at the VGJ location. To approximate a fully developed VGJ velocity profile a paraboloid velocity distribution is used at the turbine blade surface, and U_{jet} is defined at the center of the jet hole as the maximum velocity. To calculate the local freestream velocity, a fully-attached flow, surface pressure distribution is used to calculate the velocity at the location of the VGJ (Sondergaard, 2012). Now, appropriate values of the jet velocity can be set to obtain the desired blowing ratio. For a given pitch and skew angle the jet velocities are defined as

$$\begin{aligned}
\widehat{U} &= U_{jet}\cos\theta\cos\phi \\
\widehat{V} &= U_{jet}\sin\theta \\
\widehat{W} &= U_{jet}\cos\theta\sin\phi
\end{aligned} \tag{3.15}$$

where $\widehat{U},\ \widehat{V},\ \widehat{W}$ are the "physical" contravariant velocity components (Hung, 2002) in the direction of the computational coordinates: $\xi,\ \eta,\ \zeta$. The Cartesian velocity components can be obtained as

$$\begin{aligned}
u &= \frac{x_\xi}{h_1}\widehat{U} + \frac{x_\eta}{h_2}\widehat{V} + \frac{x_\zeta}{h_3}\widehat{W} \\
v &= \frac{y_\xi}{h_1}\widehat{U} + \frac{y_\eta}{h_2}\widehat{V} + \frac{y_\zeta}{h_3}\widehat{W} \\
w &= \frac{z_\xi}{h_1}\widehat{U} + \frac{z_\eta}{h_2}\widehat{V} + \frac{z_\zeta}{h_3}\widehat{W}
\end{aligned} \tag{3.16}$$

where $h_1,\ h_2,\ h_3$ are scaling factors for the transformation to curvilinear coordinates and are defined below. The jet inflow was assumed to be isothermal and the pressure was obtained from the inviscid normal momentum equation, in an approach similar to that of Rizzetta and Visbal (2005) and Poondru (2007). The inviscid normal momentum equation cast in the η-computational direction is given as

$$\begin{aligned}\frac{\partial \widehat{V}}{\partial t} + \frac{\widehat{U}}{h_1}\frac{\partial \widehat{V}}{\partial \xi} + \frac{\widehat{V}}{h_2}\frac{\partial \widehat{V}}{\partial \eta} + \frac{\widehat{W}}{h_3}\frac{\partial \widehat{V}}{\partial \zeta} & \\ - \frac{\widehat{U}^2}{h_1 h_2}\frac{\partial h_1}{\partial \eta} + \frac{\widehat{U}\widehat{V}}{h_1 h_2}\frac{\partial h_2}{\partial \xi} + \frac{\widehat{V}\widehat{W}}{h_2 h_3}\frac{\partial h_2}{\partial \zeta} - \frac{\widehat{W}^2}{h_2 h_3}\frac{\partial h_3}{\partial \eta} &= -\frac{1}{\rho h_2}\frac{\partial p}{\partial \eta} \end{aligned} \tag{3.17}$$

following the derivation of Tannehill et al. (1997), where $h_1,\ h_2,\ h_3$ are given as

$$\begin{aligned} h_1 &= \sqrt{\left(\frac{\partial x}{\partial \xi}\right)^2 + \left(\frac{\partial y}{\partial \xi}\right)^2 + \left(\frac{\partial z}{\partial \xi}\right)^2} \\ h_2 &= \sqrt{\left(\frac{\partial x}{\partial \eta}\right)^2 + \left(\frac{\partial y}{\partial \eta}\right)^2 + \left(\frac{\partial z}{\partial \eta}\right)^2} \\ h_3 &= \sqrt{\left(\frac{\partial x}{\partial \zeta}\right)^2 + \left(\frac{\partial y}{\partial \zeta}\right)^2 + \left(\frac{\partial z}{\partial \zeta}\right)^2} \end{aligned} \tag{3.18}$$

The time derivative of $\widehat{V}$ is solved for analytically through the time dependence of the jet velocity. The ξ and ζ derivatives of $\widehat{V}$ are solved for analytically based on the specification of a paraboloid jet velocity distribution. The η-derivative is calculated using the one-sided explicit formulation, E4, from Table 2.2. The η-derivative of pressure, assumed the same as the normal direction, is then calculated using the same E4 formulation. Density is solved for using the ideal gas law.

Jet velocity is further specified by pulsing frequency and duty cycle (DC). The non-dimensional pulsing frequency is defined as

$$F^+ = \frac{f C_x}{U_{in}} \tag{3.19}$$

where U_{in} is the average velocity at the flow domain inlet (wind tunnel inlet in an experiment) and f is the dimensional frequency of the VGJ. For a selected value of the pulsing frequency the simulation time-step, Δt, is selected so that an integer number of time-steps represents one jet-cycle. The temporal profile of the VGJ was assigned using a piecewise combination of cubic and linear functions to approximate a square wave function. The piecewise combination was chosen in a way to ensure that the first-derivative was continuous for the proper calculation of the time derivative in Eq. 3.17. Duty cycle specifies how long the VGJ is active during a given jet-cycle; for example, a 50% duty cycle VGJ would be actively blowing for half the jet-cycle and would be off the other half. Figure 3.3 shows an example of the VGJ temporal profile. This particular profile reaches its defined velocity, U_{jet}, quickly, and then maintains this jet velocity for the remainder of the duty cycle (35% for this example). The quantity t/T of the abscissa describes the percentage of the jet-cycle that has occurred, where T is the jet-cycle period.

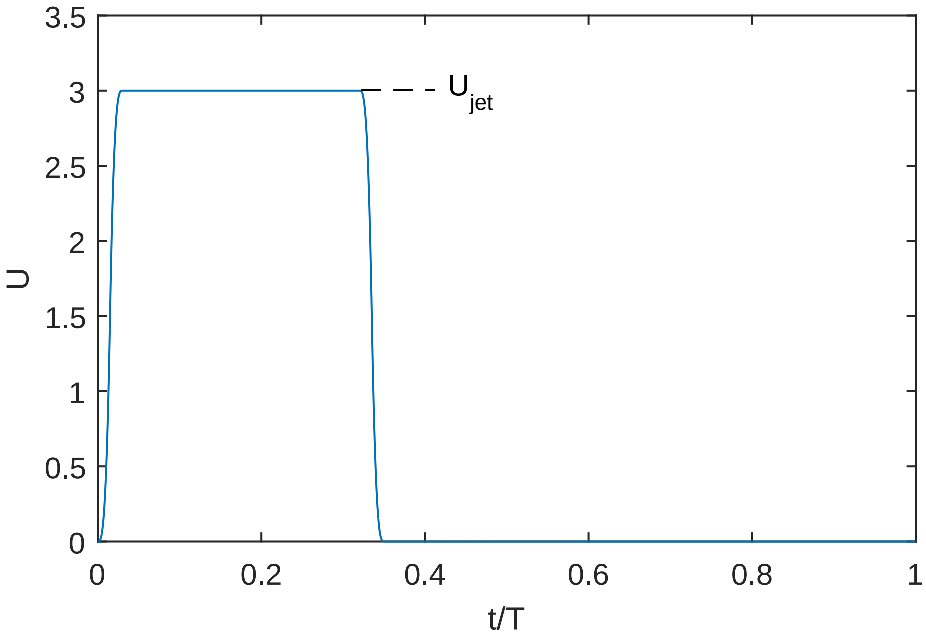

Figure 3.3: VGJ velocity time history

The VGJ boundary condition was implemented on a 13 x 13 square on the turbine blade surface. Poondru (2007) had simulated a jet in quiescent air and found that 11 points across the jet span were sufficient to accurately model the jet. While the

VGJ was active the above implementation specifying velocity and using the inviscid-normal-momentum equation was used but during the inactive phase of the jet-cycle the VGJ boundary defaults back to the turbine blade surface (i.e., the no-slip, adiabatic, solid wall).

Chapter 4

Grid and Validation Study

The current flow solver, FDL3DI, has been used extensively for steady and unsteady flow problems such as those mentioned previously in Chapter 2. Despite the extensive validation of FDL3DI, it is still necessary to understand program usage and implementation through simulation of an LPT flow. For the current study, a numerical setup was selected which corresponded with available experimental data for an LPT flow problem. Comparing computational results with experimental results serves the dual purpose of tutorial for FDL3DI and numerical validation for the software used. In tandem with this validation study, a grid-independence study was also conducted to further understand the mesh requirements for the LPT flows of interest.

4.1 Experimental Study

The current flow solver validation compares computational results with the experimental results of Volino et al. (2009) and Volino et al. (2011). Volino et al. (2009) conducted an experimental investigation of baseline and flow control cases using the L1A turbine blade. Flow control was implemented through the use of VGJs. This study used the L1A due to its aggressive lift characteristics and its high degree of separation which serves as a great test blade for flow control research. A wide range of cases were considered with varying jet pulsing frequencies, blowing ratios, and duty cycles. Additionally, these experiments were carried out for Reynolds numbers ranging from 25,000 to 100,000 (Re_{ex}) based on wind tunnel exit velocity and blade suction surface length, or equivalently, Reynolds number of 10,000 to 40,000 (Re_{in}) based on tunnel inlet velocity and axial chord length. The LPT cascade consisted of 7 turbine blades which provided for good periodicity between each blade and inlet freestream turbulence intensity (FSTI) was low at 0.6%. These conditions make this experiment more ideal for comparison with simplifying assumptions made in the current numerical setup. The second experiment, Volino et al. (2011), had the same setup as the first but had higher FSTI (4.9%) and a more limited Reynolds number range of $Re_{in} = 10,000$ to $20,000$. The higher FSTI provides a less favorable comparison with the current solver since the free-stream turbulence at the inlet in the computational domain inlet is not reproduced.

4.2 Numerical Setup

Based on the results available in these two experimental investigations, two setups were considered for the validation study. The first case, referred to as Case 1, represents a set of jet parameters which did not effectively mitigate separation. The second case, Case 2, corresponds to a well-controlled case where separation was reduced substantially. These cases represent both ends of the control spectrum and ideally, the simulation could capture the flow physics on both ends. Both cases were only considered at the lowest Reynolds number ($Re_{in} = 10,000$) where separation was the greatest in the baseline flow. Only the lowest duty cycle (10%) was considered since it was the most amenable to modeling as a square wave based on the jet profile that was measured in the experiment. The non-dimensional pulsing frequencies were 0.28 and 0.56 for Case 1 and Case 2, respectively. Non-dimensional frequencies in the experimental study is defined as

$$F^+_{ssj} = \frac{f L_{ssj}}{U_{ave}} \tag{4.1}$$

where L_{ssj} is the suction surface length from the VGJ hole to the trailing edge of the blade, and U_{ave} is the average local freestream velocity between the VGJ and the trailing edge. In order to calculate the non-dimensional frequency in terms of the inlet velocity and axial chord length the following equation can be used

$$F^+ = \frac{U_{ave}}{U_{in}} \cdot \frac{C_x}{L_{ssj}} \cdot F^+_{ssj} \tag{4.2}$$

Blowing ratio was set at 1.0 and 2.0 for Case 1 and Case 2, respectively. Reynolds number and non-dimensional frequencies were specified in terms of the inlet velocity and axial chord length for the current computation. A summary of the overall setup is shown in Table 4.1.

Table 4.1: Summary of Volino experimental setup and current numerical setup

Setup	Parameter	Case 1	Case 2
Experimental	Re_{ex}	25,000	25,000
	F^+_{ssj}	0.28	0.56
Numerical	Re_{in}	10,000	10,000
	F^+	0.7565	1.5130
Both	BR	1.0	2.0
	DC	10%	10%

In order to calculate the average local freestream velocity (U_{ave} required for getting frequency based on inlet conditions and axial chord) and the local freestream velocity (U_{local} used to define blowing ratio) an attached surface pressure distribution is needed for the L1A blade. This attached profile was obtained from the inviscid coefficient of pressure profile given in Volino et al. (2009). This profile is shown in Fig. 4.1. In this

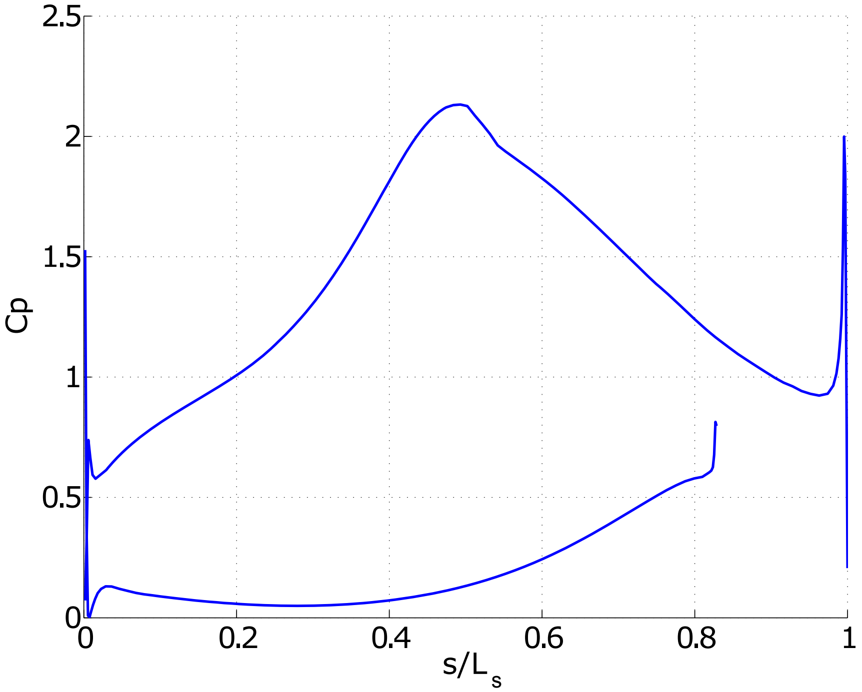

Figure 4.1: Inviscid surface pressure distribution for the L1A turbine blade

figure C_p is defined as

$$C_p = \frac{2\left(p_t - p\right)}{\rho U_{ex}^2} \tag{4.3}$$

where U_{ex} is the velocity at the wind tunnel exit and p_t is the upstream total pressure. Note that the point of peak suction occurs at $s/L_s = 0.5$; hence, this point is the optimal position of jet implementation for flow control.

In addition to implementation details given above, the jets were specified in the same configuration as Volino et al. (2009). The jet diameter was set at $0.006C_x$, jet spacing at $0.0636C_x$ (spanwise extent of computational mesh), jet pitch angle at $\theta = 30°$, and the jet skew angle at $\phi = 90°$. The jet location was set at $s/L_s = 0.5$, where s is the arc length along the suction surface from the blade's leading edge to the jet location and L_s is the total suction surface length. This corresponds to a position, in terms of the axial chord, of $x/C_x = 0.62$. This jet configuration is the same for all of the cases that are given in the experimental study.

The final settings for the jet consider the temporal aspects of the jet. From the non-dimensional frequency, F^+, a corresponding frequency based on the reference velocity can be calculated as

$$F_\infty^+ = \frac{fC_x}{U_\infty} = U_{in}F^+ \tag{4.4}$$

and subsequently, the jet period can be calculated. For the validation study, a time step of $\Delta t = 6.734473e^{-4}$ was selected which allowed for an integer number of solver iterations to simulate one jet-cycle. This time step corresponds to 3,336 $^{\text{iterations}}/_{\text{jet cycle}}$ for Case 1 and 1,668 $^{\text{iterations}}/_{\text{jet cycle}}$ for Case 2. As described in Section 3.1, the solution was initialized from the final results of the Reynolds Number iteration runs. This was a well-developed baseline solution. In case 1, the solution was allowed to develop for 3 jet-cycles before time averaging and data collection commenced over another 4.5 jet-cycles. In case 2, there were 6 jet-cycles for the transient run and another 10 for the data run. Each of the transient runs was executed for 6.7399 non-dimensional time units. The data run for Case 1 ran for 10.0855 non-dimensional time units and Case 2 for 11.2223-time units.

4.3 Meshing Details

There were three meshes that were developed for the grid-independence study. These meshes had approximate sizes of 3, 5, and 7 million grid points; thus, these meshes are referred to as coarse, mid, and fine, respectively. Each mesh was created with a background H-grid to compute the flow through the turbine channel while the details around the blade were captured with a highly refined O-grid. Most grid points were contained in the O-grid around the blade. The 3 million point mesh contained a background H-grid with 319 x 138 x 17 points in the streamwise, cross-flow, and spanwise directions, respectively. The number of spanwise points of the H-grid was selected to obtain a mesh spacing of $\Delta z \approx 0.004$ which Poondru (2007) had concluded is high enough resolution to resolve the flow in the spanwise direction based on the work of Rizzetta and Visbal (2003*b*). The corresponding O-grid had 563 x 85 x 47 points. Points were clustered for the streamwise direction in the aft section of the suction surface since this is where the separated shear layer interacts with the main flow and potential reattachment occurs. The aft portion of the suction surface contained 35.5% of all the points in the O-grid. Points were also clustered in the vicinity of the VGJ hole to help capture the flow physics there. For the VGJ, hole points were clustered in both the streamwise and spanwise direction with 13 points across the jet diameter. The first grid point at the wall was set at $\Delta n = 0.0007$. A screenshot of the mesh for the aft end of the blade is shown in Fig. 4.2 and shows the clustering of points near the VGJ location and in the aft section of the blade.

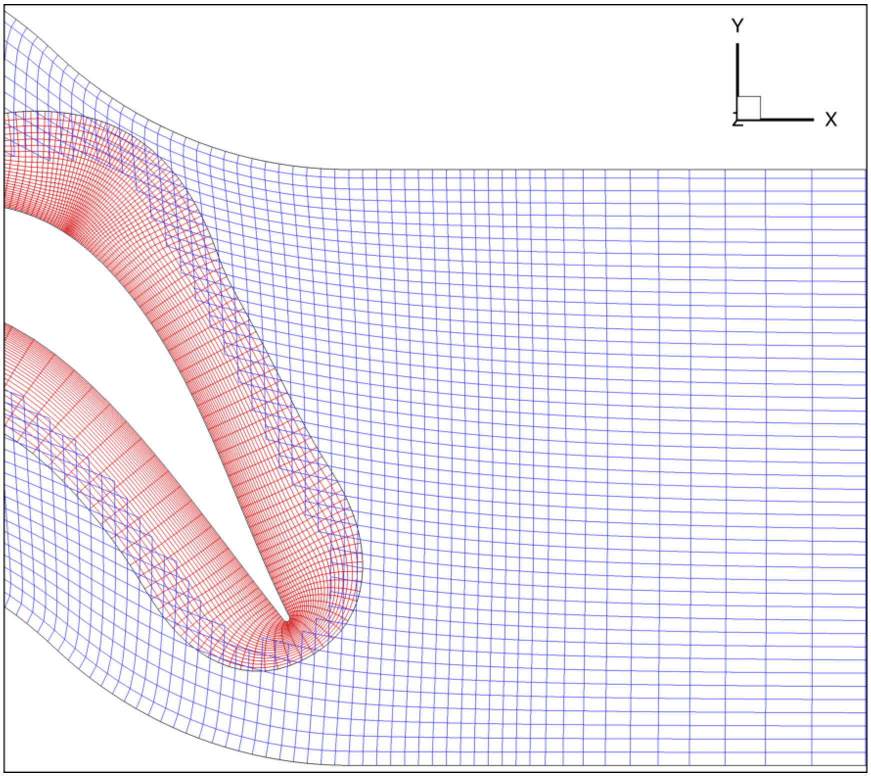

Figure 4.2: Screenshot of H-O grid setup for 3 million L1A mesh (aft end of blade, every 3rd grid point shown)

Each refinement of the mesh increased points in all areas of the mesh but concentrated this increase to the suction surface of the turbine blade, particularly the aft section of the blade. The 5 million point mesh H-grid contained 397 x 185 x 17 points. The O-grid had 649 x 105 x 55 points with 37.6% of these points concentrated in the aft portion of the suction surface, and the first point away from the wall was at $\Delta n = 0.00035$. The 7 million point mesh H-grid had 474 x 217 x 17 points. The O-grid consisted of 700 x 119 x 63 points with 39.1% of the points concentrated in the aft suction surface, and the first grid point from the wall at $\Delta n = 0.00025$.

Mesh resolution given in wall units is shown in Table 4.2 for Cases 1 and 2. The wall reference conditions used to normalize values is based on the time-averaged flow conditions at $0.5C_x$ where the boundary layer is fully developed, attached, and steady. The mesh sizes Δs^+, Δn^+, Δz^+ are for the streamwise, normal, and spanwise directions, respectively. Both the minimum and maximum values are shown.

Table 4.2: Computational mesh size given in wall units for Cases 1 and 2

Case #	Mesh Size	Δt^+	Δs^+_{min}	Δs^+_{max}	Δn^+_{min}	Δn^+_{max}	Δz^+_{min}	Δz^+_{max}
Case 1	3,000,000	0.13	0.88	25.53	1.10	1.30	0.88	6.93
	5,000,000	0.12	0.88	23.35	0.58	0.64	0.88	5.02
	7,000,000	0.11	0.85	21.63	0.40	0.44	0.85	3.70
Case 2	3,000,000	0.14	0.93	26.73	1.15	1.35	0.93	7.26
	5,000,000	0.15	0.95	25.41	0.63	0.69	0.95	5.46
	7,000,000	0.15	0.97	24.71	0.46	0.50	0.97	4.23

The results of the grid study on the L1A were used to approximate the meshing requirements for the L2A blade simulations, presented in Chapter 5. This approximation was considered valid for the current problem due to the similarity of the L1A and L2A blades. Both blades have the same inflow and outflow design angles, similar points of separation, similar loading profiles (both aft-loaded), and similar blade pitch. Given these similarities the mesh for the L2A blade was created in a similar fashion to that for the L1A blade.

4.4 Reynolds Number Iterations

For the Reynolds Number iteration a baseline flow mesh (span $= 0.2C_x$) similar to the 3 million mesh described above was used to quickly iterate through the Re_∞ value. This resulted in the values seen in Table 4.3. With the value of U_{in} for the given value of Re_{in} the jet frequency could be calculated and the time-step for the simulation of Cases 1 and 2 set. As the flow solution develops with flow control, the value of Re_{in} will increase because of the reduced blockage through the turbine passage. There was no attempt to correct Re_{in} after the flow control solution had developed as this would have been a very time-consuming process iterating between baseline and flow control Re_∞ values.

Table 4.3: Re_∞ iteration results to obtain desired $Re_{in} = 10,000$

Re_∞	Re_{in}	U_{in}
16,967	10,005	0.5883875

4.5 Results

The following sections present comparisons between the current computation and experimental results. Computational results are compared for each of the 3 meshes to try and achieve a solution which is grid independent. Results are presented as time-averaged surface pressure distributions, wake loss profiles, blade normal velocity magnitude, blade normal fluctuating velocity magnitude, cross-flow vorticity iso-surfaces, and streamtraces. Case 2 also includes phase-averaged spanwise vorticity, and phase-averaged blade normal velocity magnitude. Phase-averaged results were obtained by taking the instantaneous flow solution at a given time during the jet-cycle and averaging these results across multiple jet periods. Figure 4.3 shows a diagram of the locations where blade normal profiles were collected. All data presented is extracted from points located in-between the jets on the periodic spanwise domain boundaries, unless otherwise stated.

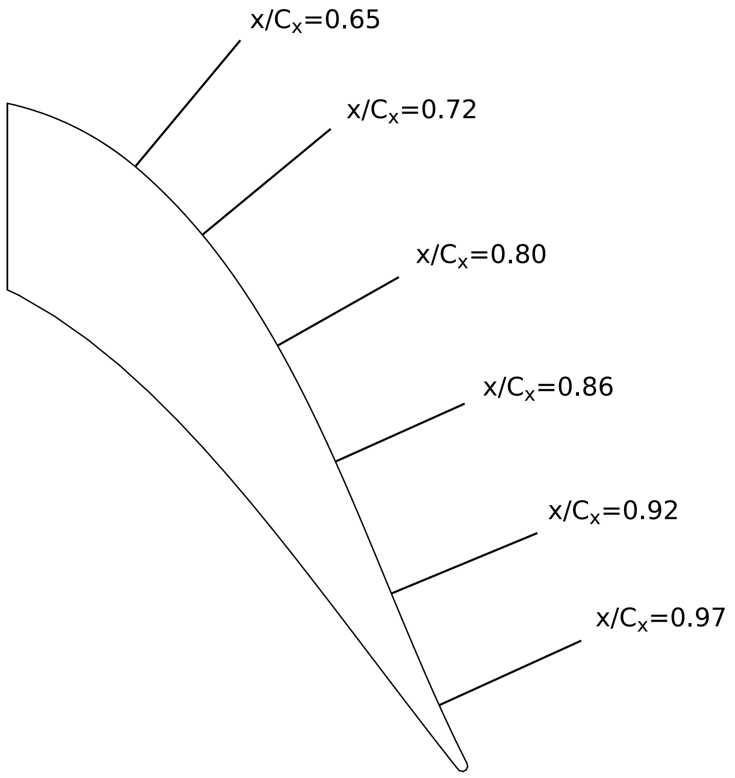

Figure 4.3: Blade normal profile locations for L1A blade

4.5.1 Case 1

The first case corresponds to a jet setup which did not provide adequate control of separation in the experiments of Volino et al. (2009) and Volino et al. (2011). Numerical results for the surface coefficient of pressure are compared with both experiments and are shown in Fig. 4.4. The coefficient of pressure here is defined in Eq. 4.3. The first item to note is the difference in the experimental results. The only differences between the experiments are the levels of FSTI with 0.6% in the experiments of Volino et al. (2009) and 4.9% in the study of Volino et al. (2011). This indicates the large effect the FSTI can have downstream at the turbine cascade. Overall, the numerical results compare better with the higher freestream turbulence experiment which is an unexpected result. While the experimental and numerical results do not agree quantitatively, the trends are very similar. A quantitative bias seems to exist between the numerical and experimental results in the aft suction surface and the fore pressure surface. A similar bias can be seen in the computational and experimental comparisons of Volino et al. (2009) which could be indicative of similar differences between the experimental and computational setup. Both mid- and fine-grids match identically on the pressure surface but deviate on the suction surface just before peak suction around $x/C_x = 0.45$. Both coarse- and mid-grids agree with the experiments on the point of peak suction while the fine-grid predicts peak suction upstream of the other cases. All grids maintain the characteristic plateau that is representative of separated flow and never show a distinctive reattachment which would be indicated by a rapid decrease in the coefficient of pressure. Both mid- and fine-grids capture the slight increase in coefficient of pressure that occurs at $x/C_x = 0.8$ for both experimental studies. Overall, the mid-sized grid compares the best with the experimental results of Volino et al. (2011) maintaining a similar rise on the fore section, achieving the same point of peak pressure, maintaining the pressure plateau, and capturing the slight increase in coefficient of pressure in the aft section. One consideration that can affect the comparison with experimental results is blade periodicity. The setup of both experiments made no attempt to correct the wind tunnel flow to ensure periodicity in the case of separated flow. This was done in order to ease experimental setup and was considered an acceptable trade-off since the aim was to find cases which provided adequate control of separation. Case 1 here was a flow control case which did not effectively control separation and so would suffer from a reduction in periodicity in the experiment. Two other considerations are the spanwise and cross-flow effects of the wind tunnel walls. In the spanwise direction, the walls will cause secondary end wall effects at the end of the blades. This effect can propagate into the midspan section of the blade and affect results. Also, the walls in the cross-flow direction will help turn the flow just downstream of the blade which effectively reduces separation on blades with suction surfaces closer to the wind tunnel walls. Both of these conditions will affect the separation characteristics of the blade and can cause differences with the simulation result as seen here.

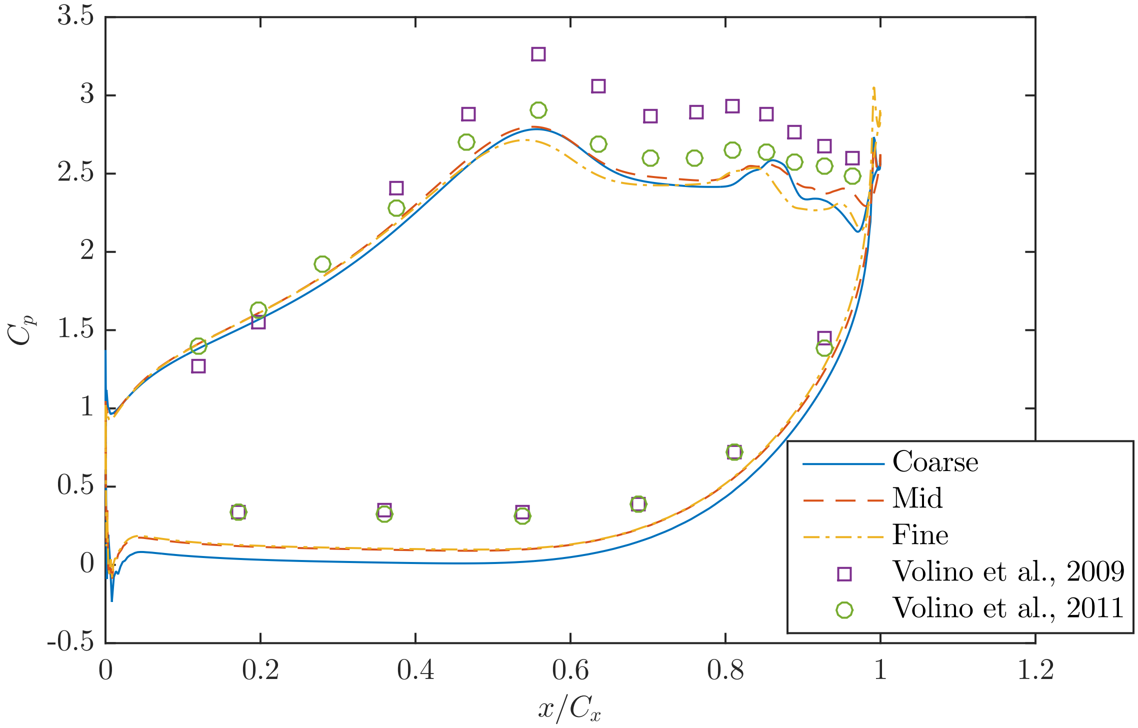

Figure 4.4: C_p surface distribution for Case 1

Next, results for the time-averaged wake loss coefficient are given in Fig. 4.5. Wake loss coefficient is defined as

$$\psi = \frac{p_t - p_{t,e}}{p_t - p} \tag{4.5}$$

where $p_{t,e}$ is the total pressure at the cross-flow location where the wake loss is calculated. Wake loss values are extracted from a plane in the pitch axis of the turbine cascade (pitch is perpendicular to the axial direction). y/C_x is a non-dimensional indication of the location in this plane. Increasingly positive values of y indicate moving up from the suction surface of the turbine blade toward the pressure surface of the adjacent blade. The location $y/C_x = 0$ is the axial projection of the blade trailing edge onto the plane where results are calculated. The results given here show that all grids agree in trend. The mid- and fine-grids match well approaching the wake disturbance, caused by flow separation, from the pressure surface. The wake loss maximum value increases as the grid is refined suggesting that the fine-grid computes a larger amount of separation and thus higher losses. Also, the more refined the grid becomes the wider the wake loss disturbance becomes. The discrepancies found here between the three grids indicate that for the failed control case there is a high degree of unsteadiness potentially requiring a more refined mesh.

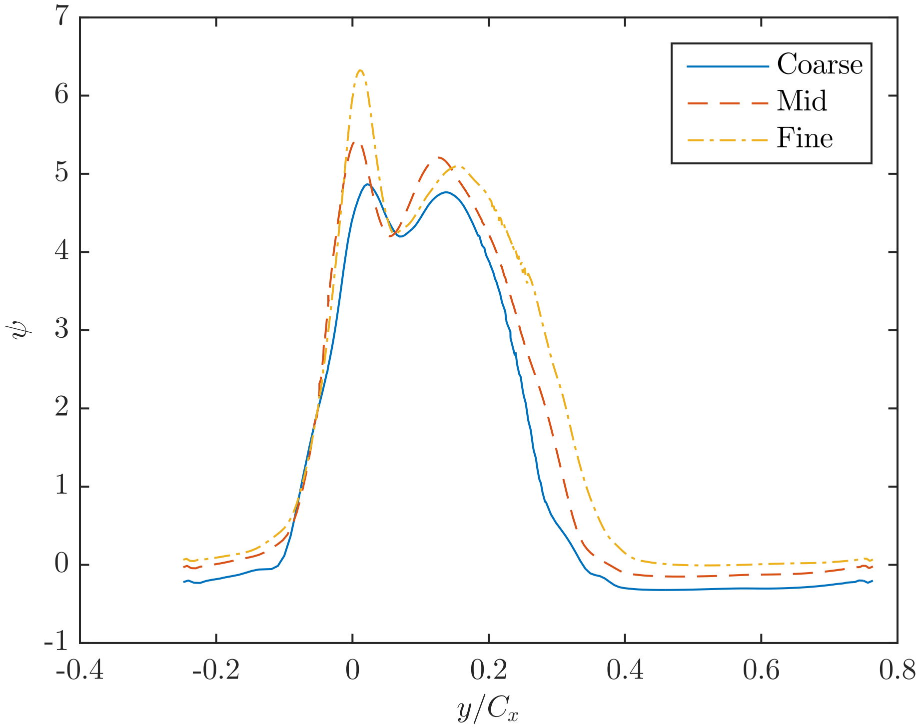

Figure 4.5: Wake Loss coefficient at $x/C_x = 1.05$ for Case 1

Time-averaged velocity magnitude profiles normal to the blade surface are shown in Fig. 4.6. The x-axis is shifted for each of the blade normal profiles for clarity. Results are displayed at the 6 streamwise stations shown in Fig. 4.3. At the first station, $x/C_x = 0.65$, the velocity profile for all three grids are nearly identical and flow is still attached. By $x/C_x = 0.72$, the boundary layer has separated as indicated by the small region of zero wall normal velocity gradient. At each subsequent station the size of the separation bubble increases as the shear layer moves further from the blade surface. The shear layer here is indicated by the region where velocity magnitude monotonically increases to the freestream value with a concave up profile. Even at $x/C_x = 0.97$, the velocity gradient suggests that the flow is still not attached as indicated by the non-monotonically increasing velocity value. For this case, the boundary layer has not attached indicating an open separation bubble. Once separation has occurred the coarse- and mid-grids match mostly with the mid-grid predicting a slightly larger separation zone. The fine-grid predicts a larger separation bubble than the other two grids. These results are consistent with those found for the wake loss results given in Fig. 4.5.

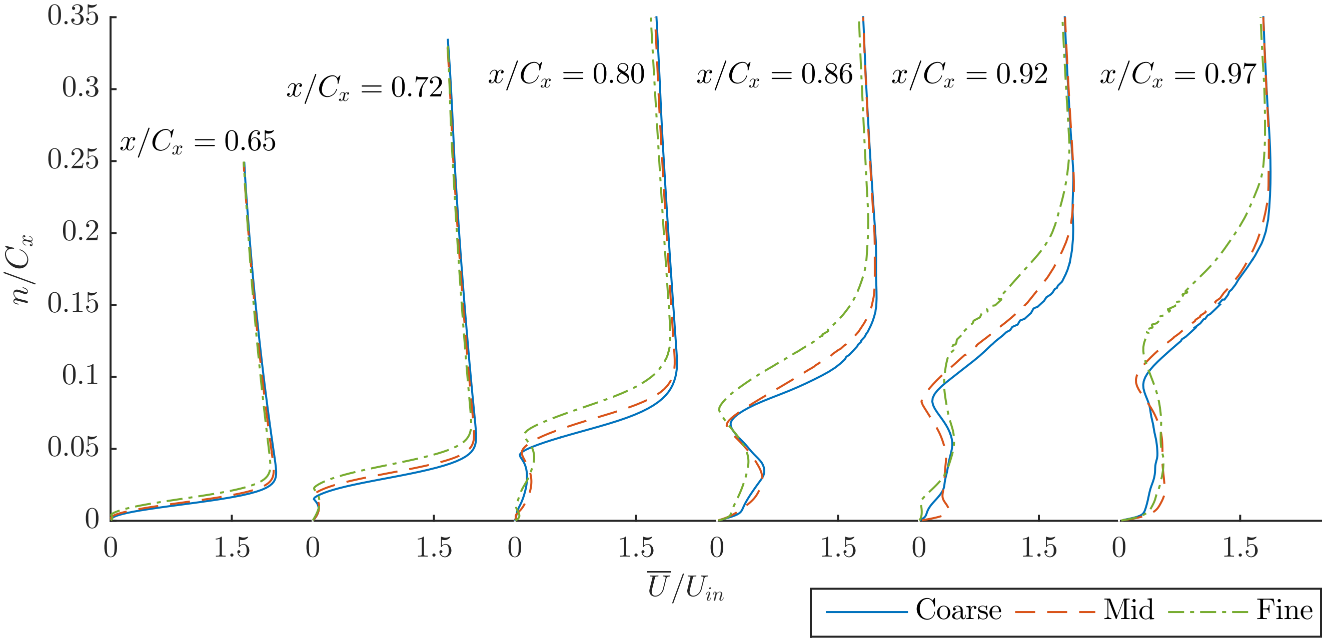

Figure 4.6: Time-averaged blade normal velocity magnitude profiles at six streamwise stations, Case 1

The root-mean-square fluctuating velocity magnitude blade normal profiles are shown in Fig. 4.7. The profiles here are shifted on the x-axis just as in the velocity magnitude profiles to clarify the distinct streamwise locations. Results are again displayed at the six streamwise stations shown in Fig. 4.3. The first station at $x/C_x = 0.65$ shows low levels of fluctuating velocity. This is consistent with the velocity magnitude profiles showing the flow is still attached at this point but it is getting ready to separate. The peak in fluctuating velocity seen here is indicative of the unsteadiness in the boundary layer. All three meshes at this point agree well. At $x/C_x = 0.72$ the boundary layer has separated and the peak in fluctuating velocity represents the separated shear layer which has moved away from the blade surface. The peak in fluctuating velocity is further away from the blade for the fine-case which is consistent with other results indicating a larger degree of separation. Further downstream at $x/C_x = 0.80$, the shear layer has moved even higher as indicated by the fluctuating velocity peak and again the peak is higher for the fine-grid because of larger separation. At both stations, $x/C_x = 0.72$ and 0.80 the coarse- and mid-grids have similar peak fluctuating velocity locations and profiles after the peak has been reached. The last three stations ($x/C_x = 0.86,\ 0.92$ and 0.97) do not exhibit a distinctive peak in the fluctuating velocity but show high levels of unsteadiness all through the separated region. This unsteadiness increases moving further downstream and may indicate possible transition is occurring. The last three stations have different profiles for all three grids which are probably caused by the high degree of unsteadiness in this region.

Iso-surface images of the time-averaged cross-flow vorticity on the aft portion of the blade are shown in Fig. 4.8 for all three mesh sizes. The plot shows iso-surfaces for cross-flow vorticity of $\Omega_y = 1.0$ and is colored by the velocity magnitude. All three meshes show a similar vortical structure coming off the VGJ and all capture the fine scales that are inherent with the large separation occurring at low-Reynolds number. The coarse-mesh differs from the other two with a large vortical structure extending further upstream on the blade and with some vortical structures with higher velocity

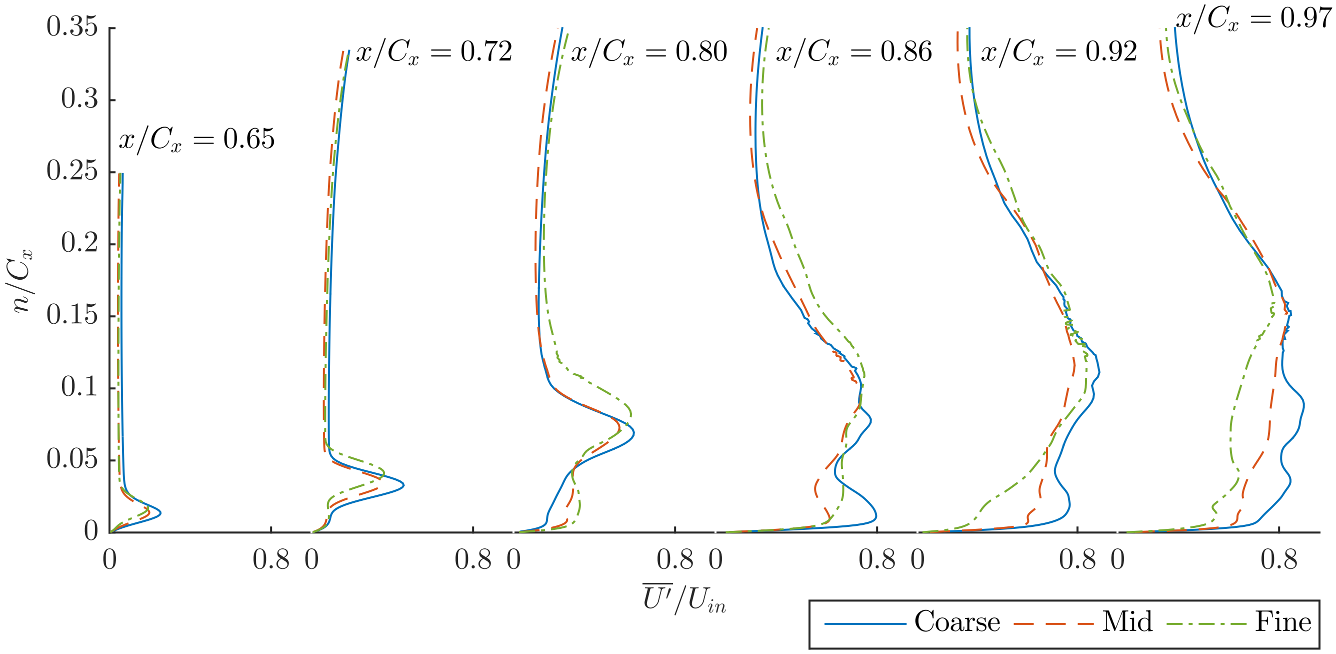

Figure 4.7: Time-averaged blade normal root-mean-square fluctuating velocity magnitude profiles, Case 1

magnitudes.

Time-averaged streamlines for the aft section of the blade are shown in Fig. 4.9 for all three meshes. These results indicate that the separation bubble increases in size as the mesh is refined with the appearance of larger recirculation zones. This result is consistent with the other results mentioned previously.

In summary, results of the simulation for Case 1 show ineffective control of separation as was the case in the experimental studies of Volino et al. (2009, 2011). The current computations did not effectively control separation with large separation still occurring on the aft portion of the blade. Three meshes of increasing refinement were used in the computation. In comparing to experimental surface coefficient of pressure results the mid sized mesh had the most favorable comparison and matched the trend of the experimental data while still differing quantitatively. This discrepancy was most likely caused because of differences between the numerical and experimental setup. A similar discrepancy was found between the experimental and computational

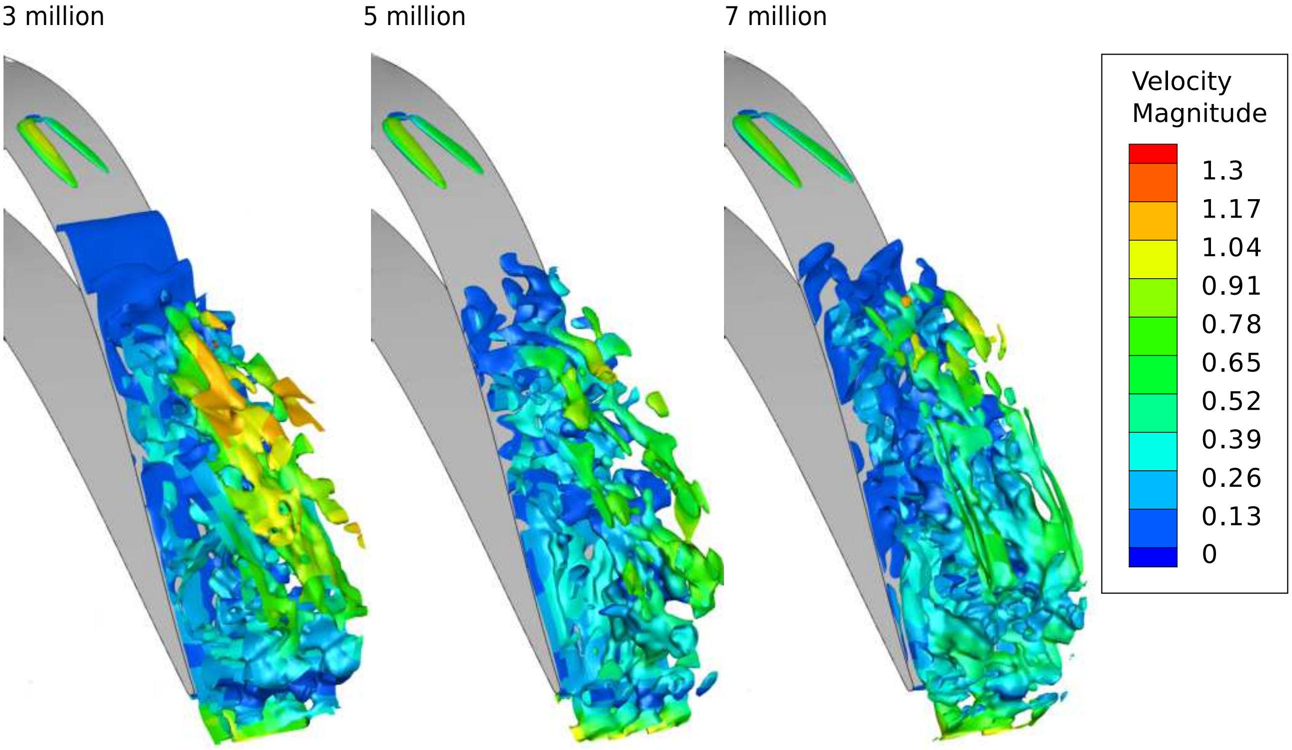

Figure 4.8: Time-averaged iso-surface image of cross-flow vorticity ($\Omega_y = 1.0$), colored by velocity magnitude, Case 1

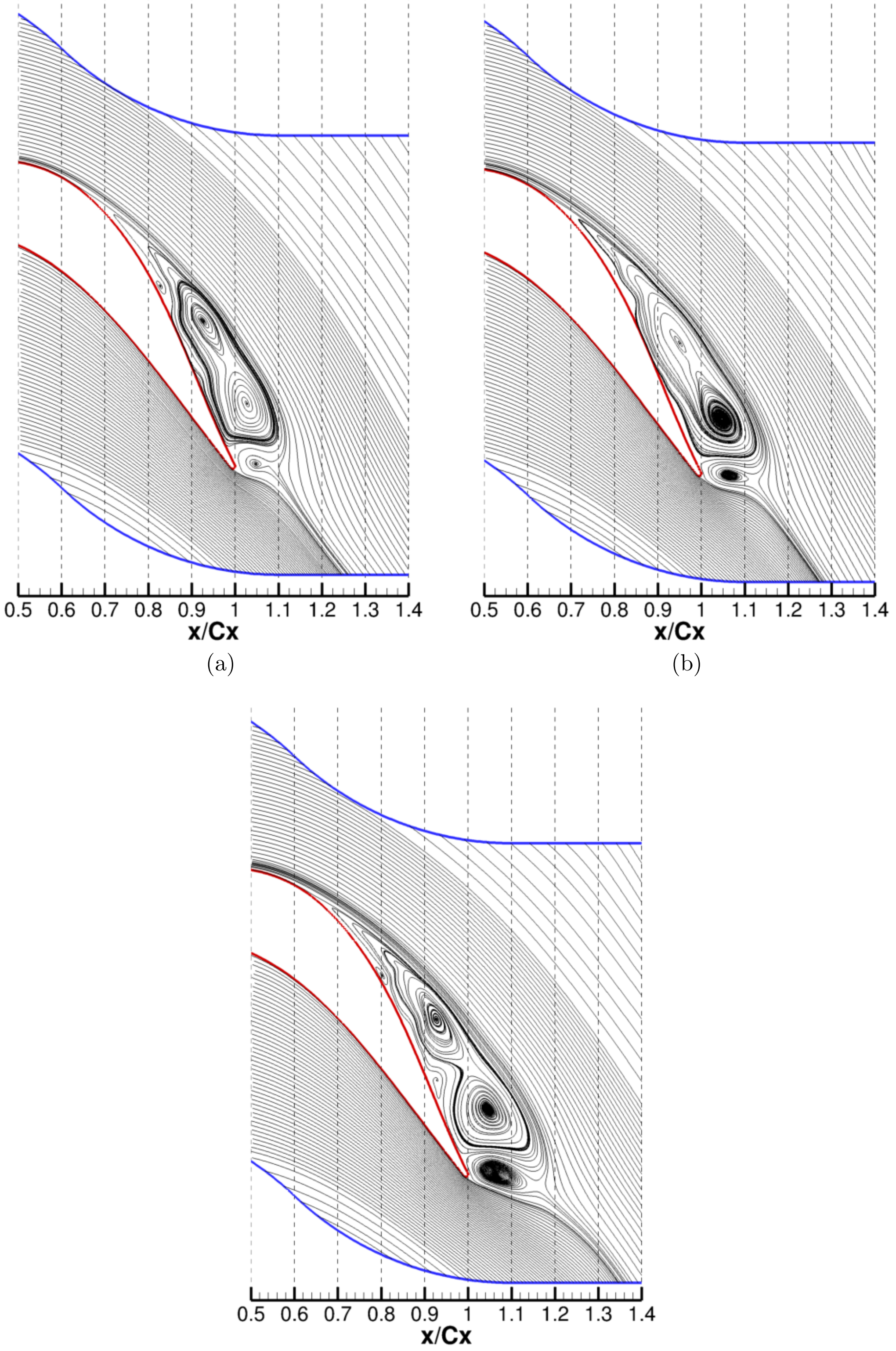

(a)

(b)

(c)

Figure 4.9: Time-averaged streamlines for (a) coarse, (b) mid, and (c) fine meshes, Case 1

results in Volino et al. (2009). Other results are displayed to show comparisons between the different mesh sizes. Most of these results indicate the same behavior with increasing mesh refinement resulting in larger degrees of separation. The massive separation that was present in these simulations makes for a highly unsteady problem and likely exacerbates the differences between the mesh sizes thus causing their results to be different. The high degree of unsteadiness could also make time-averaging more difficult as the solution is rapidly changing. It is possible that time-averaging over a longer time interval would have provided a better comparison between the different mesh sizes.

4.5.2 Case 2

The second case corresponds to a setup which successfully mitigated, not eliminated, the separation on the L1A blade in the experimental studies of Volino et al. (2009, 2011).

The time-averaged surface coefficient of pressure distributions are compared with both experiments and shown in Fig. 4.10. Similar to Case 1 the results between the two studies by Volino are different likely due to the differences in FSTI. As in the results of Case 1, the computational results match better with the experiments conducted with higher levels of FSTI. Again, this is an unexpected result as the numerical simulation does not simulate the effects of freestream turbulence. Numerical results match very well on the pressure surface of the blade but compute a lower coefficient of pressure on the suction surface indicating a lower amount of separation in the experiments. Both mid- and fine-grids match very well in this computation and approximate the experimental results nicely. Both compute the same point of peak suction at $x/C_x = 0.59$ and compare well with the experiments. Transition is characterized by a sharp drop in the coefficient of pressure after the plateau inherent with separation. After transition the flow can reattach which would be indicated by a coefficient of pressure value approximating the fully-attached flow C_p value. Both mid- and fine-grids appear to begin transition at $x/C_x = 0.77$ which is slightly earlier than the experiments at $x/C_x = 0.81$. Just after transition the mid- and fine-grids deviate slightly and are most different near the trailing edge where reattachment is possible. The coarse-mesh differs from both the mid- and fine-grids and does not match the experimental results as well as the other two grids. Overall, the mid- and fine-grids match each other very well and approximate the trends in the experimental results of Volino et al. (2011) best. These results maintain a similar rise in coefficient of pressure on the fore section of the blade, compute the same point of peak suction, and exhibit a similar point of transition. The differences between computational and experimental results are likely the result of differences in problem setup. Namely, the effects of the wind tunnel walls were not accounted for in the simulation. Compared with the results of Case 1 in Fig. 4.4 the results here show larger values of the coefficient of pressure which is consistent with the reduction of separation in this case.

Time-averaged wake loss coefficient is shown in Fig. 4.11. Again, positive y/C_x indicates movement from the pressure surface toward the suction surface. The coarse-mesh differs from the results of both the mid- and fine-mesh, and even computes a non-zero loss outside of the immediate wake of the turbine blade. Both mid- and fine-meshes agree well outside of the blade wake region with both giving near zero loss as the results should indicate in this region. Approaching the blade wake region from the pressure surface the mid- and fine-meshes are identical as the wake loss rises but then deviate with the mid-mesh predicting higher losses and a wider wake region. Then both mid- and fine-meshes are again identical outside the wake region. These results indicate a smaller degree of separation in the fine-mesh. By comparing these results with the wake loss in Fig. 4.5 for Case 1 one can see that the wake loss has been reduced both in loss value and the size of the wake loss region for all

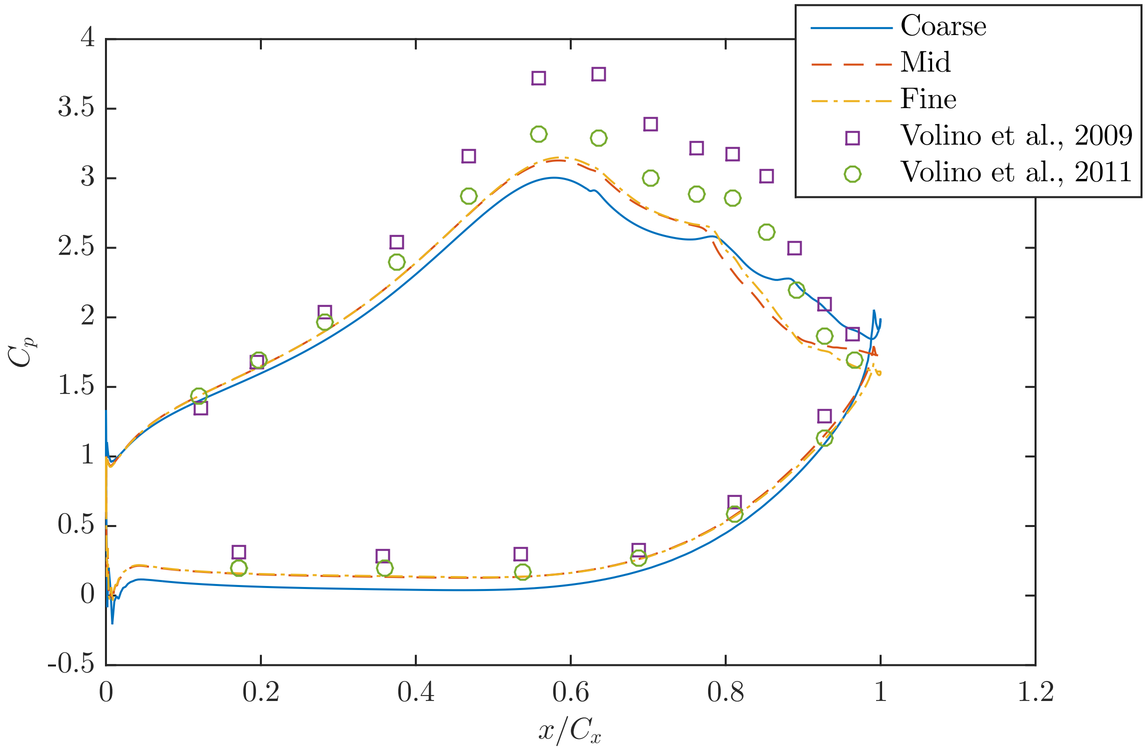

Figure 4.10: C_p surface distribution for Case 2

meshes. This is consistent with the results of coefficient of pressure and the reduction of separation present in this flow control case.

Next, time-averaged velocity magnitude profiles normal to the blade surface are shown in Fig. 4.12 and compared with experimental values from Volino et al. (2011). The x-axis is shifted for each of the profiles for clarity of the display. Results are displayed at the six streamwise stations shown in Fig. 4.3. Station $x/C_x = 0.65$ shows identical profiles for all three grids that match very well with experimental data and display attached flow. At $x/C_x = 0.72$ all grids and experimental data show the beginning of flow separation; however, the coarse-grid calculates a larger degree of separation while the mid- and fine-grids predict a smaller amount of separation consistent with the experimental results. Station $x/C_x = 0.80$ shows more separation with the coarse-mesh again predicting larger separation than any other result. The mid- and fine-grids agree very well and match with experimental data after a short

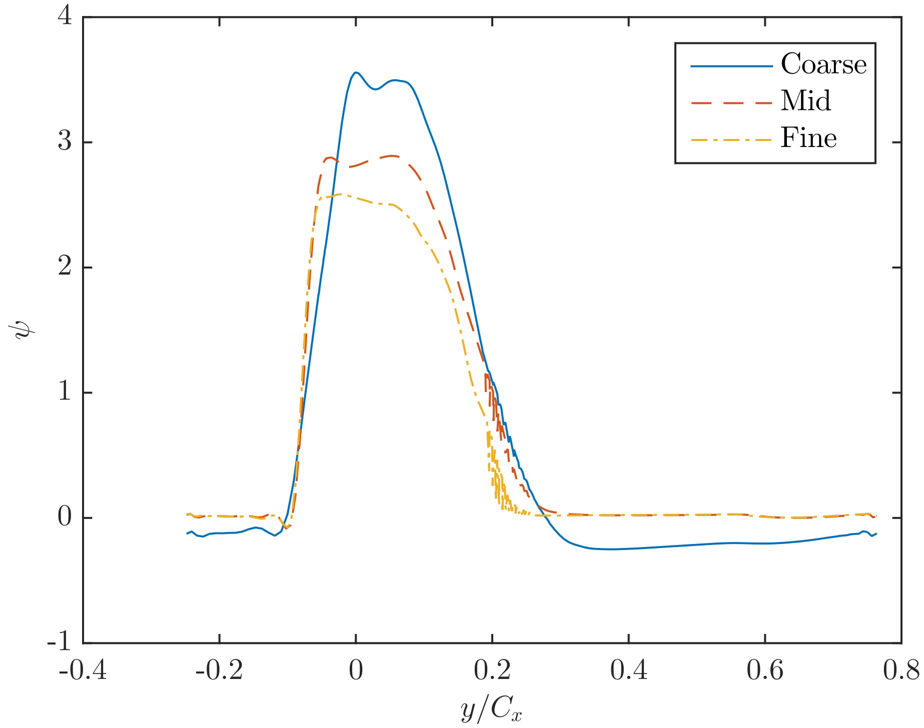

Figure 4.11: Wake Loss coefficient at $x/C_x = 1.05$ for Case 2

deviation just above the blade surface. By station $x/C_x = 0.86$ the experimental data has begun to deviate from the other results showing less separation, but it still matches with the mid- and fine-grids outside the separation bubble. The coarse-mesh computes the largest separation while the mid- and fine-meshes agree in trend but differ slightly in values. At $x/C_x = 0.92$ and 0.97, the experimental data indicates that the flow is reattached; although, the velocity normal gradient is gradual. Both mid- and fine-meshes show possible reattachment at $x/C_x = 0.97$ where the velocity profile continuously increases from the blade surface. Both these meshes disagree with the experimental results inside the separation bubble but agree outside the bubble. The coarse-mesh is not consistent with either meshes or the experiments. Overall, these results show a good comparisons between the mid- and fine-meshes. Both these meshes match experimental data before the separation bubble becomes large at which point the results deviate inside the separation bubble but agree outside it in the freestream. The experimental results show a lesser degree of separation which is consistent with the results shown for the coefficient of pressure.

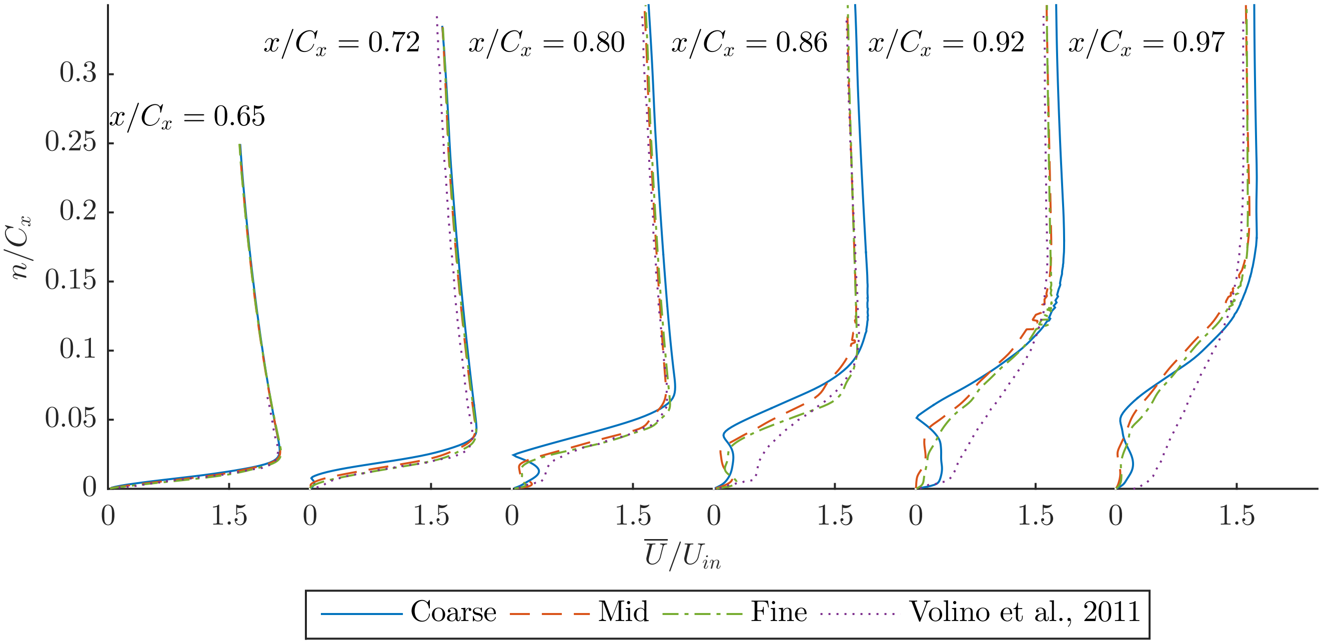

Figure 4.12: Time-averaged blade normal velocity magnitude profiles at six streamwise stations, Case 2

The root-mean-square fluctuating velocity magnitude blade normal profiles are shown in Fig. 4.13 for all meshes and compared with experimental data of Volino et al. (2011). The profiles here are shifted on the x-axis for better display. Results are displayed at the six streamwise stations shown in Fig. 4.3. The first station at $x/C_x = 0.65$ shows a smaller amount of fluctuating velocity in the experiment compared with the numerical results. The coarse-mesh has a distinctive peak in fluctuation levels which are indicative of the unsteadiness in the boundary layer introduced by the VGJs. Both mid- and fine-grids have multiple peaks which implies a greater degree of unsteadiness in the boundary layer. This is likely caused because the increased refinement was able to better capture the increased unsteadiness caused by the VGJs. By $x/C_x = 0.72$ the boundary layer has separated. Here the experiment measured a similar amount of fluctuating velocity compared with numerical results.

Quantitative measures of the fluctuating velocity do not agree, but the trend of experimental results agrees with the mid- and fine-grids and matches very well outside the separation bubble. The coarse-mesh predicts a single peak in fluctuating velocity which is higher than the other results, indicating a greater degree of separation. This is consistent with the results of the velocity magnitude profiles. Downstream at the $x/C_x = 0.80$, 0.86, 0.92, and 0.97 stations, the levels of fluctuating velocity continue to grow for the coarse-mesh which calculates higher levels of unsteadiness than the other meshes. This indicates a higher degree of separation. The mid- and fine-meshes continue to match fairly well in trend while the quantitative values differ slightly. These meshes also agree with the trend of experimental data while predicting larger levels of fluctuating velocity, indicating greater separation in the numerical results. This is consistent with the other results discussed so far. Outside of the separation bubble, the mid- and fine-meshes agree very well with the experimental results. Compared with the results of Case 1, results here show lower levels of fluctuating velocity which is consistent with the reduced separation.

Time-averaged cross-flow velocity iso-surface images are shown in Fig. 4.14 for all three meshes in the aft portion of the blade. The plots show iso-surfaces for cross-flow vorticity of $\Omega_y = 1.0$ and are colored by velocity magnitude. The large vortical structures that are present represent the interaction of the vortices resulting from the VGJ with the shear layer. This interaction is similar in the mid- and fine-meshes while the coarse-mesh presents smaller vortical structures. Underneath the interaction in the shear layer, the fine scales associated with large separation at low-Reynolds number seem to be captured by all three meshes.

Time-averaged streamlines for the aft section of the blade are shown in Fig. 4.15 for all three meshes. These results show a larger amount of recirculation in the coarse-mesh solution while the flow solutions for the mid- and fine-meshes are more similar with the mid-mesh calculating a slightly larger separation bubble. Overall

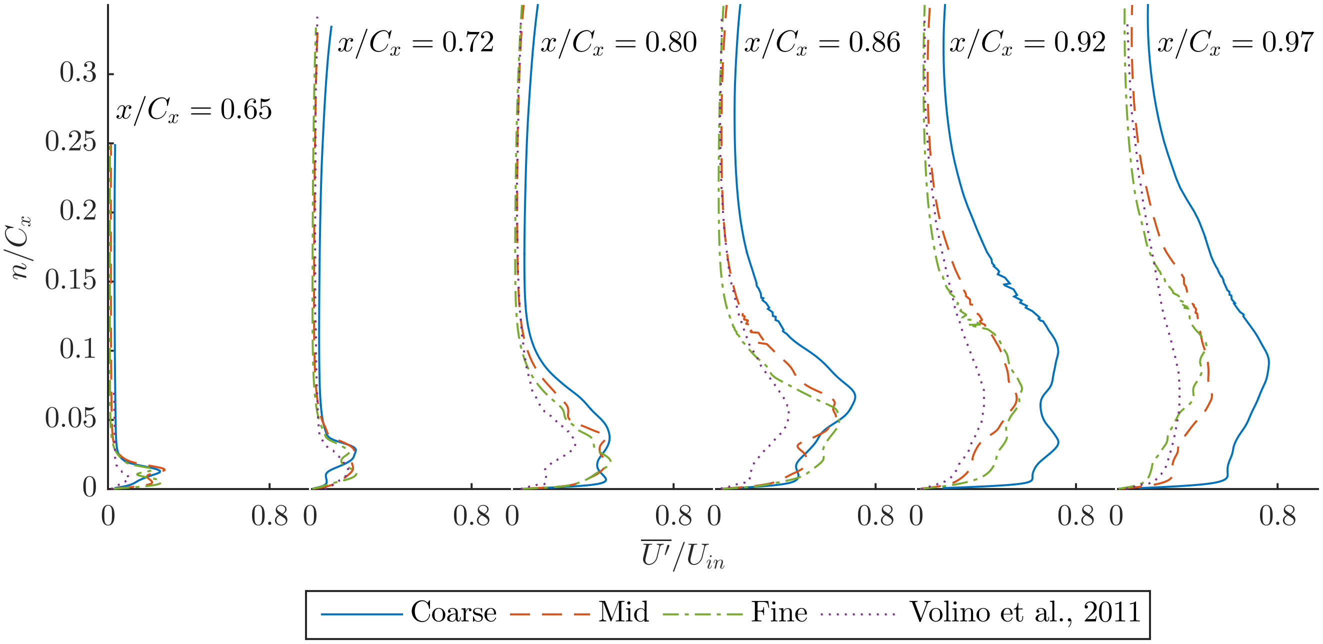

Figure 4.13: Time-averaged blade normal root-mean-square fluctuating velocity magnitude profiles, Case 2

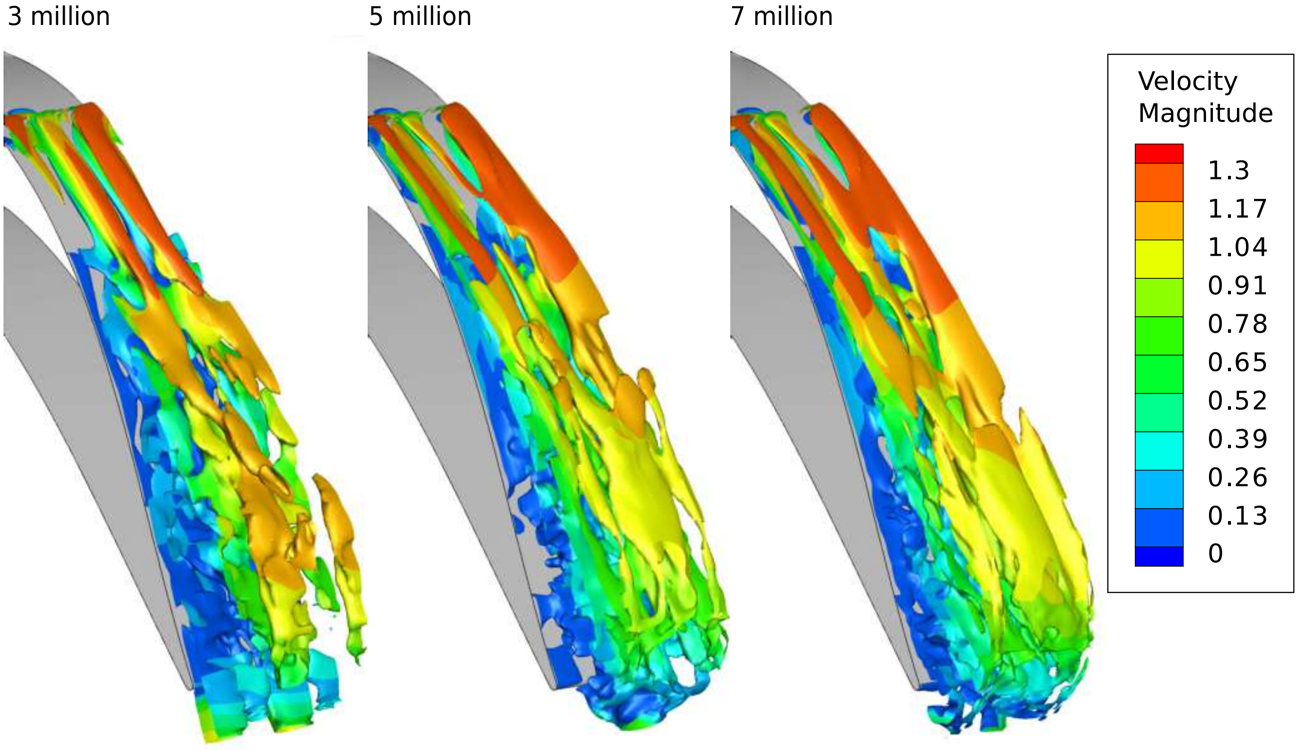

Figure 4.14: Time-averaged iso-surface image of cross-flow vorticity ($\Omega_y = 1.0$), colored by velocity magnitude, Case 2

the mid- and fine-meshes agree well with each other. Comparing this figure with the streamlines of Case 1, shown in Fig. 4.9, one can see that Case 2 did in fact greatly reduce the size of the separation bubble.

Spanwise vorticity plots are shown in Fig. 4.16 for all three meshes. These results have been phase-averaged to show the vortical structures present in the flow solution. The phase shown is for $t/T = 1/12$ which is $1/12^{\text{th}}$ into the jet-cycle or just after the jet first became active. All results show the breakdown of large vortical structures due to the highly unsteady separated zone on the suction surface. The solution for the mid- and fine-meshes compare well with both capturing some of the finer detail of the vortical structures. The coarse-mesh is likely not refined enough as it seems to diffuse the solution resulting in poor resolution of the finer details in the vortical structures. The vortices seem to coalesce into larger vortical structures.

Phase-averaged plots of velocity magnitude profiles normal to the blade surface are shown in Fig. 4.17 and compared with the experimental values of Volino et al. (2011). Each column of this plot represents each of the six streamwise stations from Fig. 4.3 while the rows represent different phases in the jet pulsing cycle. Beginning at the first station, $x/C_x = 0.65$, all numerical results agree well with the results of Volino as here the flow is still attached and well-behaved. At the next station, $x/C_x = 0.72$, the boundary layer is just starting to separate as immediately above the blade surface the velocity normal gradient is very small. The experimental and numerical results are beginning to deviate in phases $t/T = 5/12 \rightarrow 7/12$ where numerical results calculate a slightly higher velocity magnitude just above the boundary layer. Station $x/C_x = 0.80$ begins to show signs of definite separation. Numerical results have slight separation at $t/T = 1/12$ which appears to reattach at $t/T = 2/12$ and 3/12 likely because the jet disturbance has convected downstream by this point in the jet-cycle. The remaining phases of the jet-cycle show the flow relaxing to a slightly separated state again indicating the effects of the VGJ did not persist through the entire jet-

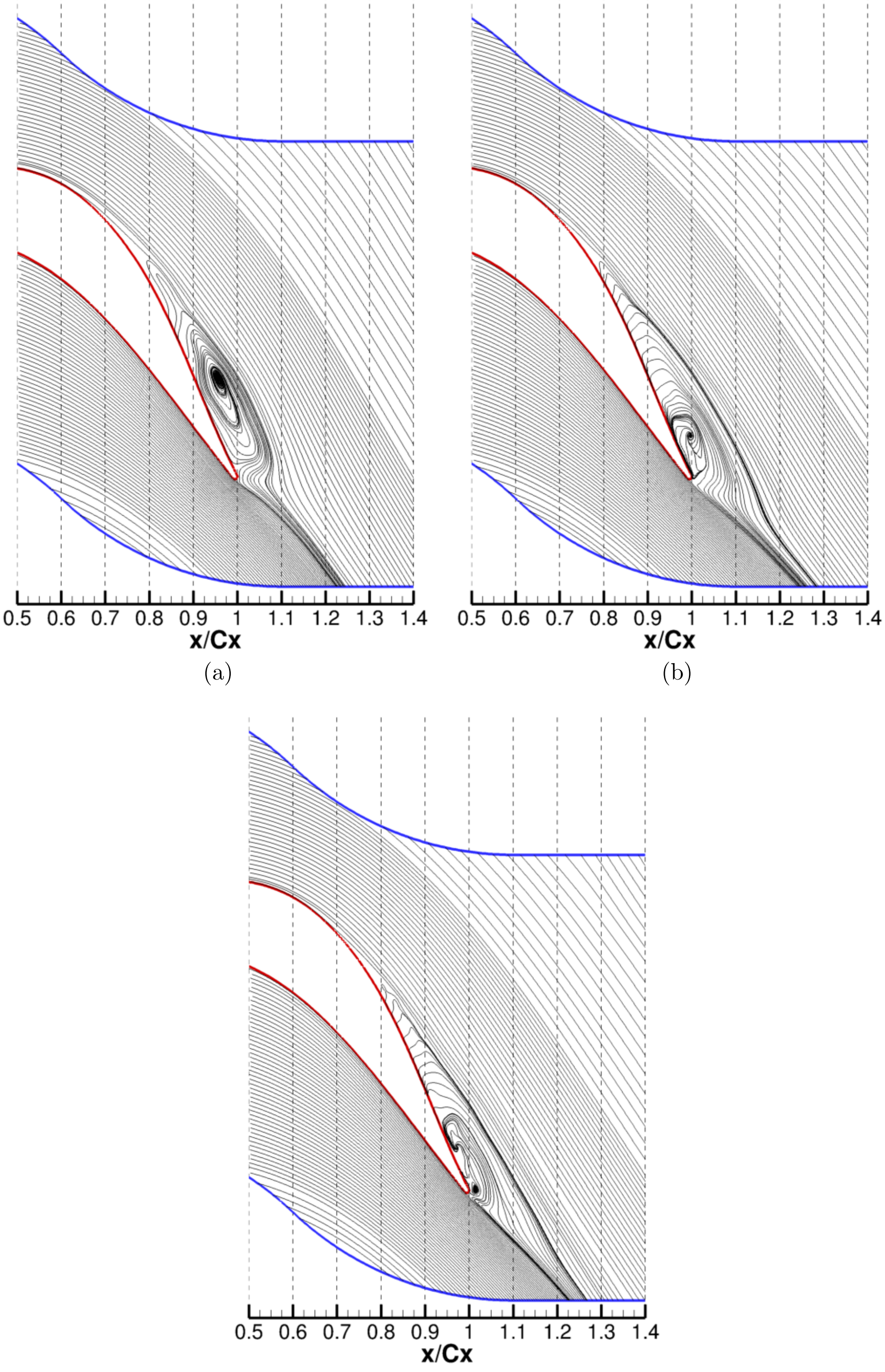

(a)

(b)

(c)

Figure 4.15: Time-averaged streamlines for (a) coarse, (b) mid, and (c) fine meshes, Case 2

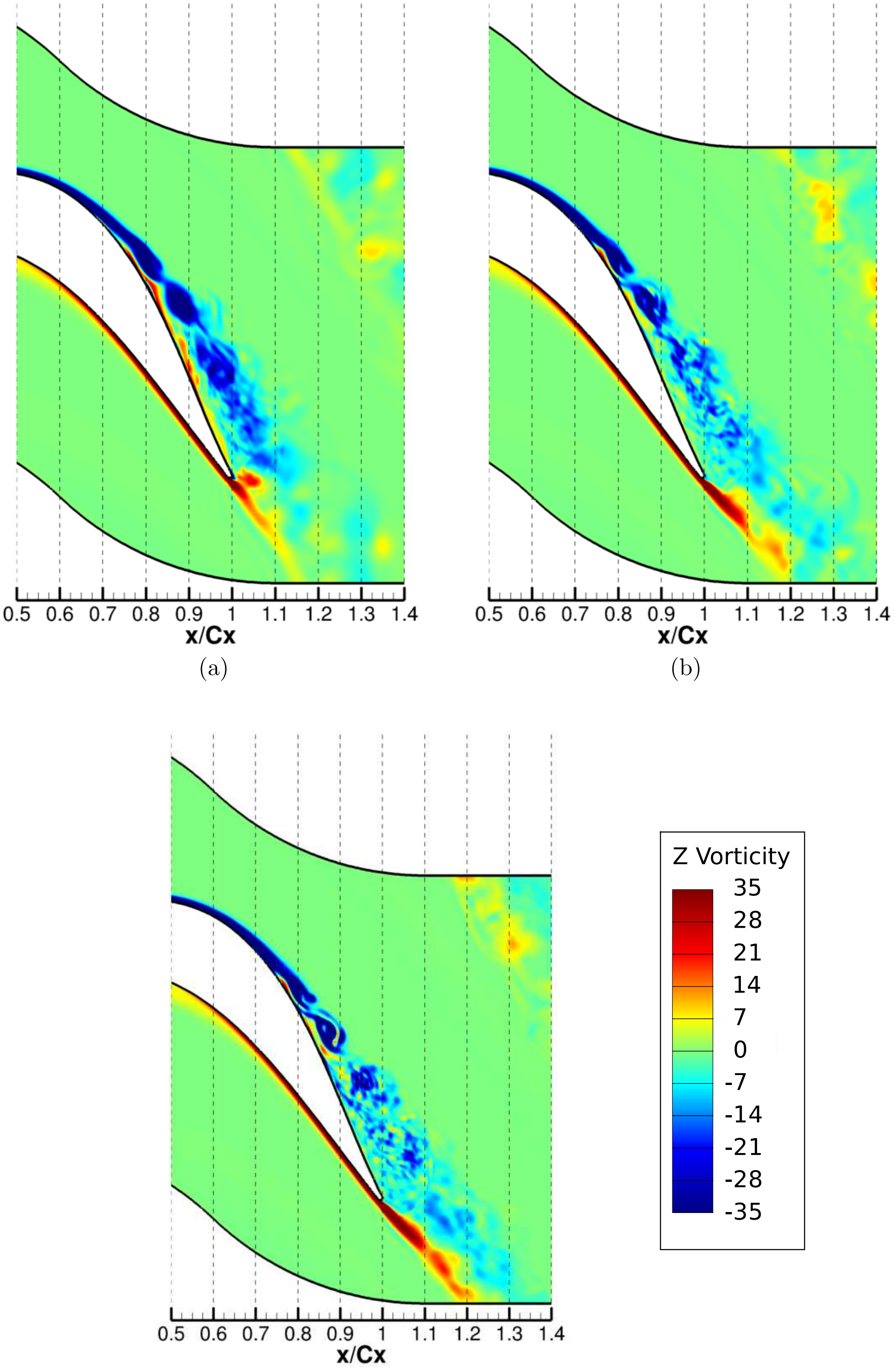

(a)

(b)

(c)

Figure 4.16: Phase-averaged spanwise vorticity for (a) coarse, (b) mid, and (c) fine meshes at phase $t/T = 1/12$, Case 2

cycle. In contrast, the experimental results show attached flow in all but phases $t/T = 10/12 \rightarrow 12/12$. At $x/C_x = 0.86$, the numerical results show separated flow in all phases except for $t/T = 8/12$ and $9/12$ where it looks like the boundary layer is trying to reattach. The experimental results again show attached flow for most of the jet-cycle phases. At the remaining downstream stations, $x/C_x = 0.92$ and 0.97 the numerical results calculate separated flow at all jet phases which contrast with the experimental results that measured attached flow for many of the jet phases. Throughout these results, the mid- and fine-grids results match very well while the coarse-grid results usually calculates a larger degree of separation. Overall, the experimental data shows better VGJ performance and indicates better control of separation than is evident in the numerical results.

In summary, Case 2 represents a case where the experimental studies of Volino et al. (2009, 2011) were able to moderately reduce the degree of separation on the L1A blade. Current computations in this study were able to effectively improve the separation characteristics of the L1A blade but not to the same extent that was measured in the experimental studies. Overall, comparisons with the experimental studies showed that there was a greater degree of separation in the numerical results which can likely be caused by differences in numerical and experimental setups. Specifically, the experimental wind tunnel provided help in turning the flow just after the turbine cascade and included some level of freestream turbulence in both studies. Both of these effects, not accounted for in the simulations, may reduce the amount of separation present on the blade. For most of the results presented here the mid- and fine-level meshes compared very well with each other. In some results the mid- and fine-calculations did not match quantitatively, in areas of high unsteadiness, but still matched in trend. The coarse-mesh differed from the other meshes and did not match as well with experimental measurements. Similar to the results in Case 1 the coarse-mesh calculated a larger degree of separation than the experimental results.

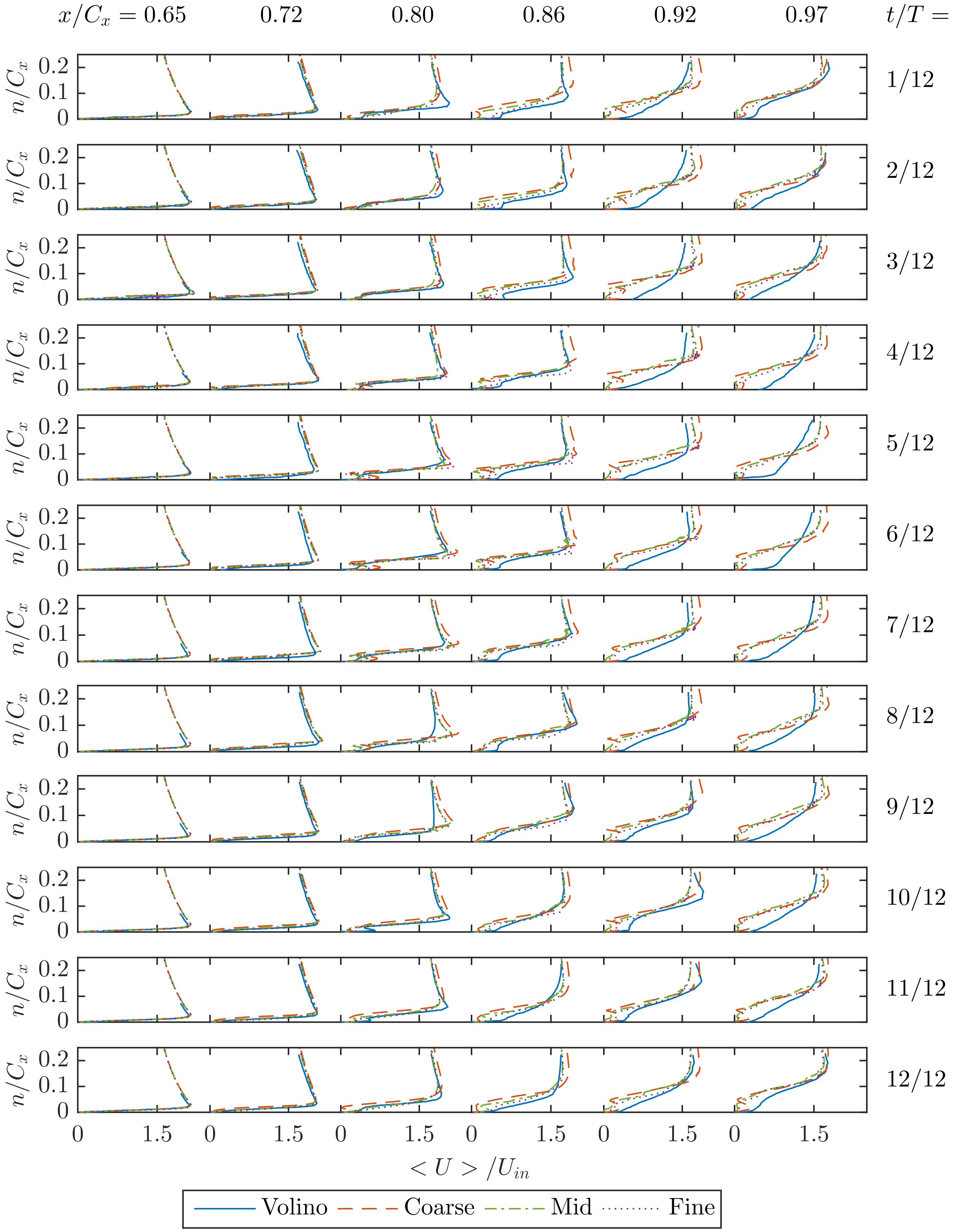

Figure 4.17: Phase-averaged blade normal velocity magnitude profiles at six streamwise stations, Case 2

4.6 Summary

The low-Reynolds number flow for the L1A turbine blade was simulated for three different meshes and compared with the experimental results of Volino et al. (2009) and Volino et al. (2011). These simulations served multiple purposes: learning how to use FDL3DI, numerical validation by comparing with experimental measurements, and verification of adequate grid refinement. Results were generated and analyzed in terms of time-averaged surface coefficient of pressure, blade normal profiles of velocity magnitude and root-mean-square fluctuating velocity magnitude, iso-images of cross-flow vorticity, flow streamlines, and spanwise vorticity. Also, phase-averaged blade normal velocity magnitude profiles were investigated. Two setups were considered from the experimental investigations. These were dubbed "Case 1" and "Case 2" corresponding to contrasting jet efficacy with ineffective separation control and effective control, respectively.

The results of Case 1 calculated a larger amount of separation than was present in the experimental results and included a bias in the data that was also present in the simulations of Volino et al. (2009). The three different mesh sizes also did not agree on the amount of separation seemed to increase with increasing grid refinement. The reason for these changes in the flow solution with grid refinement is probably caused in part due to the large unsteadiness present in the uncontrolled flow case and the potential need for more time-averaging. Results from Case 2 had similar comparisons with experimental data calculating a larger degree of separation. The discrepancies comparing with experimental data can be attributed in part to the differences between the numerical and experimental setups. The current computation makes no effort to simulate the effects of wind tunnel walls or freestream turbulence which are both present in the wind tunnel experiments. Other computations for LPT flows such as those by Rizzetta and Visbal (2005), and Poondru (2007), found similar behavior where experimental results predicted lower amounts of separation. The flow solutions for Case 2 did provide a moderate degree of control over the separation as they did in the experimental study suggesting that the proper flow physics were captured in the VGJs fluid interaction. The comparison of different mesh sizes in Case 2 showed that the mid- and fine-sized meshes compared very well with each other and matched the trends in experimental data. The coarse-mesh did not compare as well with experimental data and differed from the results of the other two meshes and was likely not refined enough for the flow physics in the current problem. By matching the trends in experimental data and providing a moderate degree of control in Case 2, the mid- and fine-sized meshes were considered to provide a flow solution that accurately captured the flow phenomena in the current study. These results provide the means of flow solver validation in this study.

Case 1 did not show good comparisons between the different mesh sizes, but this case also represented a poorly controlled separated flow. Case 2, in contrast, showed good comparisons between the mid- and fine-sized meshes, and additionally, compared well with the trends present in experimental results. Given that the jet configurations of interest are those that control the separation, the similarity of the solutions in Case 2 provide the rationale for using the mid-sized mesh for the remainder of the flow simulations. As stated before, the grid study here is used in order to approximate the meshing requirements for the L2A blade simulations in the next chapter. Given the evidence herein, the mesh for the L2A simulations was constructed in the same manner as that of the 5 million L1A mesh.

Chapter 5

L2A Flow Control Results

The objectives of the current research, discussed in Section 1.5, address the need for research related to controlling separation for LPT blades designed for "high-lift." This chapter presents the results of the current study which simulate various VGJ configurations for the AFRL L2A blade to ascertain optimal jet parameters for mitigating separation. This blade was selected due to its aft-loaded characteristics which provide advantages when considering losses from secondary flows but suffers in mid-span performance which is addressed with VGJ flow control. The choice of an aggressive, aft-loaded design also provides a great test bed for VGJ efficacy as these cases are the hardest to control. These results will add to the literature of flow control for LPT blades and provide a foundation for future research and advancement.

5.1 Numerical Setup

Given the moderate success of the VGJ configuration given in the validation study of Chapter 4, a similar configuration was explored for controlling the separation on the L2A blade. These simulations were conducted at a Reynolds number of $Re_{in} = 10,000$ which provides a large degree of separation and allows for stringent testing of the VGJ efficacy. As in the validation study, a low duty cycle, $DC = 10\%$, was considered.

Other researchers have suggested that low duty cycles are effective because it is the starting and stopping of the VGJ, which provides stronger streamwise vortices than steady blowing, that are responsible for the bulk of separation control (Bons et al., 2002 and Volino et al., 2009).

The jet physical dimensions followed the same work of the validation study, reiterated here for clarity. The jet diameter was set at $0.006C_x$, jet spacing at $0.0636C_x$ (spanwise extent of computational mesh), jet pitch angle at $\theta = 30°$, and jet skew angles at $\phi = 90°$. The flow angles here follow the general recommendation for VGJ efficacy with a shallow pitch angle and large skew angle. The jet location was selected based on the attached coefficient of pressure profile calculated by Lyall et al. (2011). This profile was calculated using Fluent's implementation of the realizable $k - \epsilon$ turbulence model. These calculations were fully turbulent and eliminated all separation on the turbine blade to give the attached coefficient of pressure profile. This profile for the L2A blade can be seen in Fig. 5.1. This plot shows that peak suction occurs at $x/C_x = 0.60$ on the blade (very similar to the L1A) which is generally considered the optimal placement of flow control devices as discussed before. Therefore, this is where the VGJ was implemented in the current study.

The jet configuration discussed thus far was maintained while the jet blowing ratio and frequency were varied to study the effectiveness of the VGJs. The blowing ratio and frequency are generally the largest contributing factors to the effectiveness of the VGJs given the same flow angles and jet location. For this study a range of blowing ratios and frequencies were selected based on the work of Volino et al. (2009, 2011). In their research, these authors varied both the blowing ratio and frequency of the jet finding configurations which were not effective and others that were successful but excessive. The present study uses these results as the basis for selecting jet parameters in the hope that some of these conditions would also provide successful control on the L2A blade given some of its similarities to the L1A blade. Following, in Table 5.1

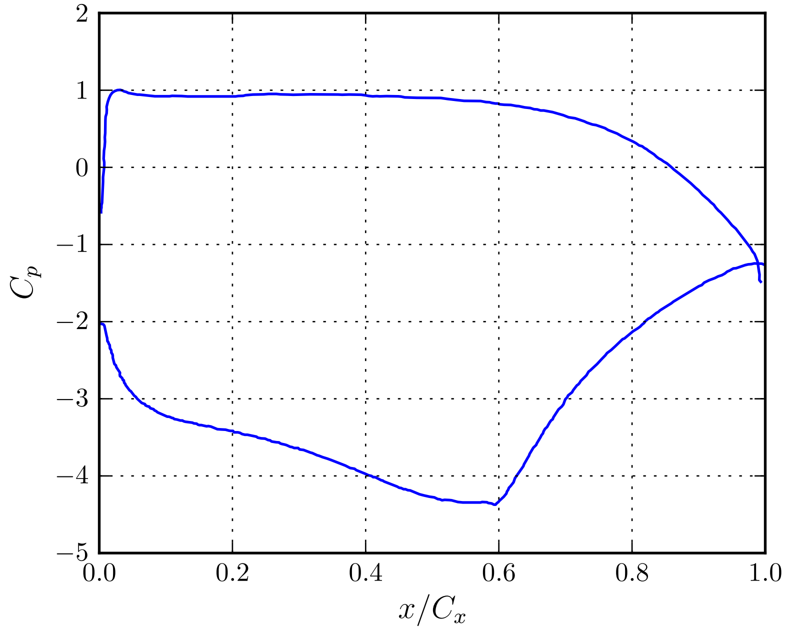

Figure 5.1: C_p profile for L2A from study of Lyall et al. (2011)

is a test matrix of various configurations ranging from Case 1 being predicted as the least effective jet compared with Case 12 likely being the most effective. These jet parameters follow the non-dimensional frequencies presented in the study of Volino. Table 5.2 shows the corresponding frequencies based on the inlet velocity and axial chord length. Additionally, the jet-cycle time is included. To calculate the required information for converting frequency from F_{ssj}^{+} to F^{+} the attached profile of Lyall et al. (2011), shown in Fig. 5.1, was used and followed the same method described in Section 4.2.

Table 5.1: Test matrix of current numerical study

BR/F_{ssj}^{+}	0.28	0.56	1.12
0.5	Case 1	Case 5	Case 9
1.0	“ 2	“ 6	“ 10
2.0	“ 3	“ 7	“ 11
3.0	“ 4	“ 8	“ 12

In order to measure the effectiveness of the VGJs, a baseline solution was also

Table 5.2: Jet frequency based on inlet conditions and axial chord along with jet-cycle time for L2A flow simulations

Cases	F^{+}_{ssj}	F^{+}	t_{jet}
Cases 1-4	0.28	0.756	2.184
Cases 5-8	0.56	1.512	1.092
Cases 9-12	1.12	3.02	0.546

generated for the same Reynolds number ($Re_{in} = 10,000$). The baseline mesh did not include boundary conditions for VGJ implementation, and the spanwise extent of the computational domain was set at $0.2C_x$. The justification for this spanwise extent was discussed previously in Section 3.4 on page 51. The baseline case was simulated with a time step of $\Delta t = 5.0e^{-4}$. The transient run was executed for 32.16-time units. Data collection was then executed for 14.0-time units during which time averaging commenced. An additional 10.5-time units were simulated in which time averaging continued and time histories of fluctuating velocity was collected for turbulence frequency spectra calculations.

Given the jet-cycle time for the flow control simulations, as shown in Table 5.2, the time step of the simulations could be selected. The time step was selected in order to give an integer number of solver iterations in one jet-cycle. Given in Table 5.3 are all the timing parameters for each case simulated. This includes the simulation time step (Δt), number of steps per jet-cycle, jet-cycle and total time of each transient run, jet-cycle and total time for time-averaging, and finally jet-cycle and total time for collection of turbulence statistics. The time step is different for Cases 9-12 to accommodate phase averaging for the cases with higher jet frequency.

Table 5.3: Simulation execution length for L2A cases

	Δt	VGJ $^{\text{steps}}/_{\text{jetcycle}}$	Transient Run $^{\text{jetcycles}}/_{\tau}$	Time-Average $^{\text{jetcycles}}/_{\tau}$	Turbulence Statistics $^{\text{jetcycles}}/_{\tau}$
Cases 1-4	$6.546e^{-4}$	3,336	3 / 6.553	10 / 21.843	7 / 15.290
Cases 5-8	$6.546e^{-4}$	1,668	5 / 5.461	15 / 16.382	12 / 13.106
Cases 9-12	$6.501e^{-4}$	840	10 / 5.461	27 / 14.744	24 / 13.106

5.2 Meshing Details

Given the results of the mesh study that was conducted in Chapter 4 on page 61 a similar 5 million grid point mesh was created for the L2A in the same method as that used for the L1A blade. A background H-grid was used for computing flow through the cascade channel and details around the blade were captured with a highly refined O-grid. The meshes for the flow control and baseline cases were different due to the additional spanwise extent present in the baseline case. To maintain the spanwise mesh spacing of $\Delta z \approx 0.004$ additional grid points were needed in the H-grid for the baseline case. The baseline H-grid consisted of 267 x 130 x 48 points in the streamwise, cross-flow, and spanwise directions, respectively. The corresponding baseline O-grid had 661 x 104 x 48 points. Points were clustered in the streamwise direction on the aft section of the suction surface to accurately capture the fluid interactions of the separation bubble present there. This resulted in 38.3% of all O-grid points contained in the aft portion of the blade. Points were also clustered in both the streamwise and spanwise directions around the point of peak suction to help capture the pertinent flow physics there (where the VGJ is located in flow control cases). The first grid point at the wall was set at $\Delta n = 0.00035$.

The flow control mesh for the L2A contained fewer points in the spanwise direction for the background H-grid due to the shorter spanwise extent which was sized to the jet spacing used in Volino et al. (2009) and Volino et al. (2011). The flow control H-grid consisted of 366 x 201 x 17 points in the streamwise, cross-flow, and spanwise directions, respectively. The flow control O-grid had 649 x 105 x 55 points. Points were clustered in the streamwise and spanwise directions surrounding the VGJ hole with 13 points across the jet diameter. The first grid point at the wall was set at $\Delta n = 0.00035$. A screenshot of the aft end of the blade is shown in Fig. 5.2 and shows the clustering of points near the VGJ location and in the aft section of the blade. The aft section contains 37.6% of all the points for the O-grid topology mesh.

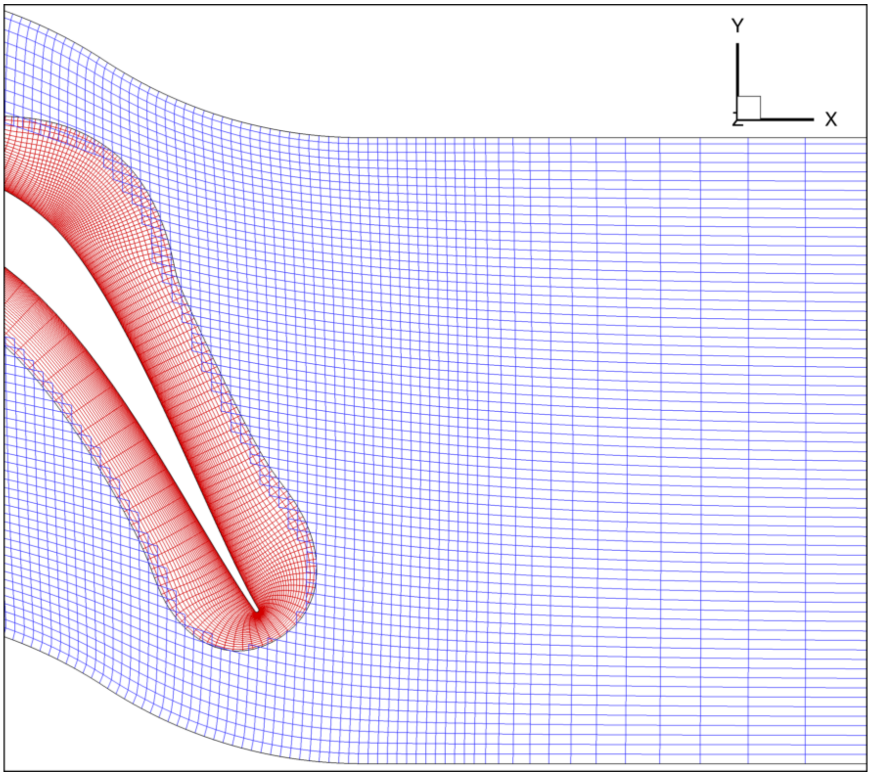

Figure 5.2: Screenshot of H-O mesh setup for flow control L2A mesh (aft end of blade, every 3rd grid point shown)

Mesh resolution given in wall units is shown in Table 5.4 for the baseline and flow control cases. The flow control values refer to the maximum Δt^+ for all 12 simulations and the corresponding minimum and maximum values for all 12 simulations for each of the Δs^+, Δn^+, and Δz^+values. Wall reference conditions used for normalizing these values were obtained from the time-averaged solution at $0.5C_x$ on the blade suction surface where the boundary layer is fully developed, attached, and steady. The mesh sizes Δs^+, Δn^+, and Δz^+ are for the streamwise, normal, and spanwise directions, respectively.

Table 5.4: Computational mesh size given in wall units for baseline and flow control cases

Case	Δt^+	Δs^+_{min}	Δs^+_{max}	Δn^+_{min}	Δn^+_{max}	Δz^+_{min}	Δz^+_{max}
Baseline	0.019	0.399	11.704	0.253	0.291	3.399	3.399
Flow Control	0.031	0.357	13.223	0.226	0.320	0.357	2.517

5.3 Reynolds Number Iterations

Reynolds number iterations were conducted with a coarse baseline mesh which allowed for quickly iterating through various values of Re_∞. The corresponding values can be seen in Table 5.5. The value of U_{in} given here was required to calculate the jet frequency thus allowing for the simulations time-step to be selected. The values of Re_{in} will vary slightly between different simulations but there was no effort to correct these variations. Specifically, during separation mitigation, the value of Re_{in} will increase due to reduced blockage in the cascade.

Table 5.5: Re_∞ iteration results for $Re_{in} = 10,000$

Re_∞	Re_{in}	U_{in}
16,600	10,074	0.6055247

5.4 Results

The following sections present computational results for the twelve jet configurations discussed above. The results of these simulations are compared with the baseline case to show potential improvement in separation control. Results are presented as time-averaged surface pressure distributions, wake loss profiles, blade normal velocity magnitude, blade normal tangent velocity, blade normal fluctuating velocity magnitude, and turbulent kinetic energy frequency spectra. Figure 5.3a shows a diagram of the locations where blade normal profiles were collected. Figure 5.3b shows the locations where time histories of fluctuating velocity were recorded for turbulence frequency spectra. Each of these points was located at a distance $0.005C_x$ normal to the blade surface. For the baseline case, turbulent frequency spectra were spanwise-averaged. All data presented for flow control cases is from points located in-between jets on the periodic spanwise domain boundaries unless otherwise stated. Legends for many of the results use a capital “B” to represent the various blowing ratios in the flow simulations.

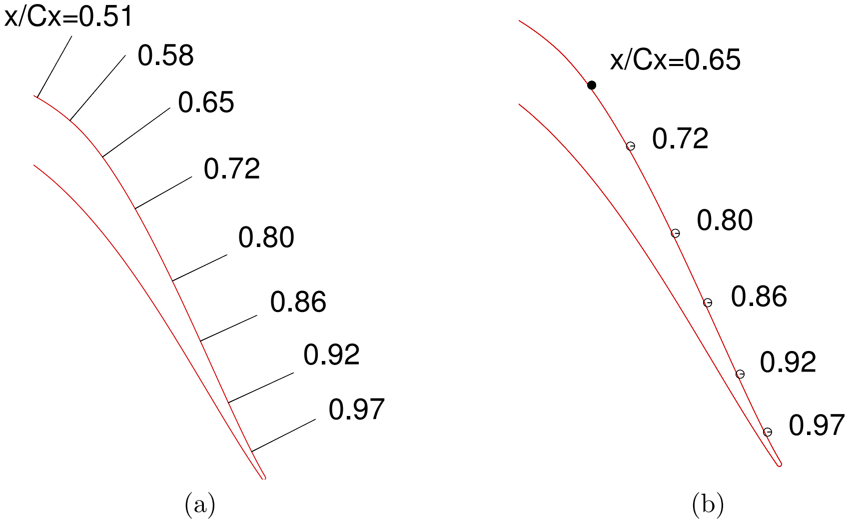

Figure 5.3: (a) Blade normal profile data collection locations, and (b) locations of fluctuating velocity time history data collection

5.4.1 Coefficient of Pressure

The simulation results for coefficient of pressure are shown in Figs. 5.4, 5.5, and 5.6. Each of these figures compares the flow control results of Cases 1-4, 5-8, and 9-12, respectively, to results of the single baseline case. Coefficient of pressure is defined by the following equation:

$$C_p = \frac{p_{t,in} - p}{\frac{1}{2}\rho_{in} U_{in}^2} \tag{5.1}$$

where all variables with the subscript “*in*” are conditions at the inlet while p is specified on the blade surface.

The results herein show very little change in pressure distribution for all flow control cases. In general, it seems that the flow control methods implemented in this study did little to effect the separation on the L2A blade. All plots show the plateau that is inherent in separated flow, but none of the cases show definite reattachment. Case 4 ($BR = 3.0,\ F^{+} = 0.756$) shows a slight peak in coefficient of pressure at $x/C_x = 0.86$ after which there is a gradual decrease in coefficient of pressure. This could indicate a small degree of separation relief. For all cases at both of the lower jet frequencies ($F^{+} = 0.756,\ 1.512$) the pressure surface results differ slightly from the baseline case with the flow control cases providing a slight increase in pressure. The results on the pressure surface were not expected to change much due to its isolation from the effects of the separation on the suction surface. For the two lower frequencies and the two higher blowing ratios ($BR = 2.0,\ 3.0$) the results near the trailing edge start deviating from the baseline case around $x/C_x = 0.8$. For the two lower blowing ratios, deviation from the baseline case does not occur until further down the blade. This could indicate that the stronger blowing ratios are starting to affect the separated flow further upstream. The flow control cases at the highest frequency ($F^{+} = 3.02$) were predicted to be the most effective but these results largely match the baseline results indicating they are probably the least effective.

An important result to note is the location of peak suction, and probable separation which are both consistent in all flow simulations. Peak suction in these results occurs at $x/C_x = 0.43$ and the plateau in C_p starts at $x/C_x = 0.6$. This shows that the flow is separated by $x/C_x = 0.6$ and separation likely began before reaching the beginning of this plateau. The attached C_p results that were used for the placement of the jets, shown in Fig. 5.1, predicted a peak suction at $x/C_x = 0.6$. This location was chosen because it is often the optimal position for flow control jets, but in the current simulations, the flow appears separated at this same point. This means that the jets were likely placed downstream of the separation point which will reduce the effectiveness of the jets. This causes poor jet performance because it is unable to incorporate freestream momentum into the boundary layer prior to separation.

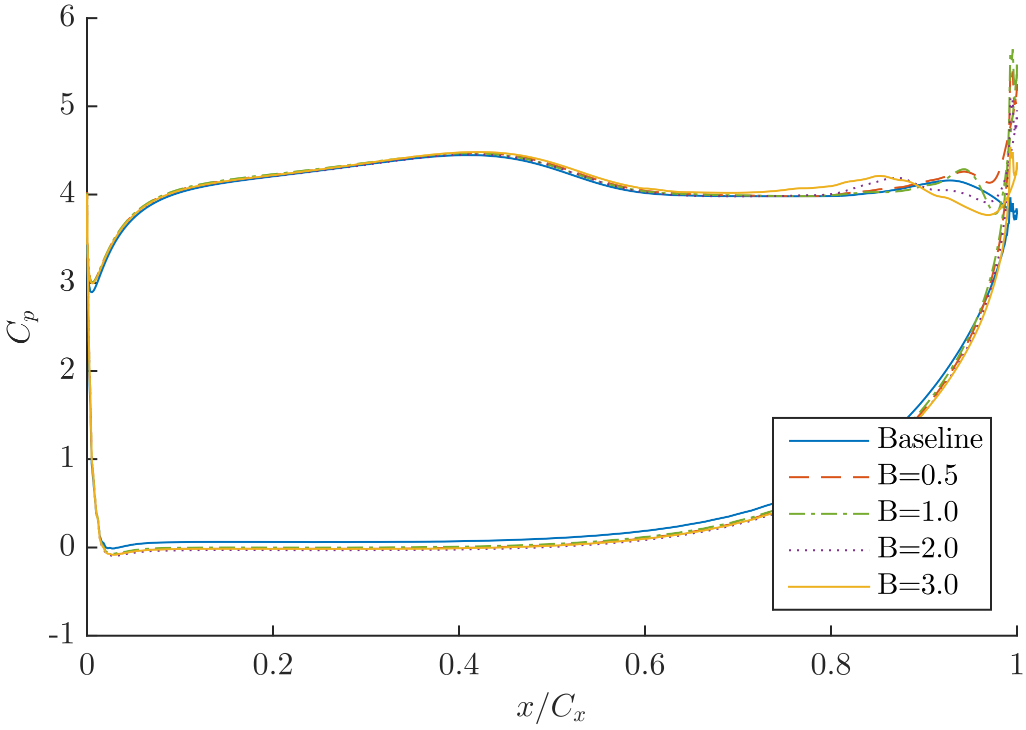

Figure 5.4: C_p surface distribution for Cases 1-4 ($F^+ = 0.756$)

5.4.2 Wake Loss

Results for the time-averaged wake loss coefficient, defined in Eq. 4.5, are shown in Figs. 5.7, 5.8, and 5.9. These results were extracted from the pitch axis of the turbine cascade just after the blade trailing edge at $x/C_x = 1.05$. Negative values of y/C_x are toward the pressure side of the blade with increasing values moving toward the suction side. Looking at all results in general, the flow control cases create a more narrow wake loss region, compared to the baseline, which indicates a reduction in the size of the separation bubble, but flow control also seems to cause two large loss cores in the separated flow region. These loss cores could be attributed to increased mixing which occurs with the jets, increasing viscous losses. Coupling this increase

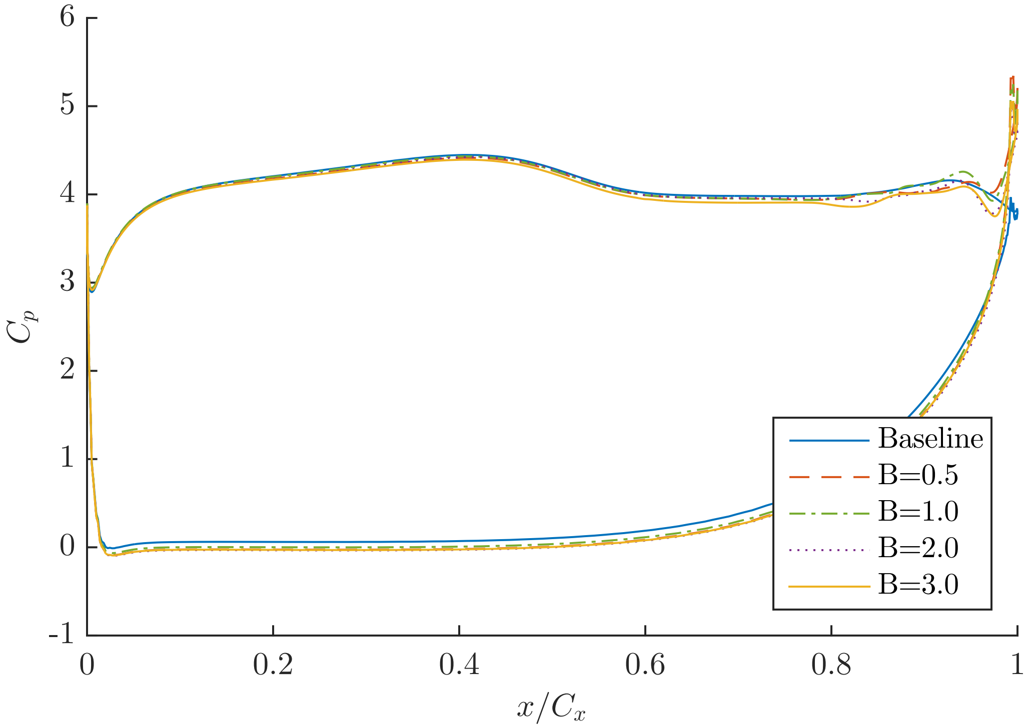

Figure 5.5: C_p surface distribution for Cases 5-8 ($F^+ = 1.512$)

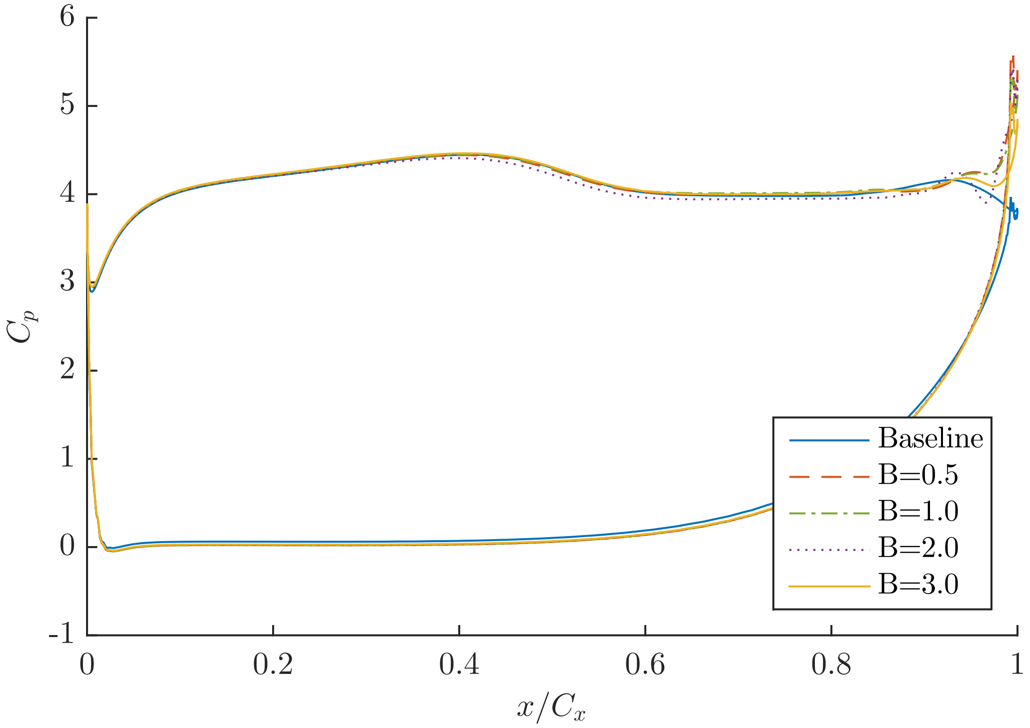

Figure 5.6: C_p surface distribution for Cases 9-12 ($F^+ = 3.02$)

in frictional losses with the failure to substantially reduce separation causes the jets to produce larger peaks in the wake loss when compared with the baseline flow. As with the results of coefficient of pressure, discussed in 5.4.1, the pressure side of the turbine blade shows different behavior in the baseline and flow control cases.

The case which seems to improve the wake loss the most is Case 4, the same case which provided slight separation relief discussed in Section 5.4.1. This case occurred at the lowest jet frequency simulated and the highest blowing ratio ($BR = 3.0,\ F^+ = 0.756$). The results for Case 4 show a narrowing of the wake loss profile with one peak of the loss core being greater than the baseline case, but the other loss core having a value very similar to the baseline case. As the jet frequency increased, the wake loss profile core becomes wider and more closely approximates the suction surface behavior of the baseline case. The highest jet frequency simulated again seems to perform the most poorly with the wake loss toward the suction surface of the blade almost identical to the baseline case.

Integrated wake loss is obtained by integrating the wake loss values over the cross-flow spacing between the blades. This is defined mathematically as:

$$\psi_{int} = \int_y \left(\frac{p_t - p_{t,e}}{p_t - p} \right) dy \tag{5.2}$$

Figure 5.10 compares the integrated wake loss for all 12 flow control simulations. Each of the integrated wake loss values is normalized by the integrated wake loss value calculated for the baseline case. Consistent with the results discussed so far, the highest frequency jet simulations performed the worst with every case actually calculating an integrated wake loss value that was higher than the baseline case. The lowest frequency jets performed the best with most values showing improvement over the wake loss profile of the baseline case. Case 4 exhibited the beginnings of flow transition in the coefficient of pressure results and provided a narrower wake loss

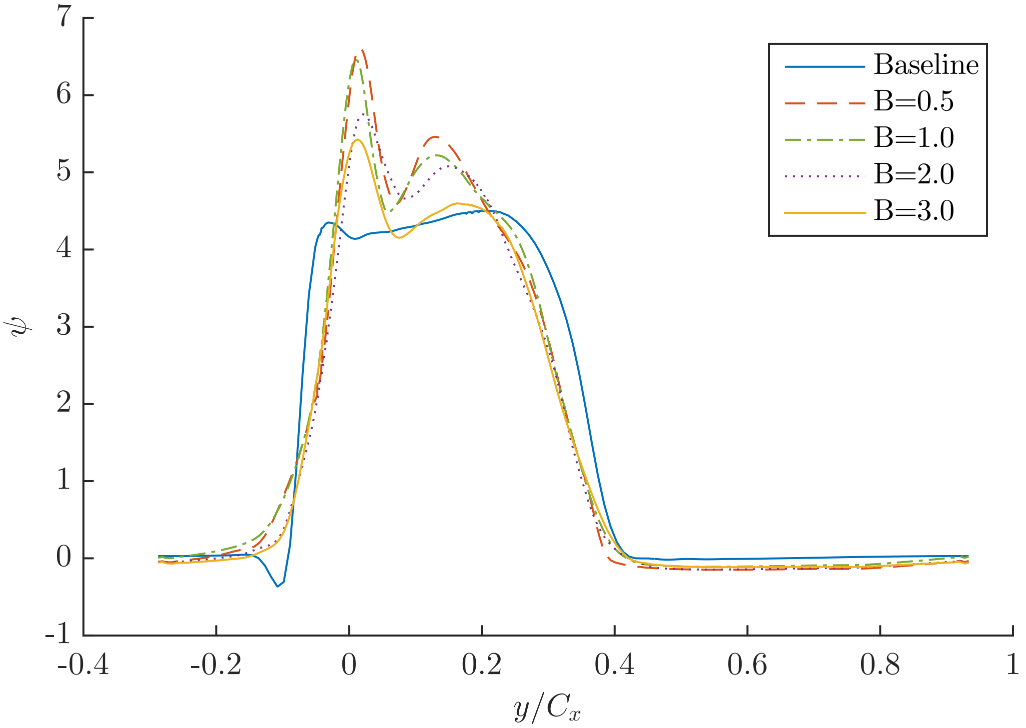

Figure 5.7: Wake loss coefficient at $x/C_x = 1.05$ for Cases 1-4 ($F^+ = 0.756$)

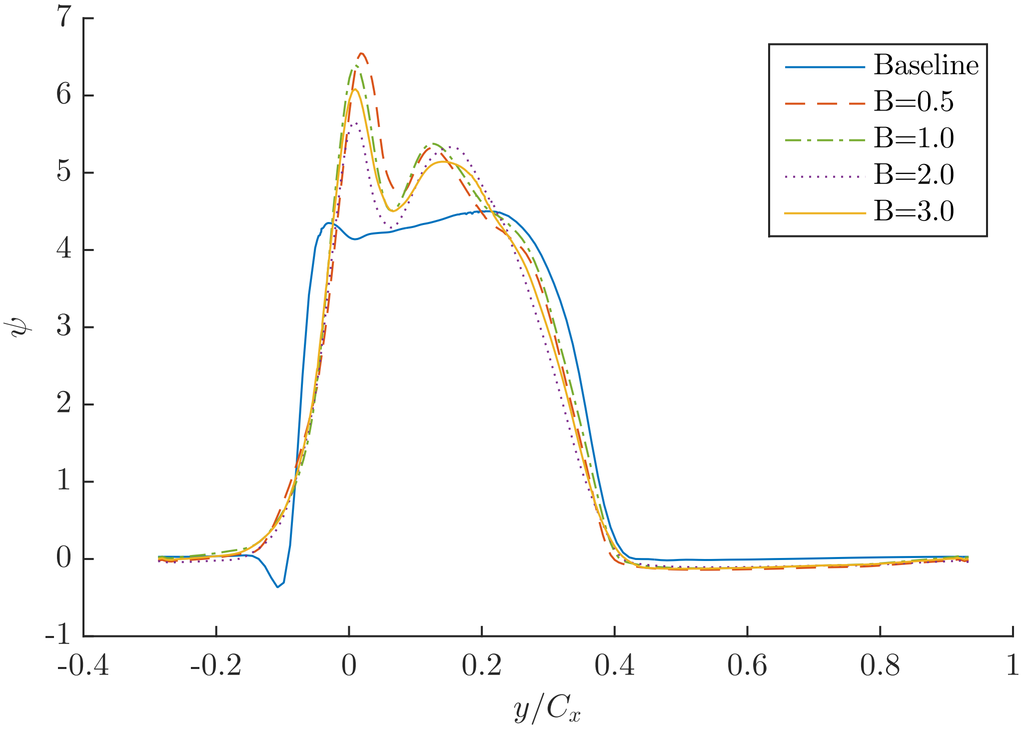

Figure 5.8: Wake loss coefficient at $x/C_x = 1.05$ for Cases 5-8 ($F^+ = 1.512$)

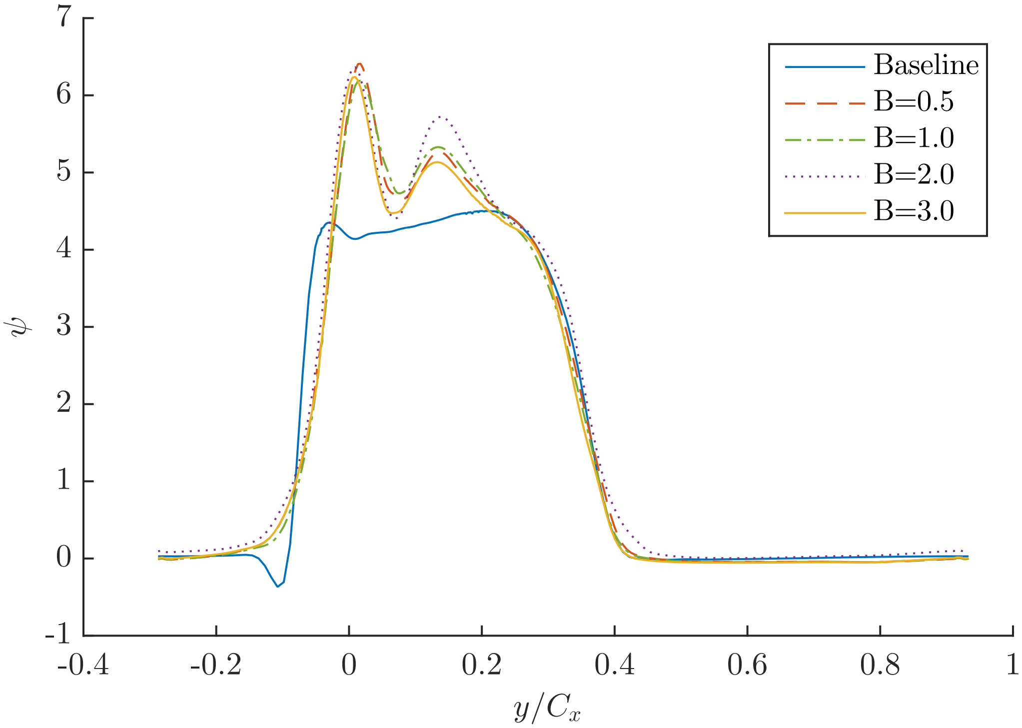

Figure 5.9: Wake loss coefficient at $x/C_x = 1.05$ for Cases 9-12 ($F^+ = 3.02$)

profile. The integrated wake loss results for Case 4 also show the largest improvement over the baseline case.

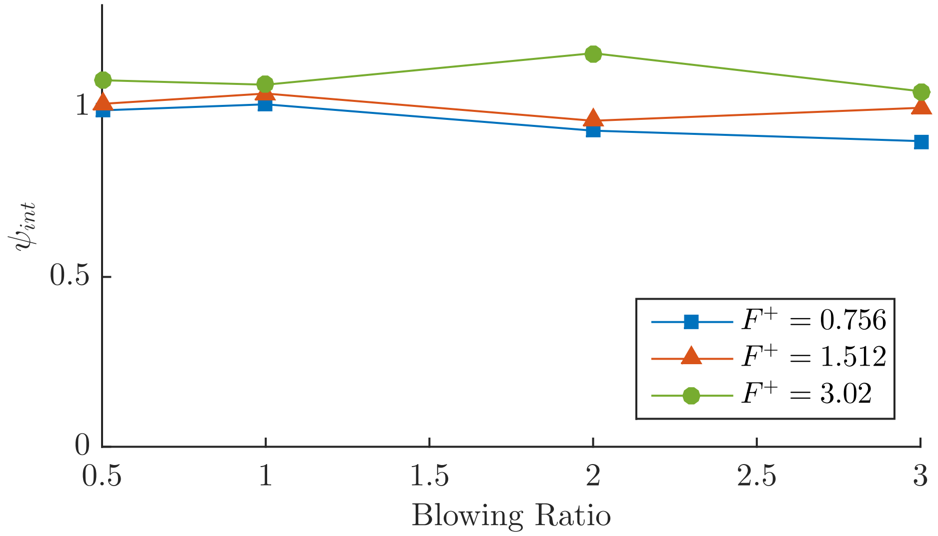

Figure 5.10: Integrated wake loss normalized by baseline integrated wake loss

5.4.3 Blade Normal Velocity Magnitude

Time-averaged velocity magnitude profiles normal to the blade surface are shown in Figs. 5.11, 5.12, and 5.13. The x-axis is shifted for each of the blade normal profiles for display clarity. Results are displayed at the eight streamwise stations as shown in Fig. 5.3a.

The lowest jet frequency simulations, shown in Fig. 5.11, show the flow control simulations essentially identical to the baseline case at the first two streamwise stations, $x/C_x = 0.51,\ 0.58$. The first station shows that the boundary layer is still attached but this second station indicates that flow separation has begun, as indicated by the zero normal velocity gradient at the wall. This result confirms the suspicions outlined in the discussion of the coefficient of pressure results in Section 5.4.1. Separation occurs upstream of the VGJ placement, placed at $x/C_x = 0.60$, which reduces the effectiveness of the jets. Each streamwise location downstream of the jet shows the baseline case calculating a larger separation bubble with the disparity in size increasing when moving downstream. This indicates that the jets did have an effect on reducing the size of the separation bubble but the effect was very modest. As with the results discussed thus far, Case 4 seemed to provide a greater degree of separation control with a smaller separation bubble at both $x/C_x = 0.80$ and 0.86. The velocity profile close to the blade also suggests that Case 4 contains a region of reverse flow due to the non-zero normal velocity gradient there. This would be consistent with the beginnings of transition which would occur in the vicinity of the reverse flow vortex present in the separation bubble (refer to Fig. 1.1). Other stations downstream of this showed very similar behavior between each of the four cases but all still showed improved behavior over the baseline case.

The next jet frequency ($F^+ = 1.512$) simulations, shown in Fig. 5.12, also show identical behavior between flow control and baseline cases at the first two streamwise stations, but additionally, the third station has near identical behavior. As with the

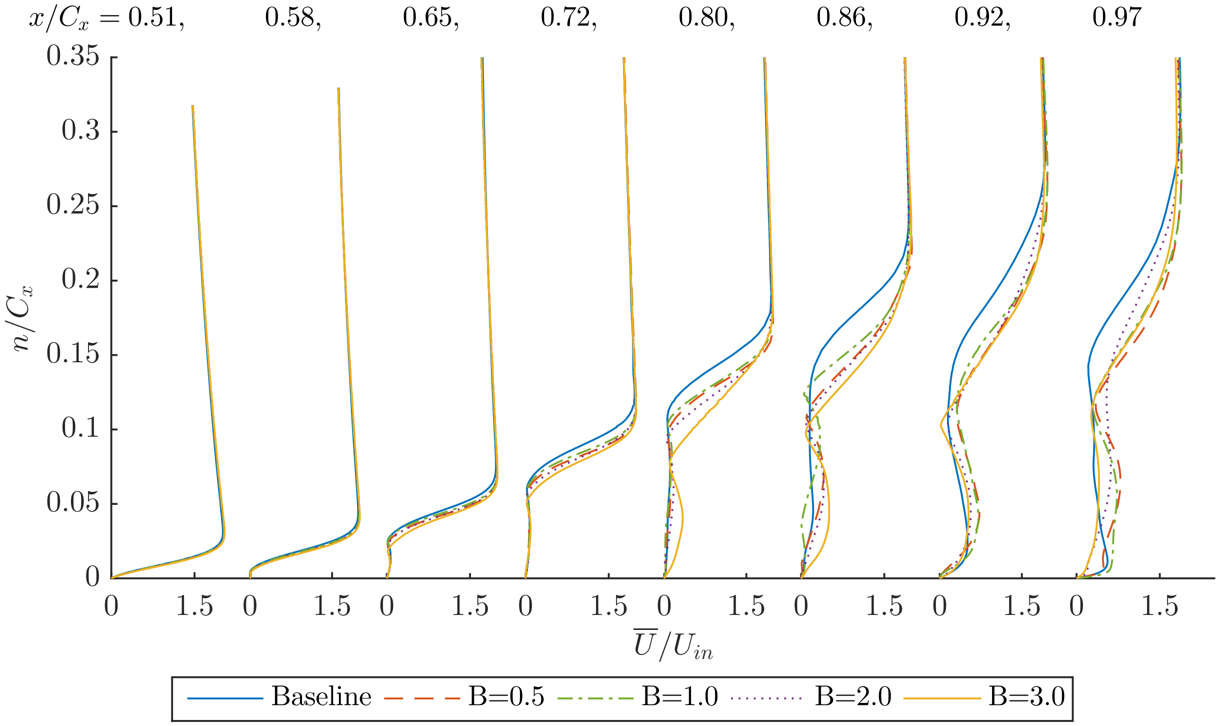

Figure 5.11: Time-averaged blade normal velocity magnitude profiles at eight streamwise stations, Cases 1-4 ($F^+ = 0.756$)

simulations of the lowest jet frequency, the flow is still attached at the first streamwise station but has separated by the second station. Flow control simulations exhibit a similar behavior to the lowest frequency simulations when comparing to the baseline case. After the third station each subsequent downstream station, the separation bubble in the flow control case is reduced in size by a modest amount. This effect is not as pronounced as it was in the lowest frequency case. Each of the four flow control cases portrays similar velocity profiles with slight differences starting at $x/C_x = 0.86$, most likely attributed to the massive separation occurring by this point. The two largest blowing ratio cases match more closely at $x/C_x = 0.80$ prior to the massive separation and unsteadiness downstream.

The highest jet frequency simulations, shown in Fig. 5.13, differ from the other eight simulations displaying almost identical behavior between the flow control simulations and the baseline case at the first five streamwise stations. This fact further

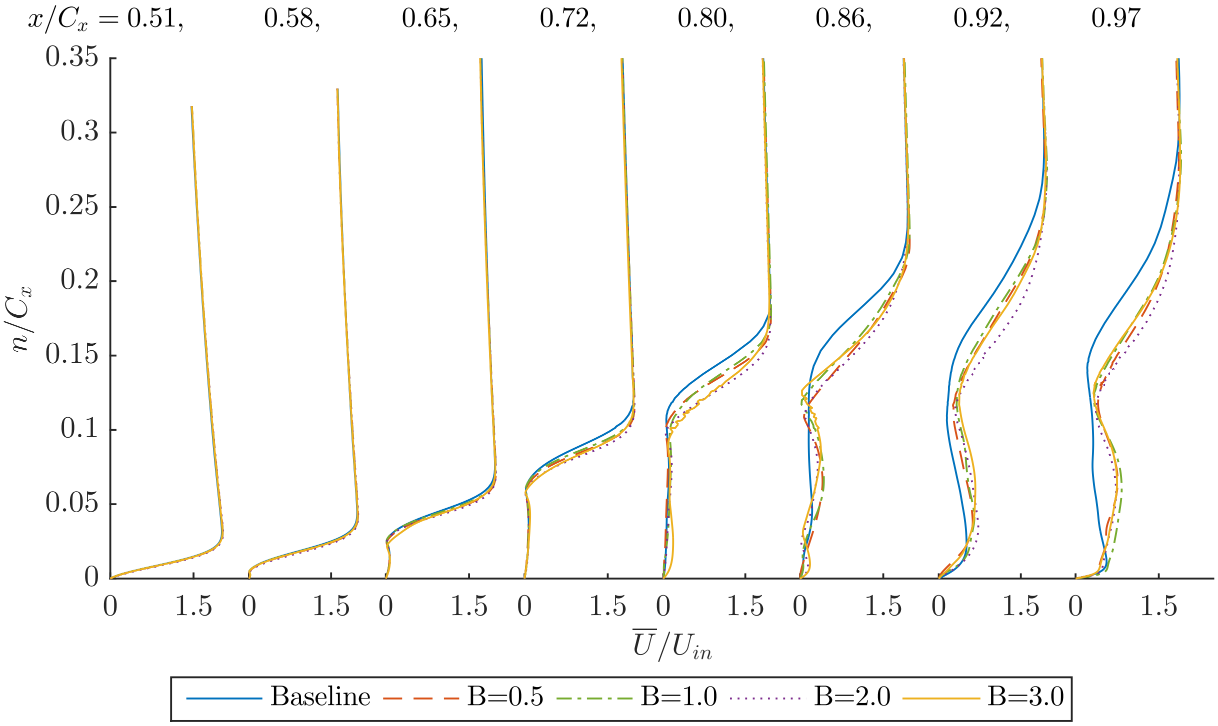

Figure 5.12: Time-averaged blade normal velocity magnitude profiles at eight streamwise stations, Cases 5-8 ($F^+ = 1.512$)

reinforces the evidence in other results discussed so far that the highest jet frequency cases conferred the poorest separation mitigation. At the last three streamwise stations the flow control cases offer a slight decrease in the size of the separation bubble, but this is much more modest than the reduction present in the two lower jet frequency simulations.

In all cases, the flow control results have similar profiles until the downstream station at $x/C_x = 0.86$ at which point the cases contain larger differences. The last three streamwise stations are likely contained in the massive separation region and contain high levels of unsteadiness causing the differences between each of the cases.

5.4.4 Blade Normal Tangent Velocity

In order to offer an alternative perspective of the velocity profiles near the blade Figs. 5.14, 5.15, and 5.16 show tangential velocity profiles. These profiles are for the

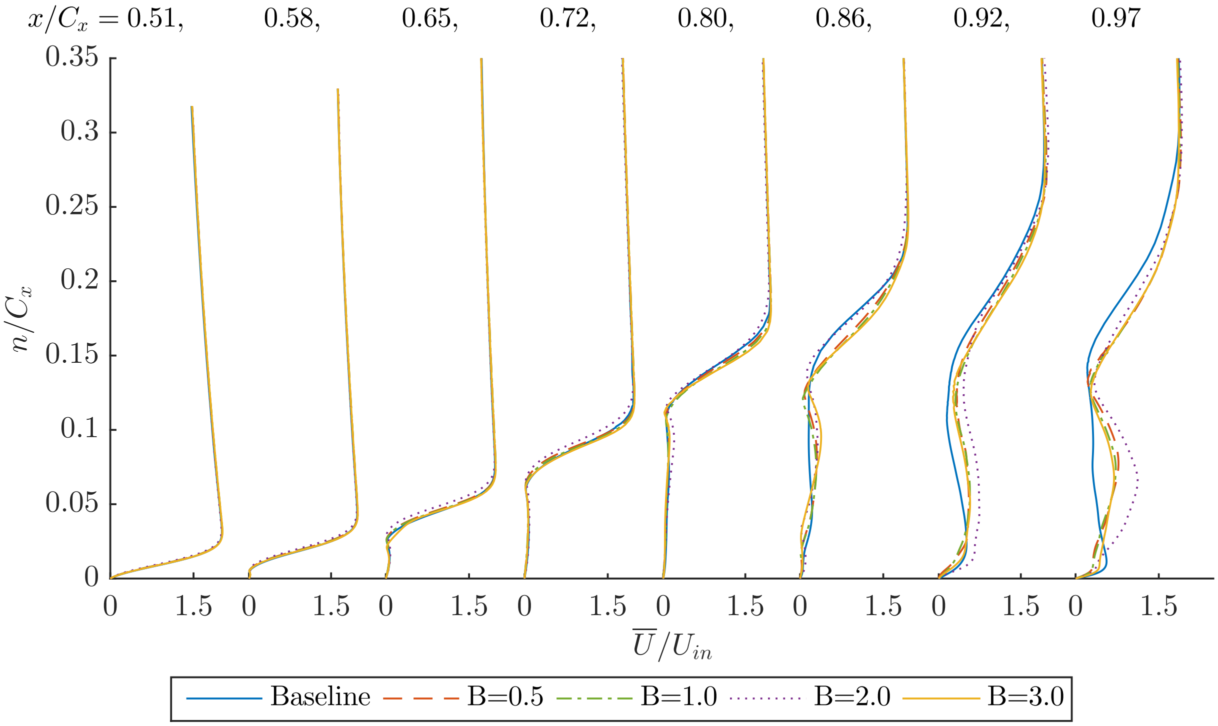

Figure 5.13: Time-averaged blade normal velocity magnitude profiles at eight streamwise stations, Cases 9-12 ($F^+ = 3.02$)

component of velocity tangential to the blade at the respective streamwise stations and allows the visualization of reverse flow in the separated flow region. The x-axis is shifted for display clarity and results are displayed at each streamwise station as shown in Fig. 5.3a.

The lowest frequency simulation, shown in Fig. 5.14, shows near identical behavior when compared with the blade normal velocity magnitude profiles, shown in Fig. 5.11. This similarity starts to break down at $x/C_x = 0.80$ where the highest blowing ratio case, Case 4, begins displaying a reverse flow region. Prior to this location the separation was characterized by a “dead-air” region as noted in Fig. 1.1. Case 4 containing a reverse flow region further upstream than the other simulations could indicate a larger reverse flow vortex, or that Case 4 has a separated region with a smaller streamwise extent than the other cases, thus pushing the reverse flow vortex further upstream. The latter case is more likely given that Case 4 starts approaching freestream velocity values further upstream and closer to the blade than the other cases. By the last station, the two highest blowing ratios have small reverse flow regions, especially near the blade when compared to the other cases. This indicates that none of the cases reattach before the end of the blade, but the two highest blowing ratios are probably close to reattachment near the blade trailing edge. Also, of note is the similarity between the flow control simulations at the last three streamwise stations in contrast to the results for the velocity magnitude. This indicates that there is unsteadiness in the spanwise direction which is not accounted for in calculating the tangent velocity.

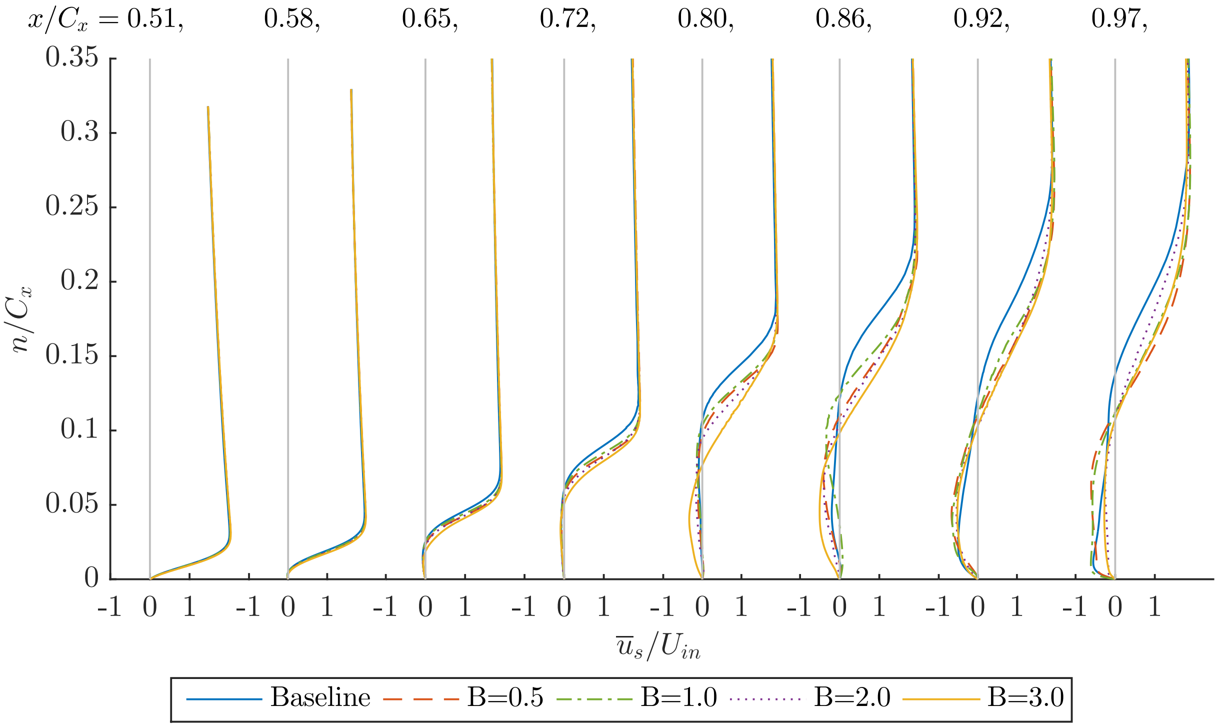

Figure 5.14: Time-averaged blade normal, tangent velocity profiles at eight streamwise stations, Cases 1-4 ($F^+ = 0.756$)

The mid-frequency simulation is shown in Fig. 5.15. As with the lowest frequency cases the results largely match the blade normal velocity magnitude profiles until $x/C_x = 0.86$. After this point, each simulation contains a modest amount of reverse flow. Each flow control simulation is very similar in terms of the tangent velocity profile. By the last station, none of the simulations are indicating a reduction in the size of the reverse flow region in contrast to the lowest frequency cases which showed results indicating incipient reattachment.

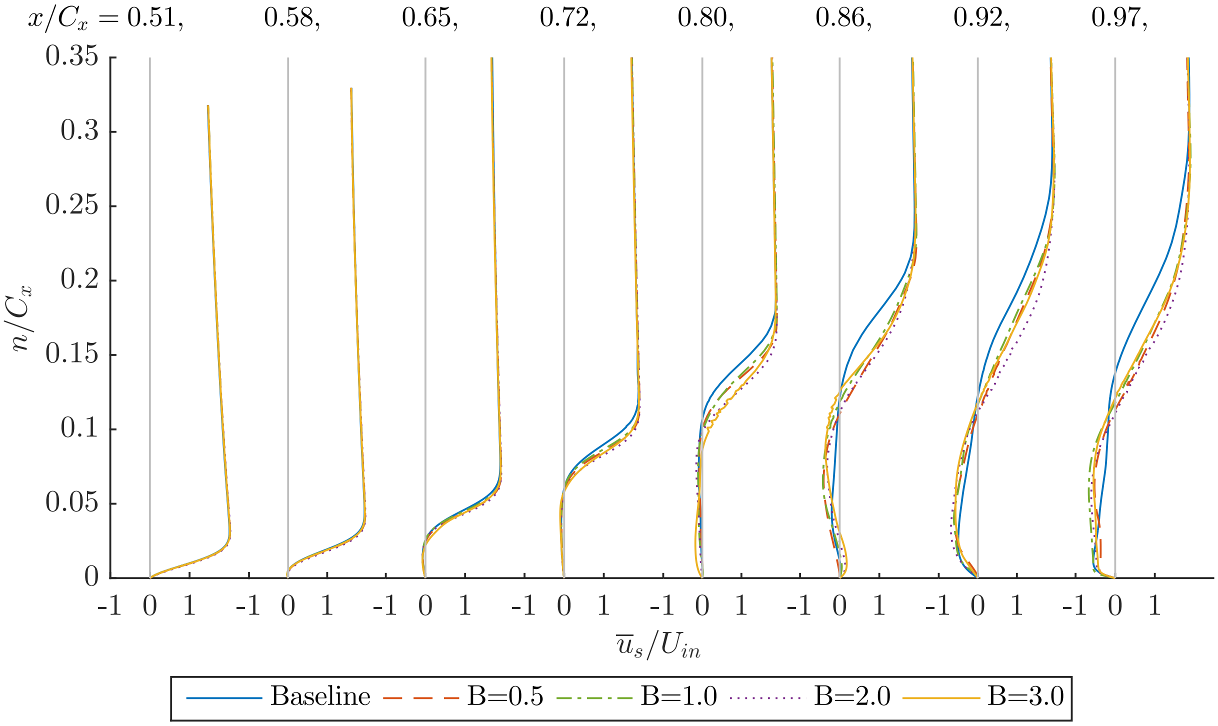

Figure 5.15: Time-averaged blade normal, tangent velocity profiles at eight streamwise stations, Cases 5-8 ($F^+ = 1.512$)

The highest frequency simulations are shown in Fig. 5.16. The results here indicate very similar behavior between the flow control and baseline cases at all except the last streamwise station. At the last station, the flow control cases indicate a larger degree of reverse flow. Although the flow control cases indicate larger reverse flow regions they also approach freestream velocity closer to the blade than the baseline case does, thus indicating a smaller separation zone.

5.4.5 Blade Normal RMS Fluctuating Velocity Magnitude

Time-averaged RMS fluctuating velocity magnitude profiles normal to the blade surface are shown in Figs. 5.17, 5.18, and 5.19. The x-axis is shifted for clarity and

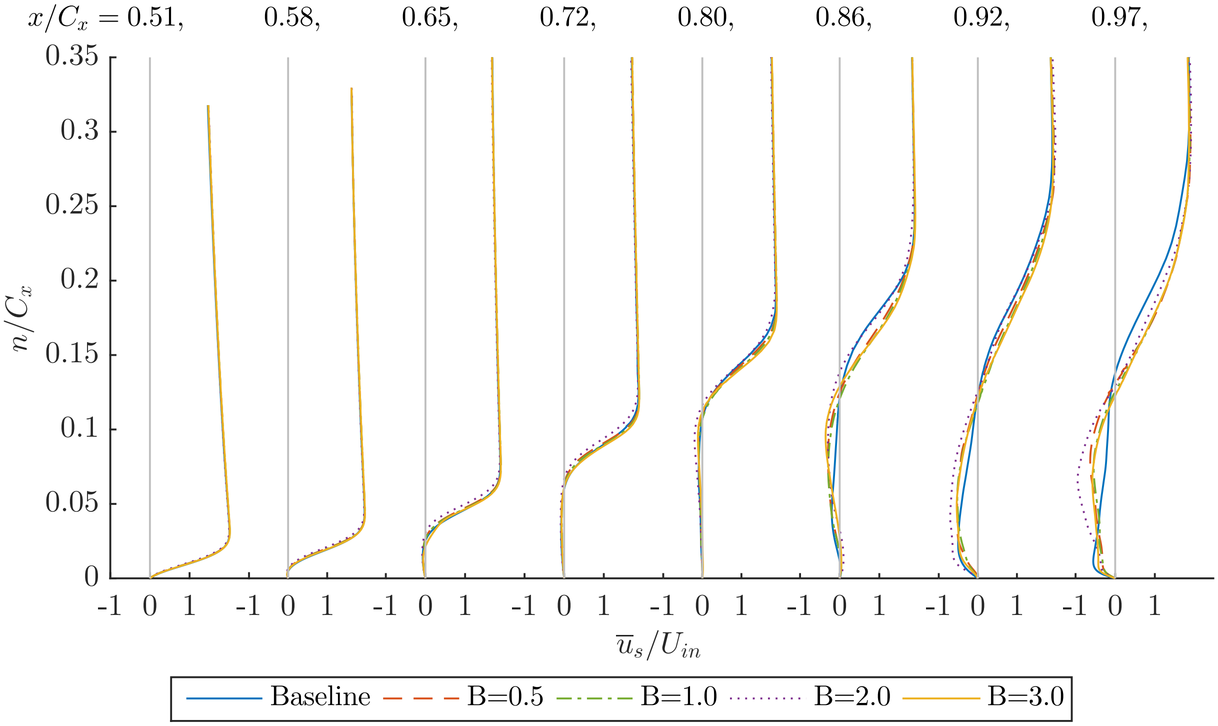

Figure 5.16: Time-averaged blade normal, tangent velocity profiles at eight streamwise stations, Cases 9-12 ($F^+ = 3.02$)

results are displayed at each streamwise station as shown in Fig. 5.3a.

The lowest jet frequency simulation, shown in Fig. 5.17, shows very similar behavior between all flow control cases and the baseline case at the first station. This first station exhibits a very small amount of unsteadiness which is consistent with the well behaved, attached boundary layer as shown in the results of Section 5.4.3. At the second streamwise station, the boundary layer has separated which is shown as the peak in unsteadiness moving away from the blade surface. This peak coincides with the separated shear layer and again reiterates the point that separation occurs before the VGJ is injected into the flow. Moving further downstream the baseline case maintains this peak in unsteadiness up to and including, station $x/C_x = 0.86$. The peak moves away from the blade surface consistent with the growth of the separation bubble. At $x/C_x = 0.65,\ 0.72$ the peak in unsteadiness of the flow control cases is slightly closer to the blade surface, consistent with the observations of the previous section indicating a smaller separation bubble. By $x/C_x = 0.80$ the two highest blowing ratio cases have lost the singular peak in unsteadiness and instead exhibit a broad increase in unsteadiness throughout the separated region. This broad increase is suggestive of the beginnings of transition and is probably responsible for the reduction in separation bubble size at $x/C_x = 0.80$ for Case 4 seen in Fig. 5.11. This large increase in unsteadiness is also responsible for the decrease in coefficient of pressure occurring at $x/C_x = 0.86$ in Case 4. The last three streamwise stations exhibit large unsteadiness for all flow control cases suggesting that all these cases are beginning the transition process and also indicates why the velocity magnitude profiles at these last 3 stations differ so greatly between each of the flow control cases. Case 4 exhibited a broad increase in unsteadiness further upstream than the other cases which could explain why it provides slightly better separation bubble suppression. For streamwise stations where the flow control cases contain a distinctive peak in unsteadiness, it is closer to the blade surface which is consistent with observations in previous sections concerning a slight reduction in separation bubble size.

Next, the middle-frequency case is shown in Fig. 5.18. The first station shows very low levels of unsteadiness and matches between flow control and baseline cases. Again, this is consistent with the well-behaved, attached flow here. The next three stations all show good agreement in the location of the unsteadiness peak while the baseline case calculates a higher level of unsteadiness. This larger peak could be caused by the larger separation bubble in the baseline case. At $x/C_x = 0.80$ the flow control cases begin deviating from the baseline case with a peak in unsteadiness closer to the blade surface. This is consistent with the results of velocity magnitude, seen in Fig. 5.12, which shows this location to be the first one where there is obvious decrease in the separation bubble size. Further downstream, the flow control cases lose their distinctive peak in unsteadiness and exhibit the broad increase in fluctuating velocity. The size of the fluctuating velocity in the last four stations is lower than it was in

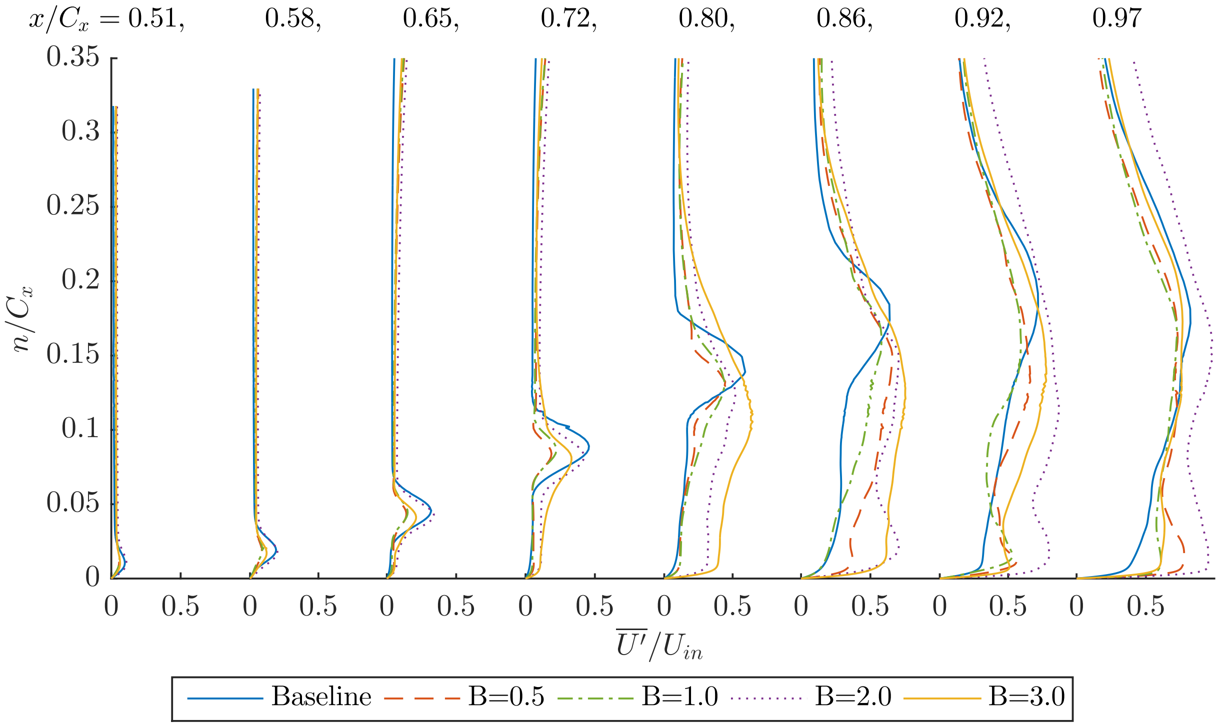

Figure 5.17: Time-averaged blade normal RMS fluctuating velocity magnitude profiles at eight streamwise stations, Cases 1-4 ($F^+ = 0.756$)

the lowest frequency case, described above. This indicates that there is a greater propensity for transition in the low jet frequency case than the middle jet frequency case. This likely contributes to the greater success of the low-frequency jet cases.

Finally, results for the highest jet frequency are shown in Fig. 5.19. In this final case, the location of the unsteadiness peak is the same in flow control and baseline cases all the way up to and including $x/C_x = 0.80$. This is consistent with the velocity magnitude results, shown in Fig. 5.13, which indicates very similar separation bubble size between all cases. One important thing to note is the case corresponding to $BR = 2.0$ which actually predicts the unsteadiness peak slightly higher than the baseline case, indicating a larger separation bubble. This same behavior can be seen in velocity magnitude results (Fig. 5.13), but the disparity in size is very small. This case also has a larger amount of unsteadiness than the other baseline cases. Curiously, looking at previous results this particular case also has the highest integrated wake

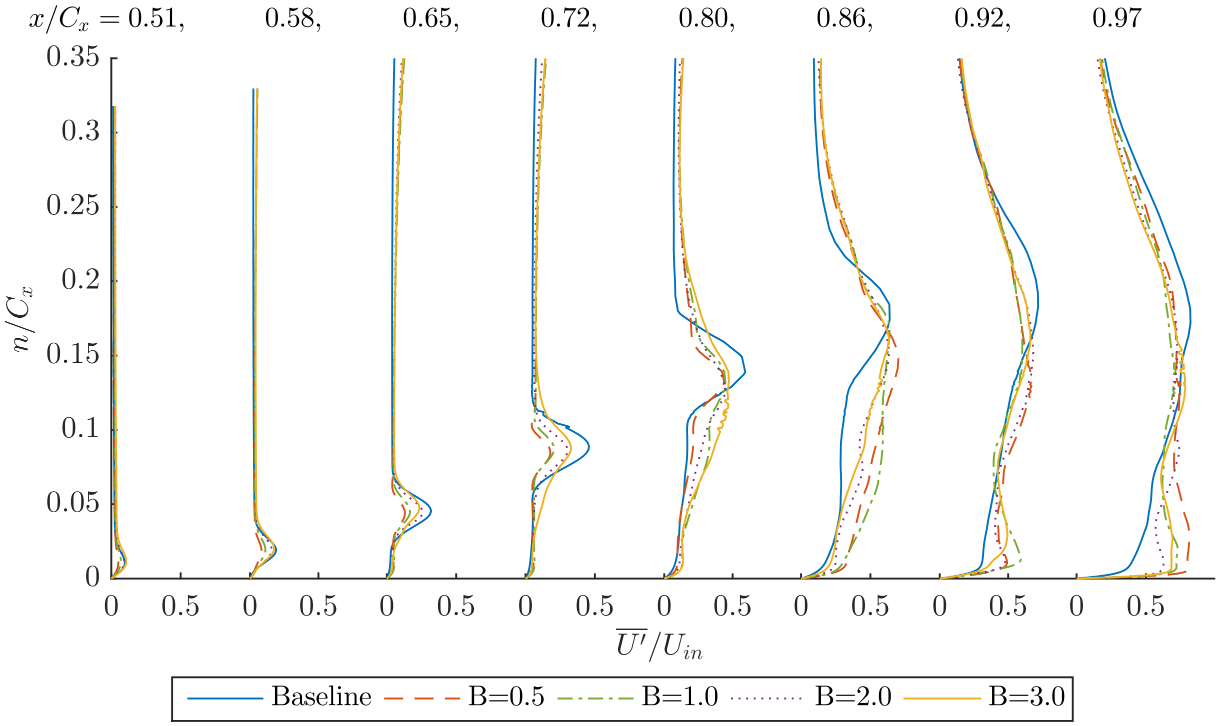

Figure 5.18: Time-averaged blade normal RMS fluctuating velocity magnitude profiles at eight streamwise stations, Cases 5-8 ($F^+ = 1.512$)

loss (Fig. 5.10), a larger wake loss core from the suction surface (Fig. 5.9), and a slightly reduced coefficient of pressure (Fig. 5.6). At station $x/C_x = 0.86$ the flow control cases have lost their distinctive peak and calculate a smaller separation bubble. The remaining stations show a broad amount of unsteadiness throughout the separated flow region similar to results at the lower jet frequencies, but indicate a lesser amount than those cases. As in previous sections, the results here for the highest jet frequency seem to provide the poorest results and even contain one case which seems to increase the amount of separation on the blade.

5.4.6 Turbulent Frequency Spectra

Time histories of fluctuating velocity were obtained at the points shown in Fig. 5.3b and were processed to calculate the frequency spectrum of the turbulent kinetic energy. This analysis shows how much each temporal frequency contributes to the

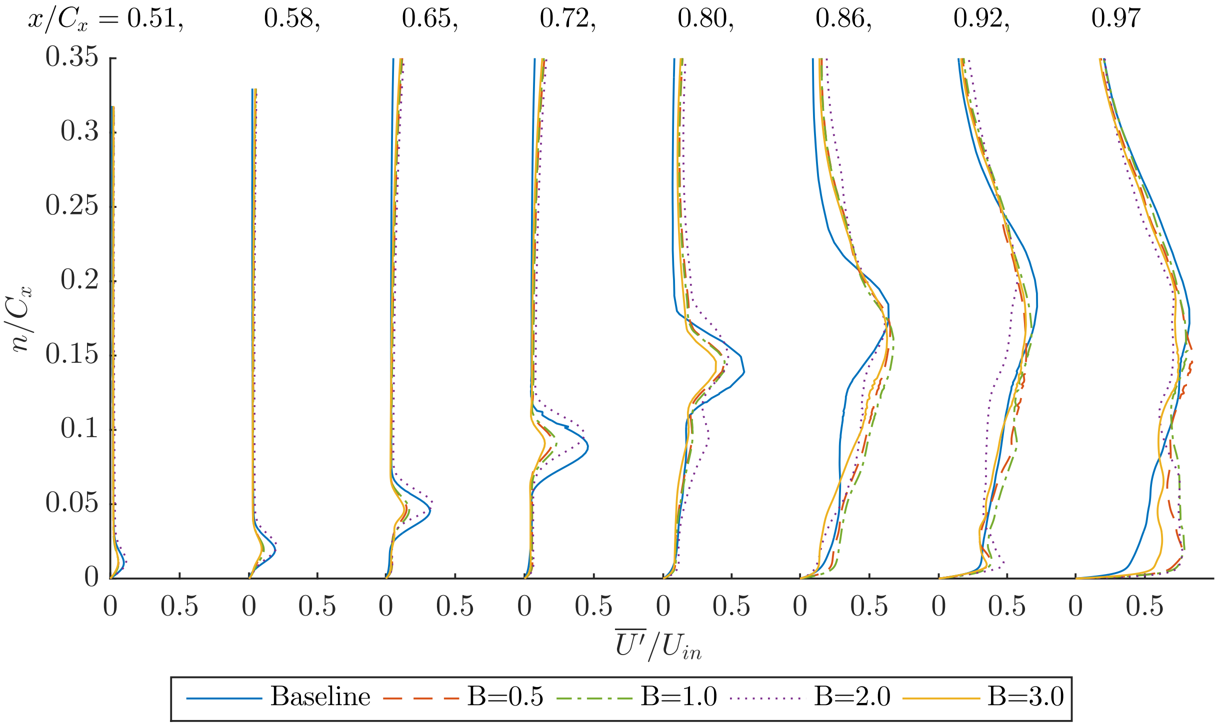

Figure 5.19: Time-averaged blade normal RMS fluctuating velocity magnitude profiles at eight streamwise stations, Cases 9-12 ($F^+ = 3.02$)

turbulent kinetic energy. Results are shown in Figs. 5.20, 5.21, and 5.22. For each of the figures, the three rows correspond to the frequencies simulated starting with the first row at $F^+ = 0.756$ with each subsequent row representing progressively higher frequencies. Each of the columns represents a single streamwise station where the time history of velocity was collected. The particular streamwise station and frequency are displayed on the top right of each plot. The axes of each plot have varying value limits to accommodate the range of the spectrum for the particular location and simulation. The x-axis for each plot is the value of non-dimensional frequency based on the reference velocity, F^+_∞. Table 5.6 shows the F^+_∞ values for each of the three different jet frequencies defined in terms of inlet velocity. These frequencies can be used to identify the influence of the jets present in the turbulent frequency spectra. Integer multiples and divisors of the jet frequency are displayed in the plots by integer values. For all plots, the baseline case turbulent frequency spectra are displayed for comparison. Also in each plot, there are lines of constant slope $-5/3$ and -7 corresponding to the turbulent inertial sub-range and the dissipation range where most of the turbulent kinetic energy is dissipated through viscosity, respectively. For a fully turbulent flow both of these ranges should be distinctly present in the turbulence frequency spectra.

Table 5.6: Non-dimensional jet frequency based on inlet velocity and reference velocity

F^+	F^+_∞
0.756	0.458
1.512	0.916
3.024	1.831

Results for the streamwise stations $x/C_x = 0.65$ and 0.72 are shown in Fig. 5.20 in the left and right columns, respectively. The streamwise station $x/C_x = 0.65$ is just after the VGJ location at $x/C_x = 0.60$, thus, this location should show the influence of the VGJ in the turbulent frequency spectra. For the lowest frequency case (top-left plot) there is a large spike in the frequency spectrum corresponding to twice the jet frequency ($2F^+_\infty$). Observing the results for the highest blowing ratio, there are also spikes at F^+_∞ and $3F^+_\infty$. This indicates the presence of jet frequency harmonics in all flow control cases with the fundamental frequency (the jet frequency) being present in the highest blowing ratio case, Case 4. Interestingly, results discussed previously have shown that Case 4 performed the best in the current simulations. Results for the frequency spectra could indicate this is due to the presence of multiple jet harmonics in the turbulent kinetic energy which contributes substantially. At jet frequency $F^+ = 1.512$ there are two distinctive spikes at $\frac{F^+_\infty}{4}$ and F^+_∞. These spikes are present in all flow control simulations and indicate the VGJ is transferring energy into a lower frequency mode given by the large spectrum value at $\frac{F^+_\infty}{4}$. The highest jet frequency, which also performed the most poorly, only contains higher harmonics of the jet frequency (at low power) and seems to amplify a lower frequency mode similar to the middle jet frequency case. The two larger jet frequencies likely performed more poorly as their energy seems like it was transferred into a lower frequency mode which was probably less effective in controlling separation. The streamwise station $x/C_x = 0.72$ shows very similar results compared with the first station. The lowest jet frequency again contains peaks at the fundamental frequency (F^+_∞) and at $2F^+_\infty$. Both of these peaks are very powerful compared to the rest of the spectrum. The middle jet frequency has the same peaks but with more overall power in the spectrum which is due to being further downstream where more unsteadiness is present. The highest frequency has transferred even more energy to the lower frequency mode while the harmonics at higher modes have diminished. The transfer of energy in both mid- and high-frequency cases to the lower frequency mode, the same frequency in both cases, seems to imply a natural tendency of the flow to accumulate turbulent energy here. This could indicate a natural frequency mode present in the flow field. None of the cases displayed at the first two streamwise stations exhibit inertial sub-range or dissipation turbulent ranges; therefore, the flow at the first stations is still laminar. This is to be expected at the low Reynolds number simulation, $Re_{in} = 10,000$.

Next, turbulent frequency spectra are displayed for streamwise stations $x/C_x = 0.80$ and 0.86 in Fig. 5.21 in the left and right columns, respectively. The first thing to note is the absence of the distinctive peaks that were present at the first two streamwise stations. The locations downstream where time histories were collected are deep inside the separated flow region; hence, the influence of the VGJs has either diffused into the highly unsteady flow region, or the vortical structures of the VGJ have been convected away from the blade toward the separated shear layer, so their presence is not felt close to the blade where time histories were collected. The two lower blowing ratio cases still display the lower frequency mode at the mid- and high-frequency cases; again, insinuating a natural frequency mode where energy has been transferred. At $x/C_x = 0.80$ for the low-frequency cases (top left plot) the lowest blowing ratio case still displays a peak at the fundamental frequency. This could occur

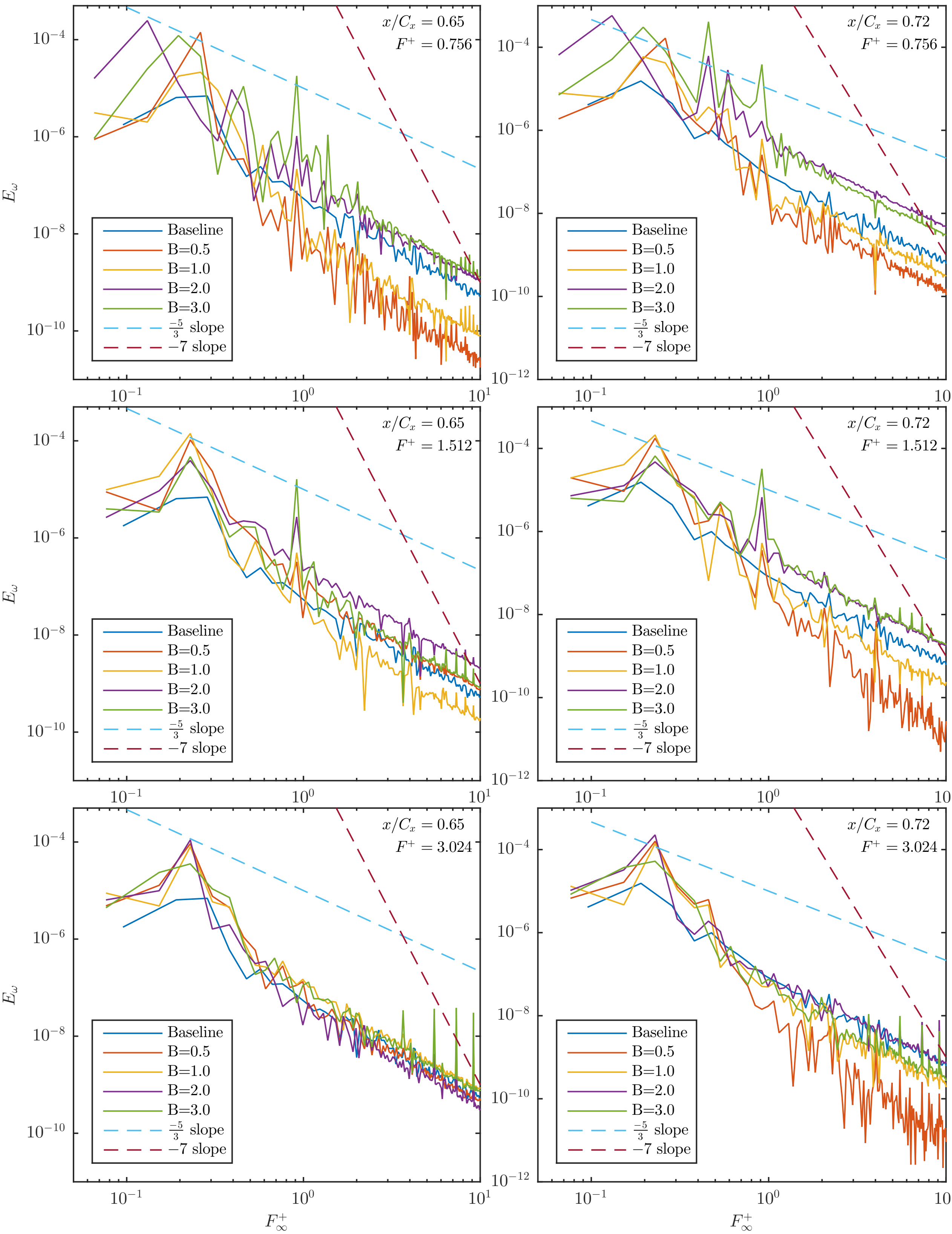

Figure 5.20: Turbulent Kinetic Energy frequency spectra at $x/C_x = 0.65$ (left column) and $x/C_x = 0.72$ (right column) for all cases.

because the low blowing ratio case does not have enough jet momentum to carry the vortex generated by the VGJ away from the blade while the higher blowing ratio cases have been convected from the blade surface by this point. For the streamwise station $x/C_x = 0.86$ at $BR = 2.0$, $F^+ = 0.756$ the spectrum plot shows a narrow dissipative range indicating the beginning of flow transition. A similar but less evident trend can be seen at the same streamwise station for $BR = 1.0$, $F^+ = 1.512$ and $BR = 2.0$, $F^+ = 3.024$.

Finally, Fig. 5.22 shows the turbulent frequency spectra at streamwise stations $x/C_x = 0.92$ and 0.97 in the left and right columns, respectively. Similar to the results at the previous two stations the mid- and high-frequency cases have a large peak at the low-frequency harmonic mode, but there are no other distinctive peaks corresponding to harmonics of the jet frequencies. Various results at the last two stations are starting to show a narrow inertial sub-range both in the baseline case and the flow control cases. Results corresponding to $x/C_x = 0.97$, $BR = 0.5$, $F^+ = 1.512$ show a small dissipation range, but lack the inertial sub-range. Even by the last streamwise station there is no single case which has become fully turbulent. The fluctuating velocity results in Section 5.4.5 suggest that the beginnings of transition are present with the broad unsteadiness in the separated region, and the results of the turbulence frequency spectra support this suggestion by the presence of a limited inertial sub-range.

In comparing the flow control and baseline cases in the turbulent frequency spectra the flow control cases contain a larger amount of power in the lower frequencies. The mid- and high-frequency cases, in particular, contain a low harmonic of the jet frequency. These results suggest that the VGJ effects are transferred into the lower frequency modes.

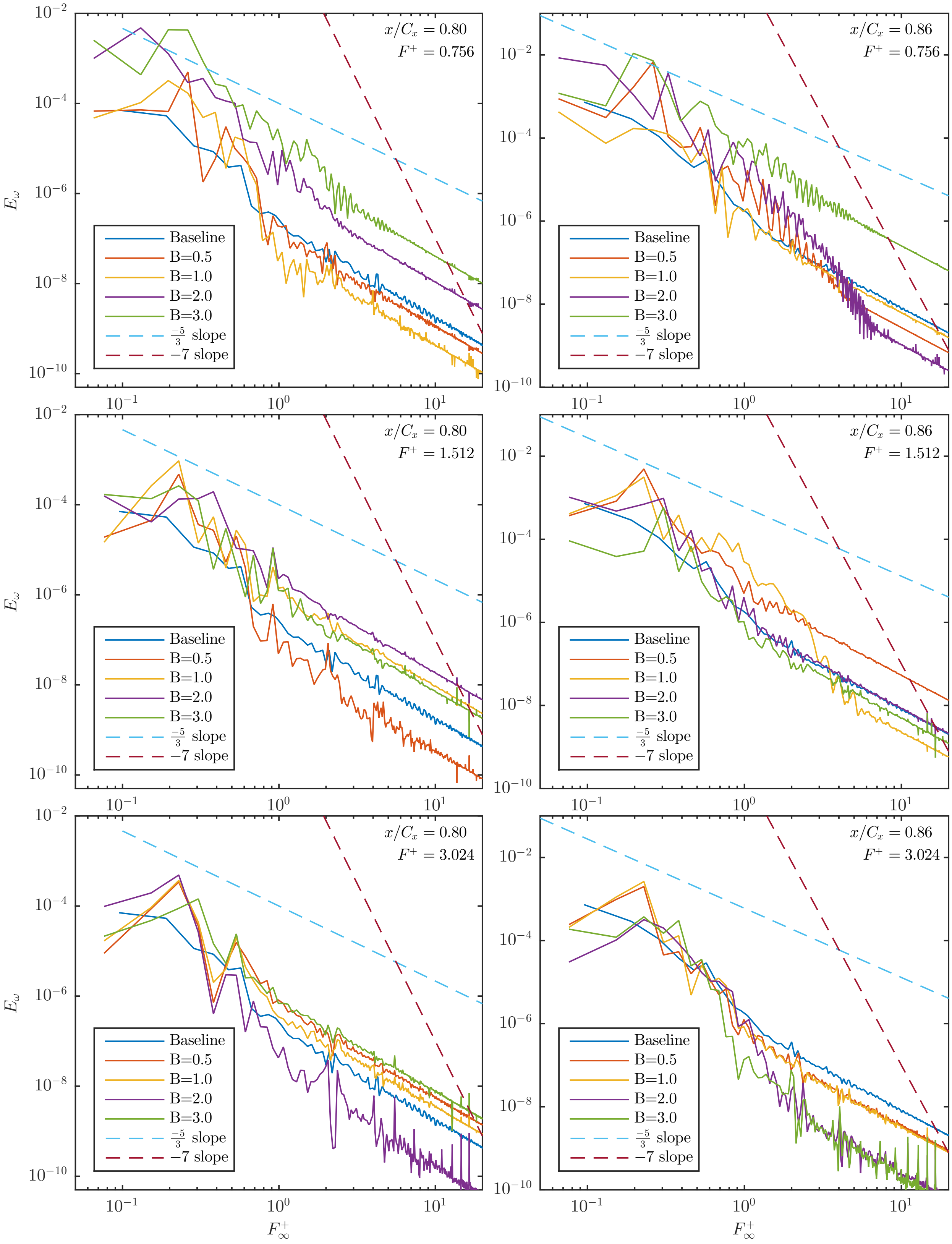

Figure 5.21: Turbulent Kinetic Energy frequency spectra at $x/C_x = 0.80$ (left column) and $x/C_x = 0.86$ (right column) for all cases.

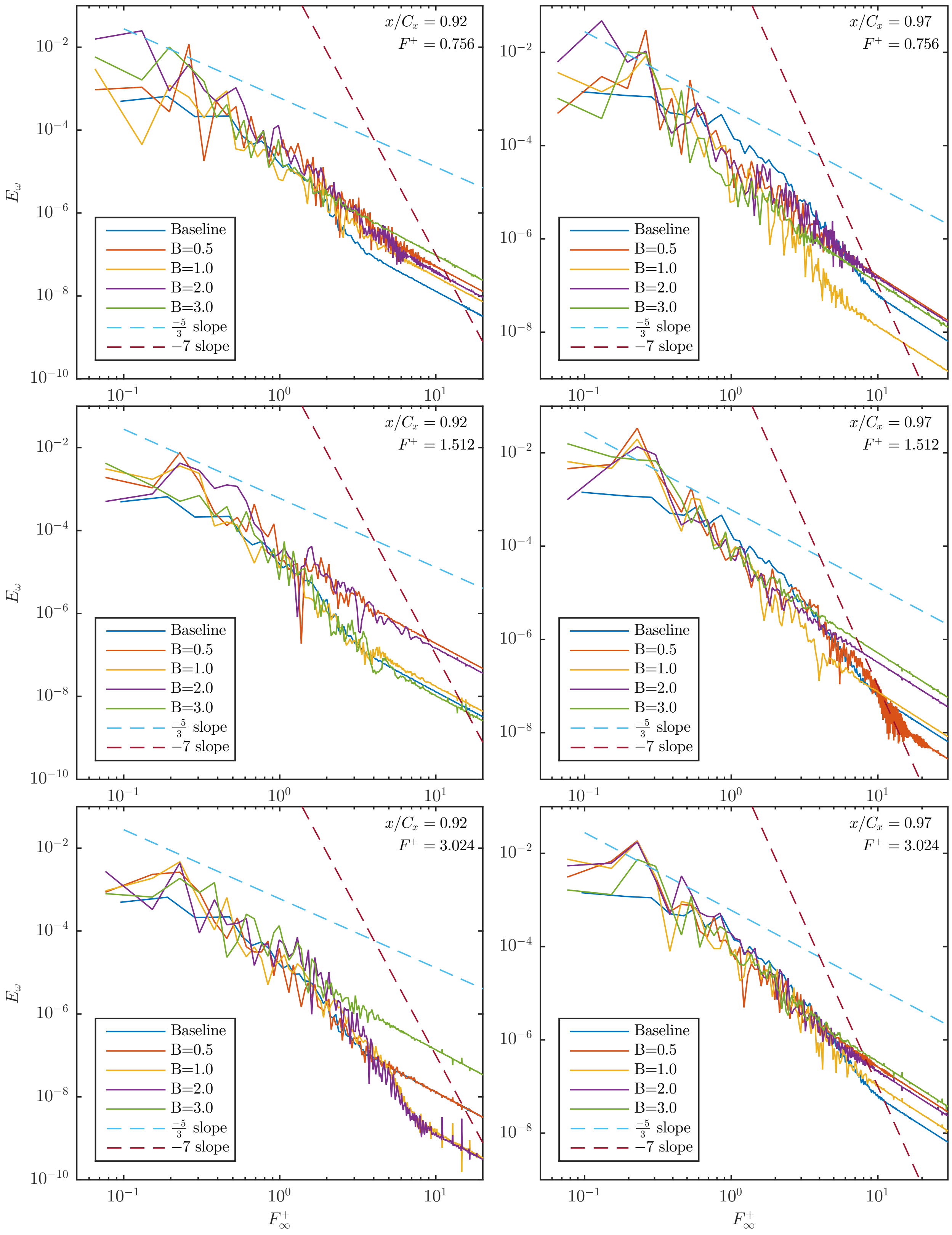

Figure 5.22: Turbulent Kinetic Energy frequency spectra at $x/C_x = 0.92$ (left column) and $x/C_x = 0.97$ (right column) for all cases.

5.5 Upstream Jet Simulations

The L2A simulation results above indicate that the VGJ was most assuredly placed downstream of the separation point. This will reduce the efficacy of the jets as the large separation present downstream of the separation point makes it much more difficult to entrain freestream momentum in order to energize the boundary layer and mitigate separation. Sondergaard et al. (2002) tested different streamwise locations for the VGJ with respect to the separation point. They found locations both upstream and downstream of the separation point to be effective but those upstream and closer to the point of separation required less jet mass to control separation. In light of the results of this research and the current study two simulations were conducted with the location of the VGJ moved upstream of the separation point.

First, results for the tangent velocity profile near the blade surface were investigated close to the blade to make a better determination of the actual separation point. These results were analyzed for the time-averaged baseline flow case. Figure 5.23 below shows the blade normal, tangent velocity profile at eight different streamwise stations. One can see that the velocity gradient just above the blade slowly decreases until it reaches a zero value at $x/C_x = 0.55$. After this point, there is a component of reverse flow indicating that separation has occurred. Based on these results the baseline case is considered to separate at $x/C_x = 0.55$. In order to increase the effectiveness of the VGJ an upstream location at $x/C_x = 0.53$ was selected. At this streamwise station, the boundary layer is still attached and is well upstream of the large separation present further downstream.

Now that the upstream location has been selected, two simulations from the previous twelve L2A simulations were selected for re-simulation with the upstream VGJ. The two simulations selected represented the best and worst flow controlling cases. The best flow control simulation was Case 4 ($BR = 3.0,\ F^+ = 0.756$) as documented by the results in Section 5.4. Based on the results of that section the higher frequency

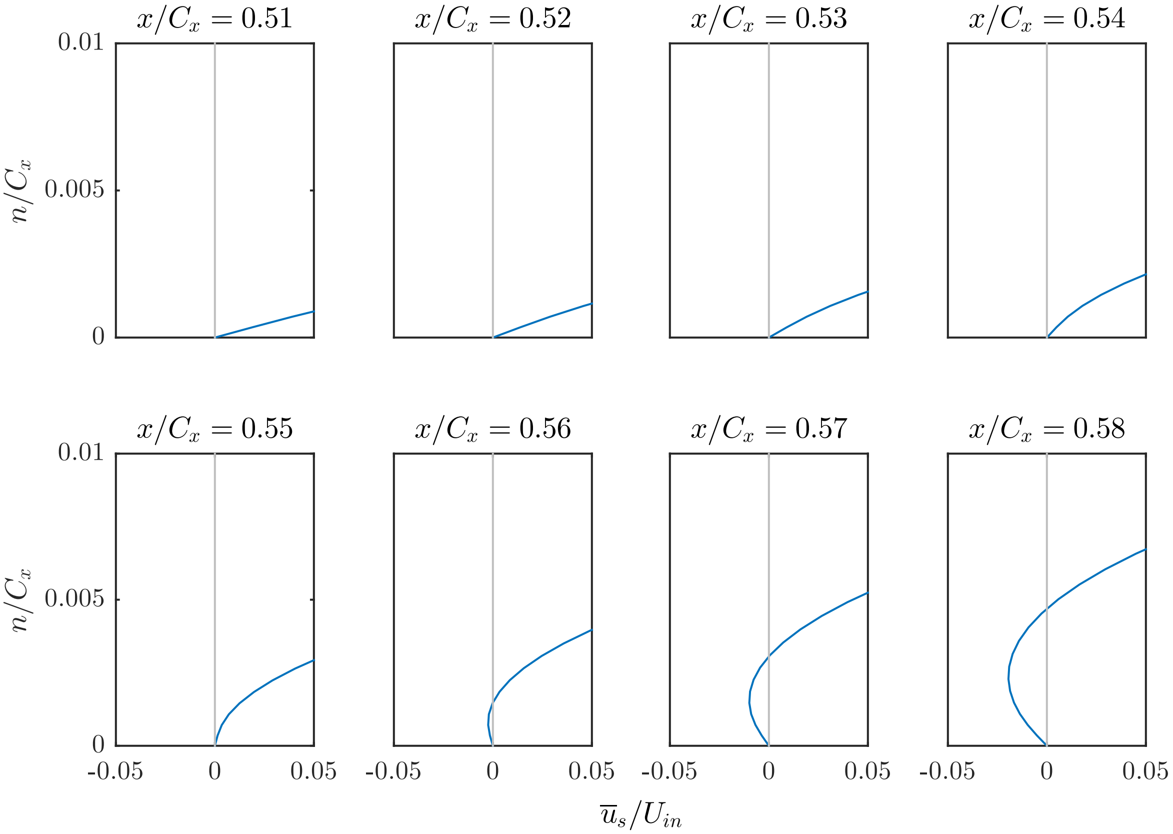

Figure 5.23: Blade normal, tangent velocity at various streamwise stations for the baseline flow

cases provided less control. Coupling this with the fact that a lower BR usually provides less control, Case 9 ($BR = 0.5,\ F^+ = 3.02$) was considered to have the worst jet effectiveness.

Two simulations were setup using the same jet parameters from Case 4 and Case 9. The only difference was the location of the jet being at $x/C_x = 0.53$ instead of the original position of $x/C_x = 0.60$. These two locations will be referred to as the upstream (US) VGJ and the downstream (DS) VGJ, respectively, from here on. Changing the jet location required reformulating the blade mesh since points are concentrated in the vicinity of the jet to increase the fidelity of the local solution. The mesh dimensions were kept the same, but points were redistributed to maintain the same points/arc-length density that was present on the blade surface before and after the VGJ in the original L2A flow control mesh. Once this change was accomplished simulations were executed using the same timing information for Case 4 and Case 9 present in Section 5.1.

The next several sections present the results for the US VGJ simulation compared with the DS VGJ and the baseline case. These comparisons are accomplished for VGJs as defined in Case 4 and Case 9.

5.5.1 Coefficient of Pressure

Results for the time-averaged coefficient of pressure (defined in Eq. 5.1) are shown in Figs. 5.24 and 5.25. These results compare the US VGJ and DS VGJ implementations for the same jet; additionally, the baseline case is shown for reference. The first set of results are for the best performing case in the original L2A simulations. This corresponds to Case 4 with jet parameters of $F^+ = 0.756$ and $BR = 3.0$ and is shown in Fig. 5.24. The results for C_p show that moving the VGJ upstream has a noticeable improvement for the blade. The point of peak suction has moved further downstream to $x/C_x \approx 0.47$ and the peak suction has also increased. There is still a plateau characteristic of separation but there are also signs of reattachment with the rapid decrease occurring in C_p at $x/C_x \approx 0.75$ and 0.86. These results show a definite increase in the performance of the blade approaching the attached C_p profile of the blade. In this case, moving the VGJ upstream of the time-averaged separation point has provided a definite increase in C_p profile.

The second set of results is for the worst-performing jet case in the original L2A simulations. This corresponds to Case 9 with jet parameters of $F^+ = 3.02$ and $BR = 0.5$ and is shown in Fig. 5.25. These results are nearly identical to the simulation of the DS VGJ. There are some variations near the trailing edge of the blade but the characteristics of the peak suction and separated region are essentially the same and additionally match the baseline case. For this particular VGJ configuration, the movement of the jet to an upstream position does not seem to have any improvement for the separation characteristics.

While the best-performing jet case has shown a definite improvement in results from the movement of the VGJ to an upstream position, this improvement seems to also be influenced by the other jet parameters as shown by the worst performing jet case not benefiting from an upstream position of the jet.

5.5.2 Wake Loss

Results for the time-averaged wake loss, defined in Eq. 4.5, are shown in Figs. 5.26 and 5.27. These results were extracted from the pitch axis of the turbine cascade just after the blade trailing edge at $x/C_x = 1.05$. Results for the best-performing jet are shown in Fig. 5.26. As with the C_p results, the wake loss values show a definite improvement resulting from the upstream jet. The US VGJ shows a more narrow wake loss profile indicating a smaller separated region and a much smaller maximum loss value compared to the DS VGJ and baseline cases. There are still two peaks in the wake loss profile which correspond to the large vortices shed from the trailing

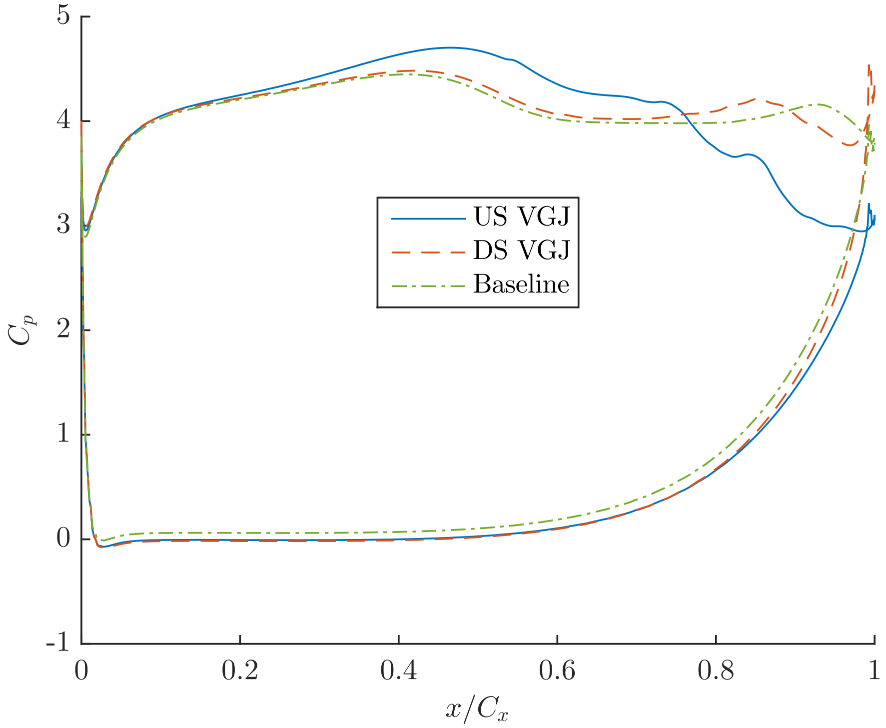

Figure 5.24: C_p surface distribution comparison for jet with $F^+ = 0.756$ and $BR = 3.0$

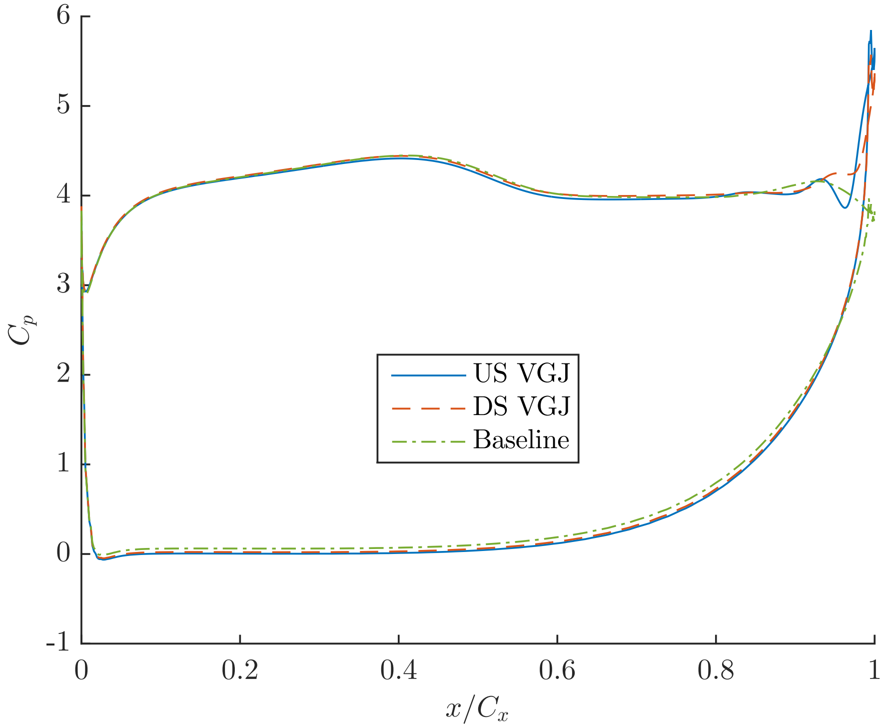

Figure 5.25: C_p surface distribution comparison for jet with $F^+ = 3.02$ and $BR = 0.5$

edge of the turbine blade.

Figure 5.27 shows the results from the worst-performing jet case. The US VGJ, in this case, has a very similar profile to the DS VGJ. There is a possible slight narrowing of the wake loss profile but overall the change in results is not significant.

The wake loss profiles compound the results seen in C_p results and further show that moving the VGJ upstream can improve flow control given a powerful enough jet.

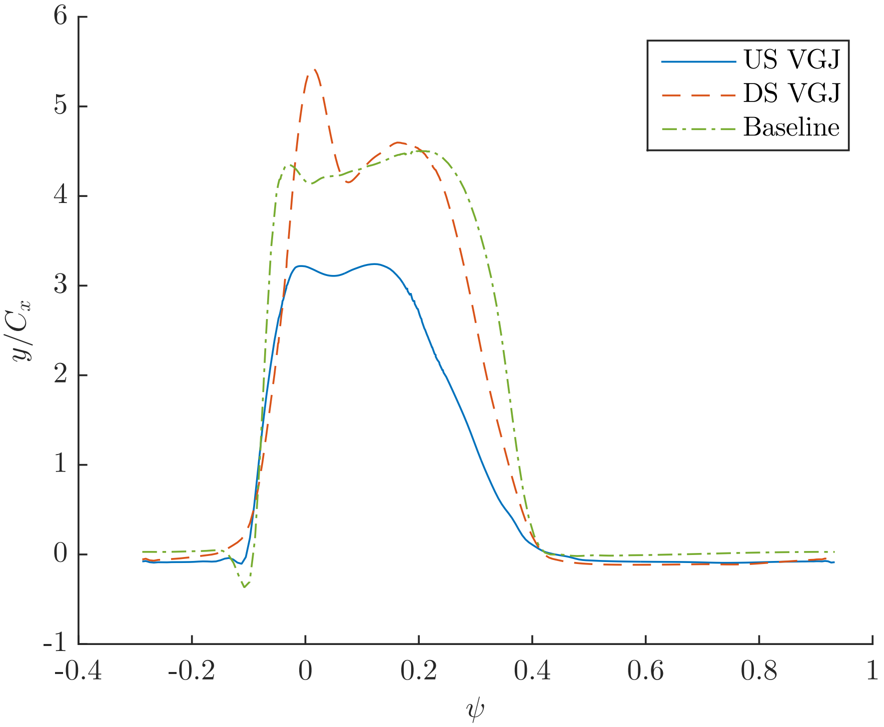

Figure 5.26: Wake Loss at $x/C_x = 1.05$ for jet with $F^+ = 0.756$ and $BR = 3.0$

Integrated wake loss, as defined in Eq. 5.2, compares all 12 original L2A simulations with the two new simulations, shown in Fig. 5.28. All values here were normalized by the integrated wake loss value calculated for the baseline case. Consistent with the results discussed so far, the best-performing jet moved upstream (US VGJ$_1$) provides a definite improvement in separation losses. The best performing case moved upstream provides a 42% reduction in the integrated wake loss over the baseline case. The worst-performing jet moved upstream (US VGJ$_2$) provides

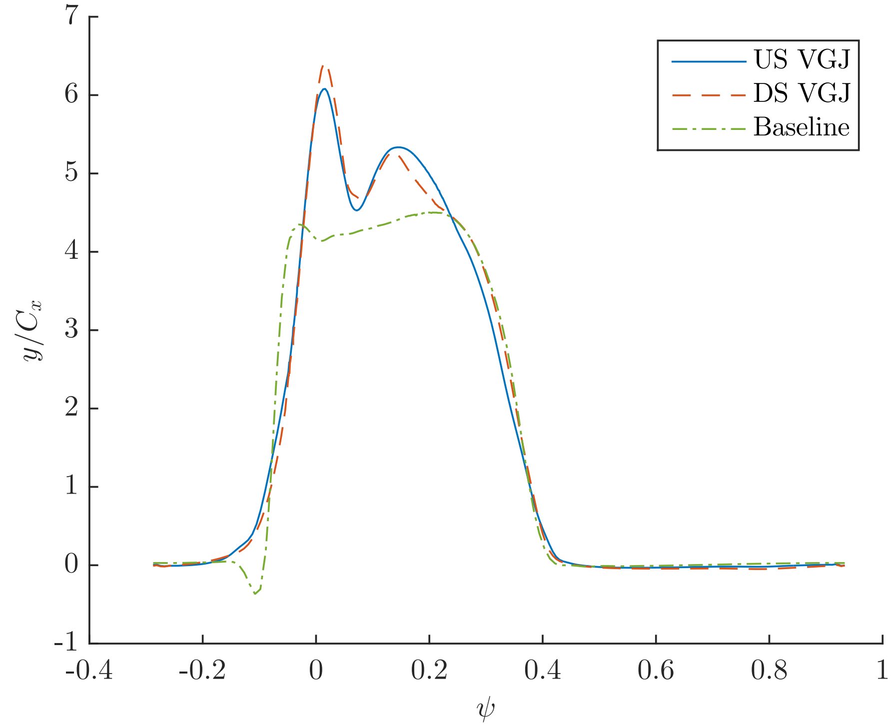

Figure 5.27: Wake Loss at $x/C_x = 1.05$ for jet with $F^+ = 3.02$ and $BR = 0.5$

almost no change over its downstream counterpart.

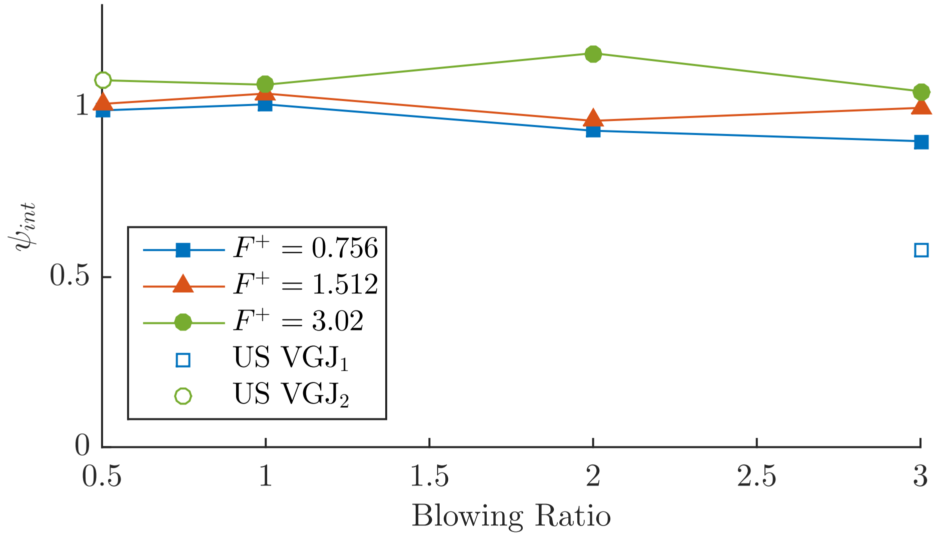

Figure 5.28: Integrated Wake Loss normalized by baseline compared for all 12 DS VGJs with two upstream, US VGJ$_1$ ($F^+ = 0.756$) and US VGJ$_2$ ($F^+ = 3.02$)

5.5.3 Blade Normal Velocity Magnitude

Time-averaged velocity magnitude profiles normal to the blade surface are shown in Figs. 5.29 and 5.30. The x-axis is shifted for clarity and eight streamwise stations are displayed as shown in 5.3a.

The best performing jet, shown in Fig. 5.29, shows improvement from moving the jet upstream at all streamwise stations. Even at the first streamwise station there is a slight improvement in that the velocity gradient changes more rapidly close to the blade. This result is the same at each downstream station as the US VGJ reaches the freestream velocity values closer to the blade than the DS VGJ or the baseline case. As with previous results the worst performing case, shown in Fig. 5.30, does not benefit from moving the jet upstream. The results are largely the same between the US VGJ and the DS VGJ. The only streamwise station with any improvement would be $x/C_x = 0.92$ where the US VGJ reaches freestream velocity values slightly closer to the blade than the DS VGJ.

5.5.4 Blade Normal Tangent Velocity

Time-averaged blade normal, tangent velocity profiles are shown in Figs. 5.31 and 5.32. The x-axis is shifted for clarity and eight streamwise stations are displayed as shown in 5.3a. These results offer an alternative view of the velocity profiles close to the blade and allow for the visualization of reverse flow regions which are typically present in separated regions.

Figure 5.31 shows the results for the best performing jet. These results again show that moving the jet upstream has provided an increase in separation mitigation at all streamwise stations. Even at the first streamwise station ($x/C_x = 0.51$) there is a slight improvement as shown by the velocity gradient increase closer to the blade surface. The presence of reverse flow at station $x/C_x = 0.72$ for the US VGJ case indicates that the separation bubble has been reduced in streamwise extent, thus

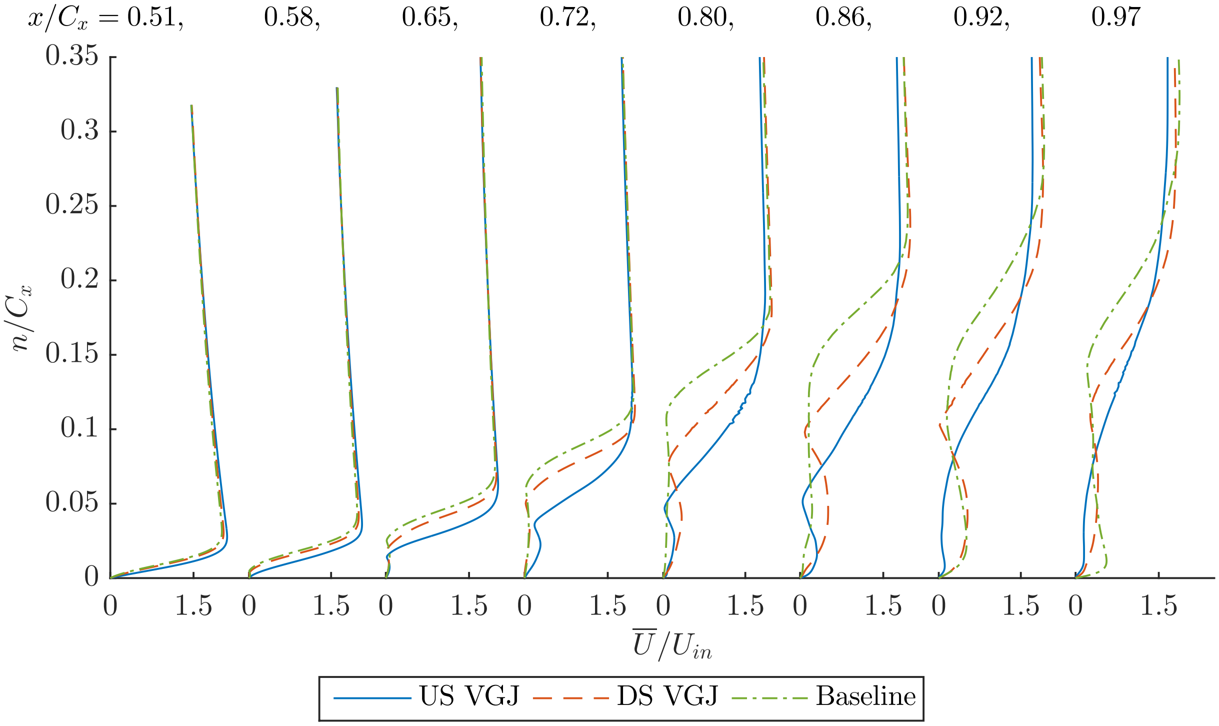

Figure 5.29: Time-averaged blade normal velocity magnitude profiles, comparing US VGJ, DS VGJ, and baseline for jet with $F^+ = 0.756$ and $BR = 3.0$

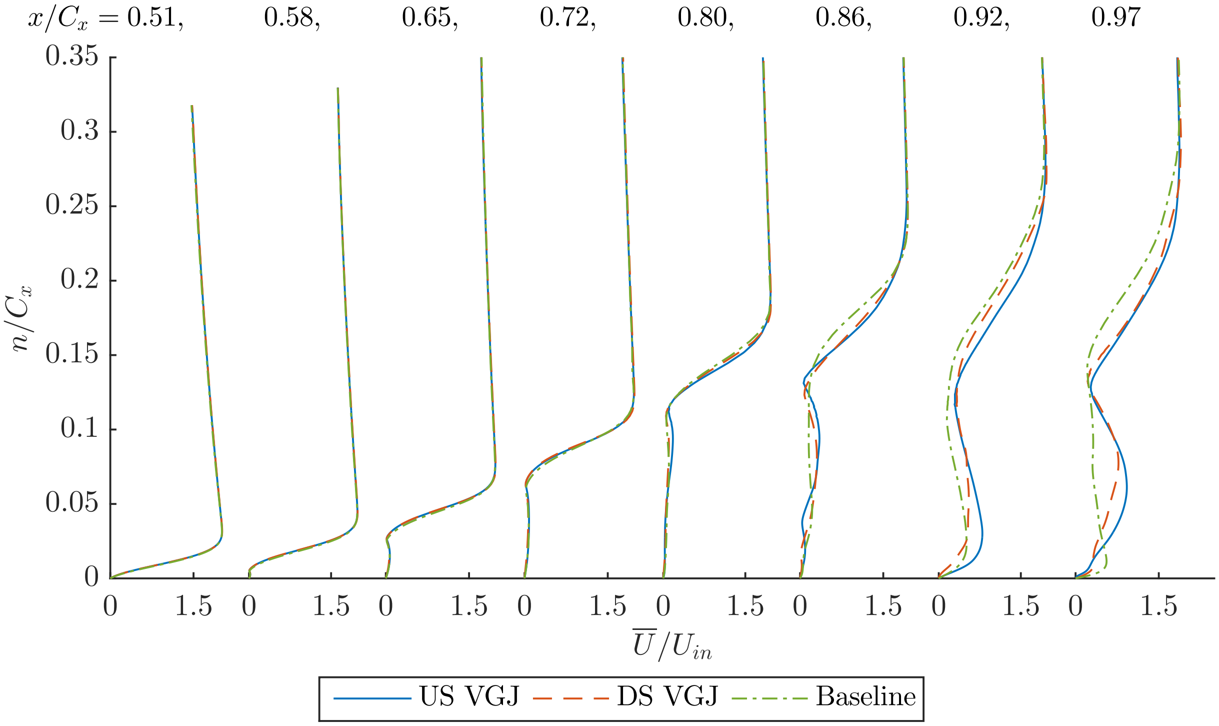

Figure 5.30: Time-averaged blade normal velocity magnitude profiles, comparing US VGJ, DS VGJ, and baseline for jet with $F^+ = 3.02$ and $BR = 0.5$

moving the reverse flow vortex further upstream. This station also shows a larger region where the velocity transitions from zero to the freestream value indicating a diffusion of the shear layer. These results also show that by station $x/C_x = 0.92$ the US VGJ case contains no reverse flow region but still maintains a greatly retarded velocity gradient close to the blade. At the next station, $x/C_x = 0.97$, there is a positive velocity value throughout the entire normal profile. This indicates that the boundary layer is starting to redevelop and the separation bubble is no longer present. This suggests that flow has reattached by $x/C_x = 0.92$, a definite improvement over the DS VGJ case which still contains reverse flow at the blade trailing edge.

The worst performing jet case, shown in Fig. 5.32, contains very similar behavior between the US VGJ and DS VGJ cases. As with the blade normal velocity magnitude results, there is a slight improvement at $x/C_x = 0.92$ with the US VGJ providing a slightly reduced separated region but also exhibiting a larger reverse flow region.

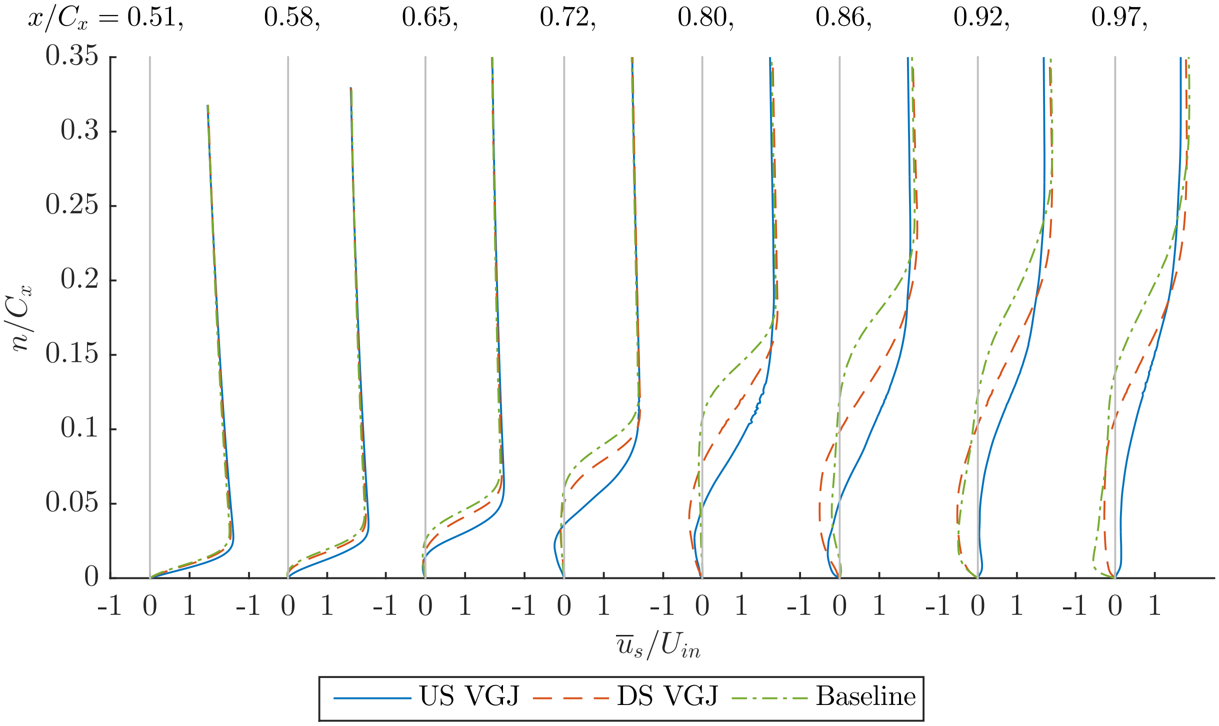

Figure 5.31: Time-averaged blade normal, tangent velocity profiles, comparing US VGJ, DS VGJ, and baseline for jet with $F^+ = 0.756$ and $BR = 3.0$

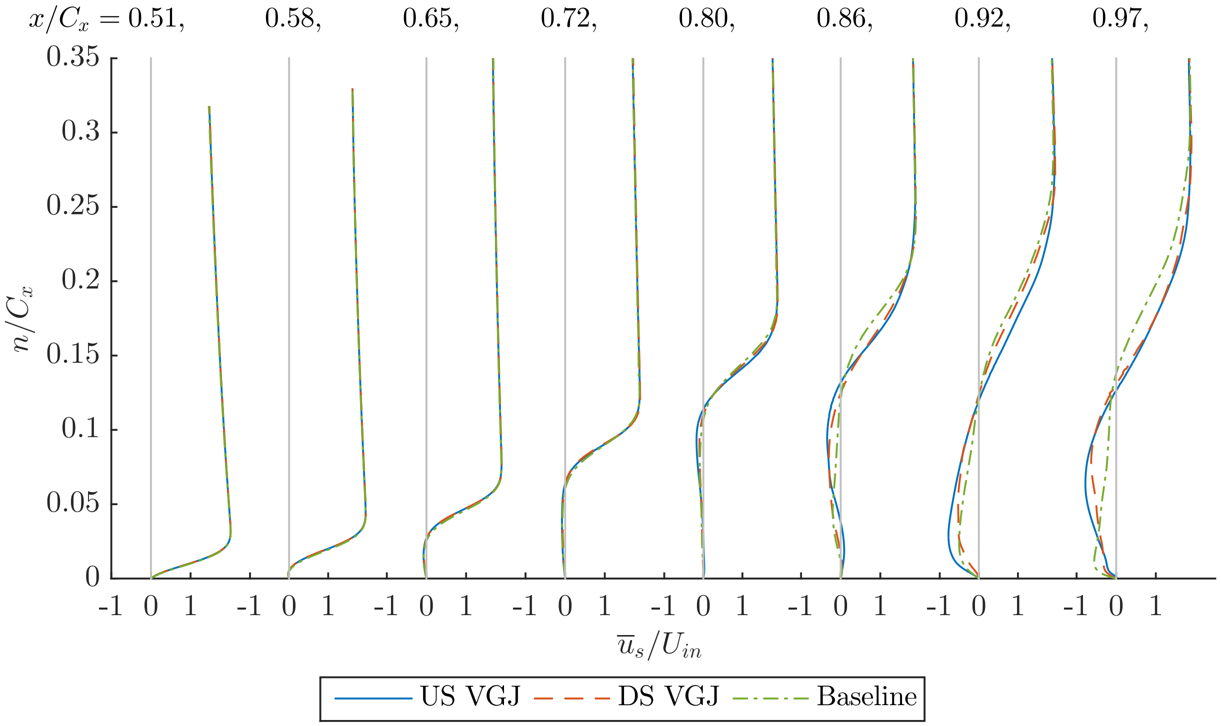

Figure 5.32: Time-averaged blade normal, tangent velocity profiles, comparing US VGJ, DS VGJ, and baseline for jet with $F^+ = 3.02$ and $BR = 0.5$

5.5.5 Blade Normal RMS Fluctuating Velocity Magnitude

Time-averaged RMS fluctuating velocity magnitude profiles normal to the blade surface are shown in Figs. 5.33 and 5.34. The x-axis is shifted for clarity and results are displayed at each streamwise station as shown in 5.3a.

The best performing jet case is shown in Fig. 5.33. At the first streamwise station, $x/C_x = 0.51$, all cases are very similar with a small amount of unsteadiness. By the second station, the US VGJ shows a larger degree of unsteadiness than the DS VGJ. At the third station, the US VGJ has a broader and more powerful peak in the unsteadiness profile than the DS VGJ. This peak is also closer to the blade. These facts indicate that the US VGJ has caused a larger amount of unsteadiness in the separated shear layer which has moved the shear layer closer to the blade and reduced the size of the separation bubble. At $x/C_x = 0.72$ the US VGJ no longer exhibits a distinctive peak in the unsteadiness levels which would correspond with a coherent separated shear layer. Instead, there is a broad span of large unsteadiness indicating that the shear layer has started to diffuse and the beginnings of transition have occurred. This also coincides with the streamwise station where reverse flow first begins for the US VGJ. In contrast, the DS VGJ does not exhibit this broad unsteadiness until $x/C_x = 0.80$ where the US VGJ still has a broader and more powerful unsteadiness profile, especially when observing near the blade. Further downstream, the US VGJ and DS VGJ have similar amounts of unsteadiness, both in terms of broadness and power, however, the US VGJ has a greater amount of unsteadiness closer to the blade surface.

The worst performing jet case is shown in Fig. 5.34. The US VGJ has a very similar profile to the DS VGJ at all stations except the last two. However, at the first four streamwise stations, the US VGJ shows a larger peak in unsteadiness. This indicates that even though the US VGJ did not provide more effective separation, as shown in previous results, its jet has imparted a larger degree of unsteadiness after the jet location. This indicates that moving the VGJ upstream does provide a benefit even for the worst performing case but suggests that this jet is not powerful enough to affect the large degree of separation.

Overall, moving the VGJ upstream helped to provide more unsteadiness in the separated flow in both the best and worst performing jet cases. The best jet allowed for diffusion of the shear layer to occur further upstream while the worst jet increased overall unsteadiness just after the VGJ but before diffusion of the shear layer. The worst jet likely has insufficient power to affect the large amount of separation.

5.5.6 Turbulent Frequency Spectra

Time histories of fluctuating velocity were obtained at the points shown in Fig. 5.3b and were processed to calculate the frequency spectrum of the turbulent kinetic energy. This analysis indicates how much turbulent kinetic energy each temporal fre-

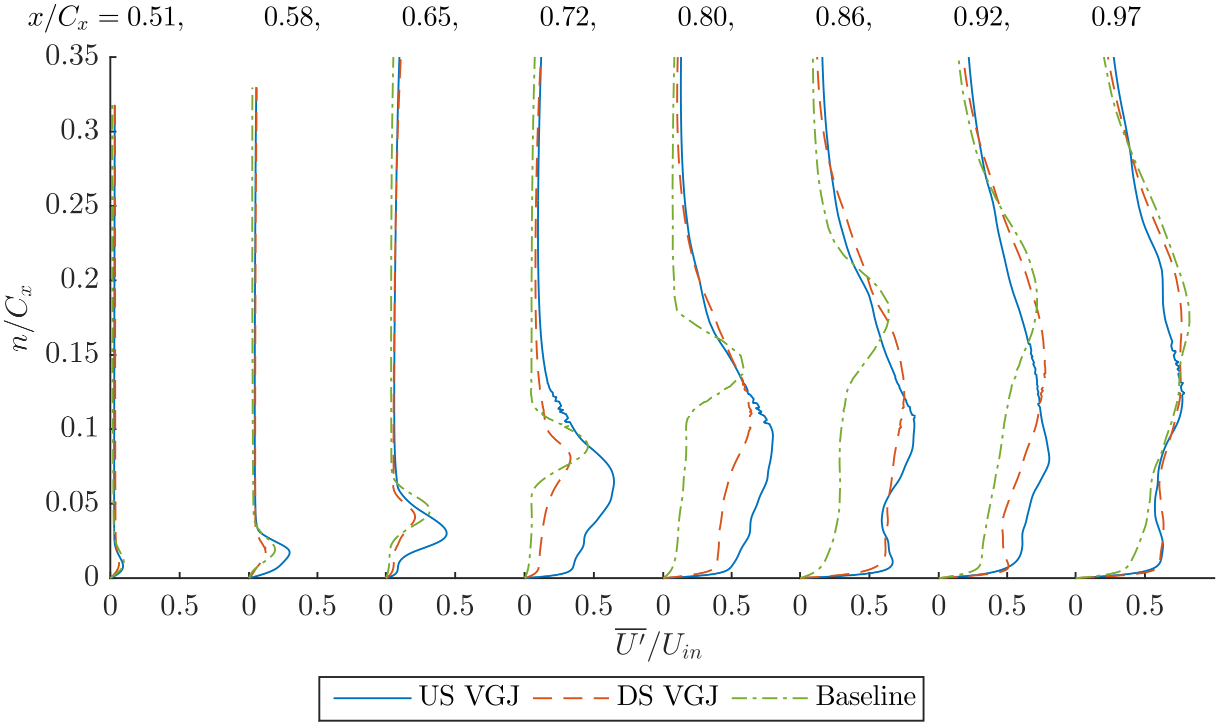

Figure 5.33: Time-averaged blade normal RMS fluctuating velocity magnitude profiles, comparing US VGJ, DS VGJ, and baseline for jet with $F^+ = 0.756$ and $BR = 3.0$

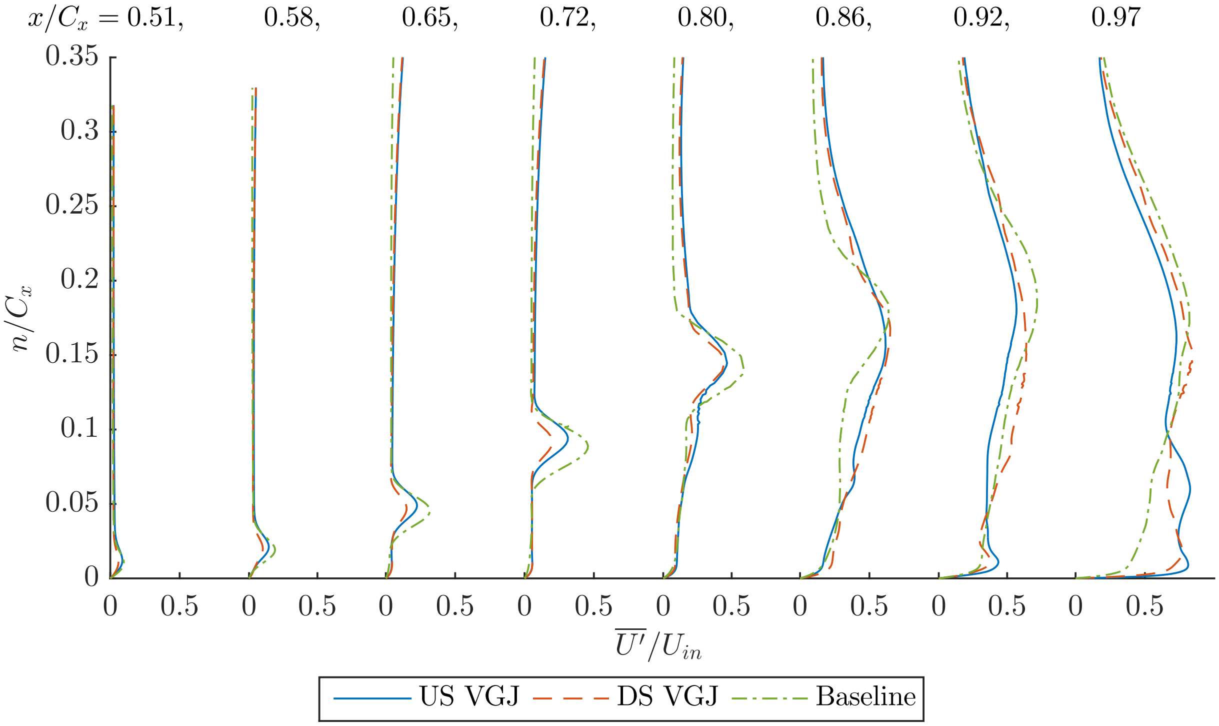

Figure 5.34: Time-averaged blade normal RMS fluctuating velocity magnitude profiles, comparing US VGJ, DS VGJ, and baseline for jet with $F^+ = 3.02$ and $BR = 0.5$

quency contains. Results are shown in Figs. 5.35 and 5.36. Each figure contains all six streamwise stations where data was collected. The top right corner of each plot displaying the particular streamwise station. The axes of each plot have varying value limits to accommodate the range of spectrum values. The x-axis for each plot is the value of non-dimensional frequency based on reference velocity, F^+_∞. Refer to Table 5.6 for the relationship between F^+_∞ and F^+ values. The baseline case turbulent frequency spectra are displayed for reference. Also in each plot, there are lines of constant slope $^{-5}/_{3}$ and -7 corresponding to the turbulent inertial sub-range and the dissipation range where most of the turbulent kinetic energy is dissipated through viscosity, respectively. For a fully turbulent flow both of these ranges should be distinctly present in the turbulence frequency spectra.

Results for the best performing jet case are shown in Fig. 5.35. As discussed in Section 5.4.6 there are multiple jet frequency harmonics present in the DS VGJ case at the first streamwise station, $x/C_x = 0.65$. The US VGJ case also displays these same harmonics but they are more powerful and contains additional harmonics at $4F^+_\infty$ and $5F^+_\infty$. As mentioned before, the presence of these harmonics likely greatly contributes to the control of the separated flow region. Given that there are more harmonics present and they are more powerful in the US VGJ case explains in part why moving the jet further upstream provides such a benefit to flow control. Further downstream, at $x/C_x = 0.72$ the US VGJ again shows the same harmonics present for the DS VGJ case but they are more powerful. Overall, at the first two streamwise stations the US VGJ contains more power in the TKE spectrum than the DS VGJ case likely because of the decreased size of the separated flow region. Unlike the DS VGJ, the US VGJ still contains the presence of the jet frequency at $x/C_x = 0.80$ indicating that the US VGJ is able to penetrate further downstream and remain close to the blade because of the decreased size of the separated flow region. Further downstream, the power levels of the US VGJ and DS VGJ case are very similar and there are no longer any jet frequency harmonics present. This far downstream the different effects of the US VGJ and DS VGJ are not discernible which agrees with the RMS fluctuating velocity results from Fig. 5.33. There are no inertial sub-range or dissipation ranges present in the frequency spectrum suggesting that the flow is still laminar.

Results for the worst performing jet are shown in Fig. 5.36. As discussed in previous sections the movement of this jet upstream did little to improve the separation mitigation. In these results we see that the US VGJ shows the same large peak at the lower frequency harmonic mode that the DS VGJ does. At streamwise stations $x/C_x = 0.72,\ 0.80,$ and 0.86 the US VGJ shows higher amounts of energy in the mid and high frequency ranges. This supports the results of the RMS fluctuating velocity, Fig. 5.34, which showed higher unsteadiness peaks for the US VGJ. As before, the movement of the jet upstream seems to have increased the unsteadiness of the flow for the worst performing jet, but the jet is not powerful enough to take advantage of this increased unsteadiness to limit the separated flow region.

5.6 Discussion

In light of the results discussed in Sections 5.4 and 5.5 an overall discussion incorporating elements from each section is merited and discussed here.

Overall the results for each of the DS VGJs show that the VGJs did offer a small degree of separation control. This is shown as a narrowing of the wake loss profile, a blade normal velocity profile that reaches freestream values closer to the blade surface, and peak fluctuating velocity values closer to the blade surface (corresponding to the separated shear layer). Two jet configurations, corresponding to the best and worst performing DS VGJs, were moved upstream for re-simulation. These US VGJs showed a drastic improvement in the low frequency, high blowing ratio case. For the

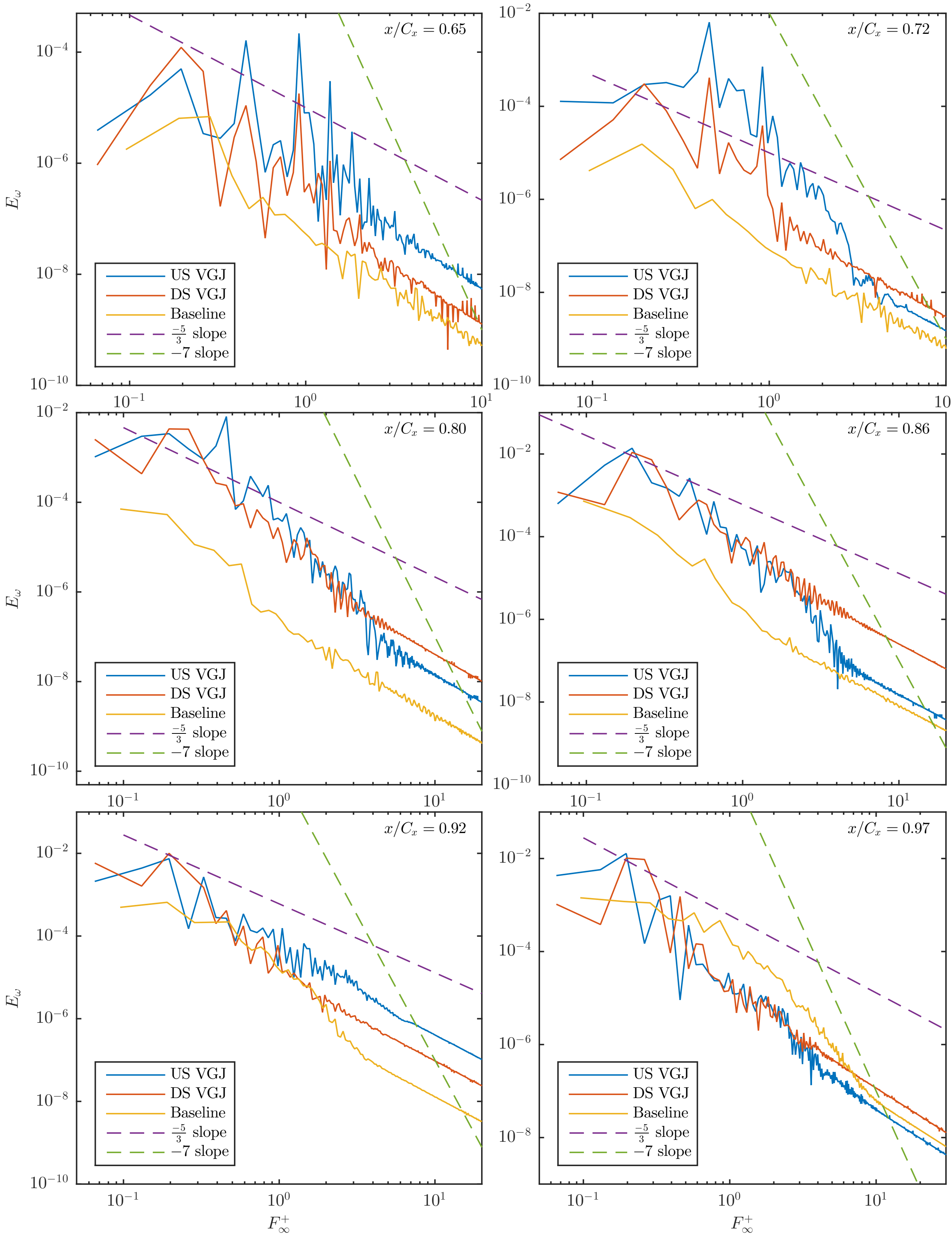

Figure 5.35: Turbulent Kinetic Energy frequency spectra at six streamwise stations, comparing US VGJ, DS VGJ, and baseline for jet with $F^+ = 0.756$ and $BR = 3.0$

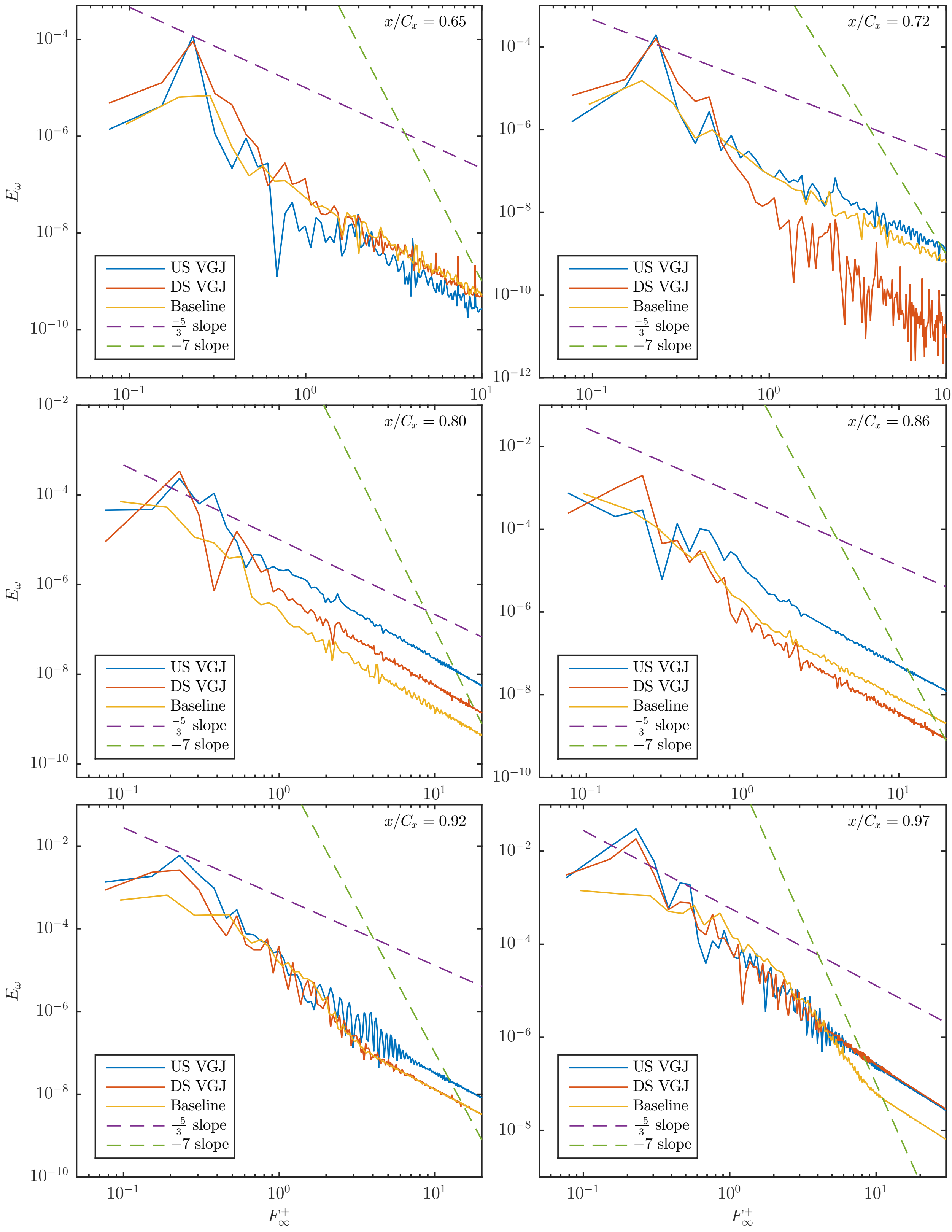

Figure 5.36: Turbulent Kinetic Energy frequency spectra at six streamwise stations, comparing US VGJ, DS VGJ, and baseline for jet with $F^+ = 3.02$ and $BR = 0.5$

high frequency, low blowing ratio case there were no large benefits to moving the VGJ upstream, but there was a modest increase in the unsteadiness present in the separated shear layer. The better performing US VGJ showed reattachment and a redeveloping boundary layer at the trailing edge of the blade.

For the DS VGJs flow control increased as the jet frequency was decreased which is an unexpected behavior. As discussed in Bons et al. (2002) and Volino et al. (2009), it is the starting and stopping of the jets which contribute largely to separation control. Typically, this fact coupled with higher jet frequencies prevents the relaxation of the separation bubble between jet pulses. Perhaps the combination of the low duty cycle (10%), high frequency, and jet placement inside the separation bubble all contributed to a low effectiveness at the highest frequency cases. The low duty cycle and high frequency will result in a smaller amount of time in which the jet is active during each jet pulse. Additionally, the jet location in the separated flow region could reduce the effectiveness of the start/stop vortex; hence, the steady blowing of the jet would be a larger driver of effective separation control. If the high jet frequency start/stop vortex was not effective; the jet duration was not long enough to control separation in each jet-cycle, so the benefit of the high frequency was never realized since it never produced adequate separation control even when active. In opposition, the low-frequency cases would produce a longer jet duration while the jet was active but allow more time to pass between jet pulses. This longer duration could have meaningfully reduced separation while active, hence the superior performance exhibited in this study, but allowed too much time to pass in-between jet pulses to provide a substantial decrease in separation characteristics. The US VGJs show that the low-frequency case VGJ again has promising flow control characteristics. Moving the VGJ upstream out of the separated flow region drastically increases the effectiveness of this jet. The high-frequency case still suffers which suggests that the placement upstream out of the separated flow region had little impact on the effectiveness of this VGJ. While this suggests that other factors such as the low duty cycle and high frequency somehow resulted in the ineffectiveness of the high-frequency jets in the DS and US configurations, a conclusive statement cannot be made since only one, low blowing ratio was simulated. Other jets with blowing ratios matching those of the low-frequency jets should also be simulated at these upstream locations to determine more accurately which parameter leads to the ineffectiveness of the high-frequency jets.

Given that the low-frequency cases were more effective, the highest blowing ratio for the low jet frequency, Case 4, provided the most effective control of separation for the DS VGJ simulations. Moving this jet upstream of the separation location also provided a substantial increase in its flow control abilities. The effectiveness of both DS and US, Case 4 VGJs is indicated by a rapid decrease in the C_p profile indicating transition, reduction in wake loss, smaller separation bubble in blade normal velocity profiles, redevelopment of the boundary layer near blade trailing edge (US VGJ), and location of peak fluctuating velocity closer to the blade surface. Viewing the turbulent kinetic energy frequency spectrum for Case 4, in Fig. 5.35 for both US and DS implementations at the streamwise stations just after the jet, there were peaks at the jet frequency and harmonics corresponding to this. This suggests that the vortices formed from the jets were more coherent than in the other cases simulated. Moving the jet upstream also increased the amount of power present in the jet frequencies of the turbulent kinetic energy frequency spectrum. Conversely, the higher jet frequency cases seemed to transfer energy into lower frequency harmonics. Perhaps the higher frequency cases were ineffective because the “effective” jet frequency was lower than that implemented at the actual jet hole. The blowing ratio of Case 4 was set at $BR = 3.0$, but a higher blowing ratio could provide more beneficial flow control.

In order to produce the most effective and optimal jets, it is beneficial to enact jet control closer to the natural separation point. In this study the location of the

DS VGJs was selected based on the attached C_p profile shown in Fig. 5.1, giving a VGJ location of $x/C_x = 0.60$. Based on L2A baseline flow tangent velocities at the blade surface, shown in Fig. 5.23, separation occurred in this study somewhere between $x/C_x = 0.55$ and 0.56. When viewing the attached C_p profile of Fig. 5.1 one can see that the pressure profile is somewhat flat from $x/C_x \approx 0.50 \rightarrow 0.60$. This is in contrast to the C_p profile of the L1A blade seen in Fig. 4.1 where there is a more distinctive peak in C_p. For the L2A blade, the flat profile indicates a section where the favorable pressure gradient is not very strong. This can allow the adverse pressure gradient on the aft portion of the blade to move the separation point upstream until it reaches a stronger favorable pressure gradient; therefore, the natural point of separation moves upstream of the peak suction location. A study of varying Reynolds numbers recording separation point of the L2A is warranted to investigate this point of natural separation.

The results of the US VGJ simulations show a definite increase in flow control effectiveness for the $BR = 3.0$ and $F^+ = 0.756$ VGJ (Case 4). This indicates a strong sensitivity of flow control to the point of separation. This is in contrast to the research conducted by Sondergaard et al. (2002) which showed that the VGJ effectiveness was relatively insensitive to the exact separation location as long as the VGJ was within the vicinity of the separation location. However, this study was conducted at $Re_{in} = 25,000$ with $FSTI = 1\%$ on the Pack-B turbine blade. The current study was conducted with a lower Re_{in}, no FSTI, and a more aggressive blade shape. This combination of factors seems to have caused the VGJ to be more sensitive to the separation location. More study is warranted to investigate the VGJs sensitivity to the point of separation.

5.7 Large Blowing Ratio

A follow on study to those conducted in Sections 5.4 and 5.5 was conducted to investigate the effects of a large increase in the VGJ blowing ratio. Typically, higher blowing ratios provide a greater degree of control with diminishing returns past a certain value. This section will discuss an additional simulation which took the US VGJ with $BR = 3.0$ and $F^+ = 0.756$, then only changed the BR, increasing it to 8.0. The hypothesis is that this large increase in BR will provide near complete separation control and indicate the limits of control using this particular VGJ configuration (i.e., DC, F^+, streamwise location, etc.).

The mesh and simulation times used here are identical to that used in Section 5.5 for the Case 4 US VGJ. The next several sections will present these results comparing the Case 4 US VGJ with an identical jet configuration except the BR was increased from 3.0 to 8.0. Comparisons will also show the baseline flow case for reference. Results will be briefly discussed and identify potential separation mitigation.

5.7.1 Coefficient of Pressure

Coefficient of pressure results are shown in Fig. 5.37. Using the baseline as a reference the $BR = 3.0$ VGJ provides an appreciable increase in peak suction and moves this suction peak downstream closer to the attached C_p profile location of peak suction at $x/C_x = 0.60$. Further increasing the BR to 8.0 increases the peak suction compared with the $BR = 3.0$ VGJ and moves the suction peak further downstream. There is a small spike in the C_p profile around $x/C_x = 0.53$. This abrupt increase in C_p is attributable to the very high jet velocity associated with the high blowing ratio which causes a local decrease in pressure. Further downstream the higher blowing ratio case shows a clear, rapid decrease in C_p. This signals large potential for reattachment for this VGJ case. The pressure surface behavior is very similar between all three cases but unexpectedly the $BR = 8.0$ case matches baseline results over a greater span of the pressure surface. These C_p results show a definite improvement in separation characteristics as given by the increase in peak suction and its movement downstream, approaching the behavior of the attached-flow C_p profile.

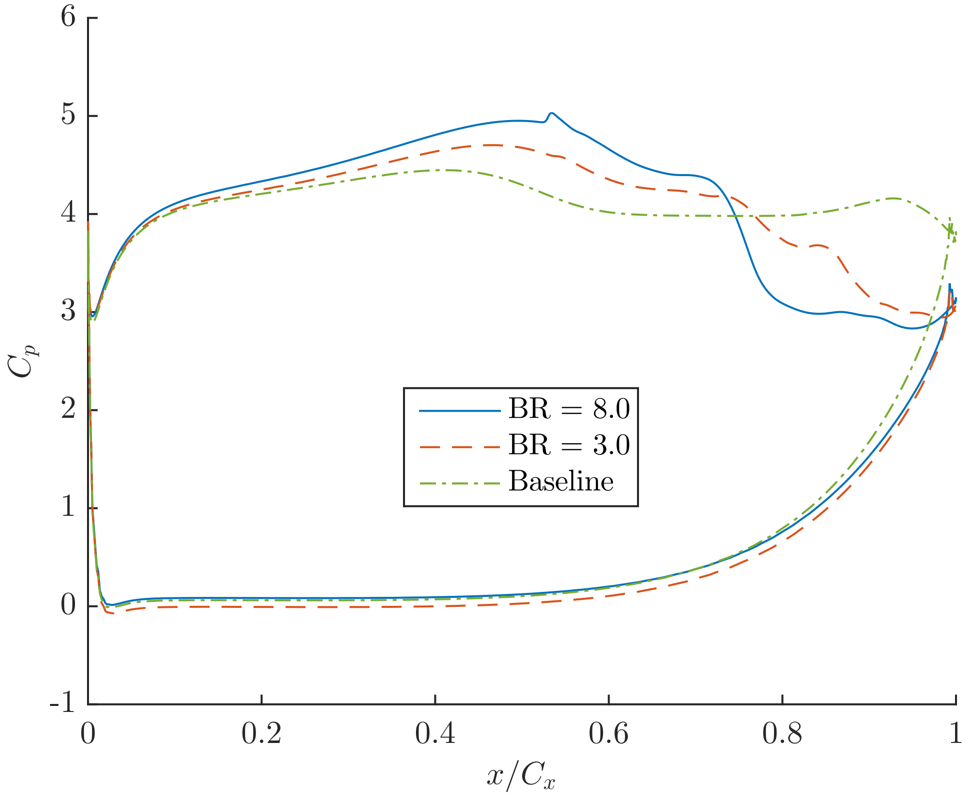

Figure 5.37: C_p surface distribution comparison for jet with $F^+ = 0.756$ located US at $x/C_x = 0.53$

5.7.2 Wake Loss

Wake loss results are shown in Fig. 5.38. Results were obtained in a plane perpendicular to the axial direction of the turbine passage at $x/C_x = 1.05$. Approaching the blade from the pressure side of the blade the two BR cases exhibit very similar behavior. The higher BR shows a larger peak value of wake loss which could indicate a greater degree of mixing occurring in the separated flow region. However, the higher

BR VGJ shows a narrower wake loss region indicating a smaller size of the separated region. Outside of the wake influence of the separated flow region the $BR = 8.0$ VGJ matches the results of the baseline case more so than the $BR = 3.0$ VGJ. Matching the baseline results outside of the separated flow region is the same behavior that was occurring with the blades pressure surface C_p results. Most importantly, the $BR = 8.0$ case increases the control of the separated region as shown by the narrower wake region.

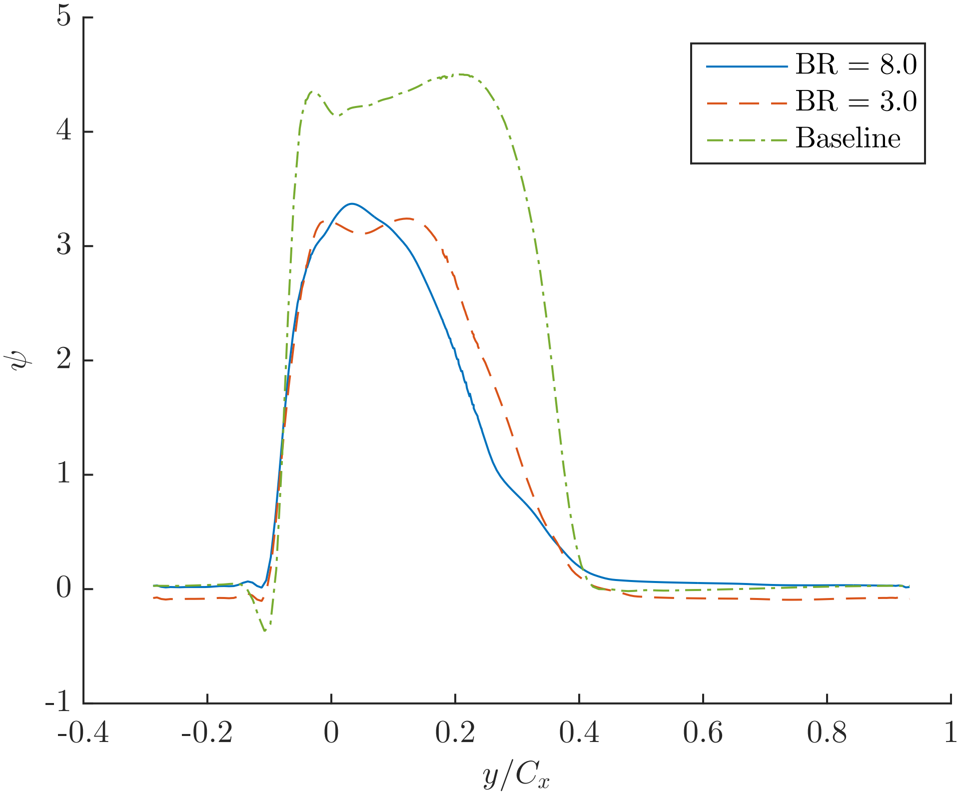

Figure 5.38: Wake Loss at $x/C_x = 1.05$ for jet with $F^+ = 0.756$ located US at $x/C_x = 0.53$

Normalized integrated wake loss results are shown in Fig. 5.39. These results show the normalized integrated wake loss for all 12 simulations from Section 5.4 compared with the US VGJ with $BR = 3.0$ and 8.0. The integrated wake loss values for the low and high BR VGJs are very similar providing a 42.1% and 42.8% reduction in wake loss over the baseline case, respectively. Therefore, the higher BR VGJ has a slight advantage over the lower BR VGJ.

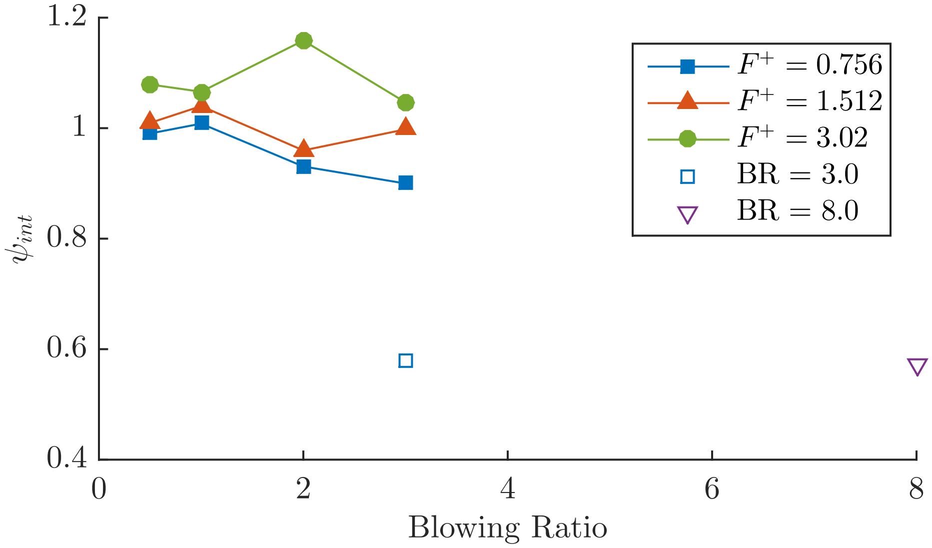

Figure 5.39: Integrated Wake Loss normalized by baseline compared for all 12 DS VGJs with two US VGJs with $F^+ = 0.756$ and $BR = 3.0$ and 8.0

5.7.3 Blade Normal Velocity Magnitude

Blade normal velocity magnitude profiles are shown in Fig. 5.40. The extent of the separated flow region is clearly reduced for the higher BR VGJ as can be seen at streamwise locations: $x/C_x = 0.65$, 0.72, and 0.80. The three downstream locations show more similar behavior between the two BR VGJs. The next section provides tangent velocity profiles allowing the visualization of reverse flow regions and is more telling of the benefits of the higher BR.

5.7.4 Blade Normal Tangent Velocity

Blade normal tangent velocity profiles are shown in Fig. 5.41. At station $x/C_x = 0.58$ the $BR = 8.0$ VGJ case shows a slight improvement with the boundary layer closer to the blade surface. At $x/C_x = 0.65$ both VGJ cases seem to have very little velocity

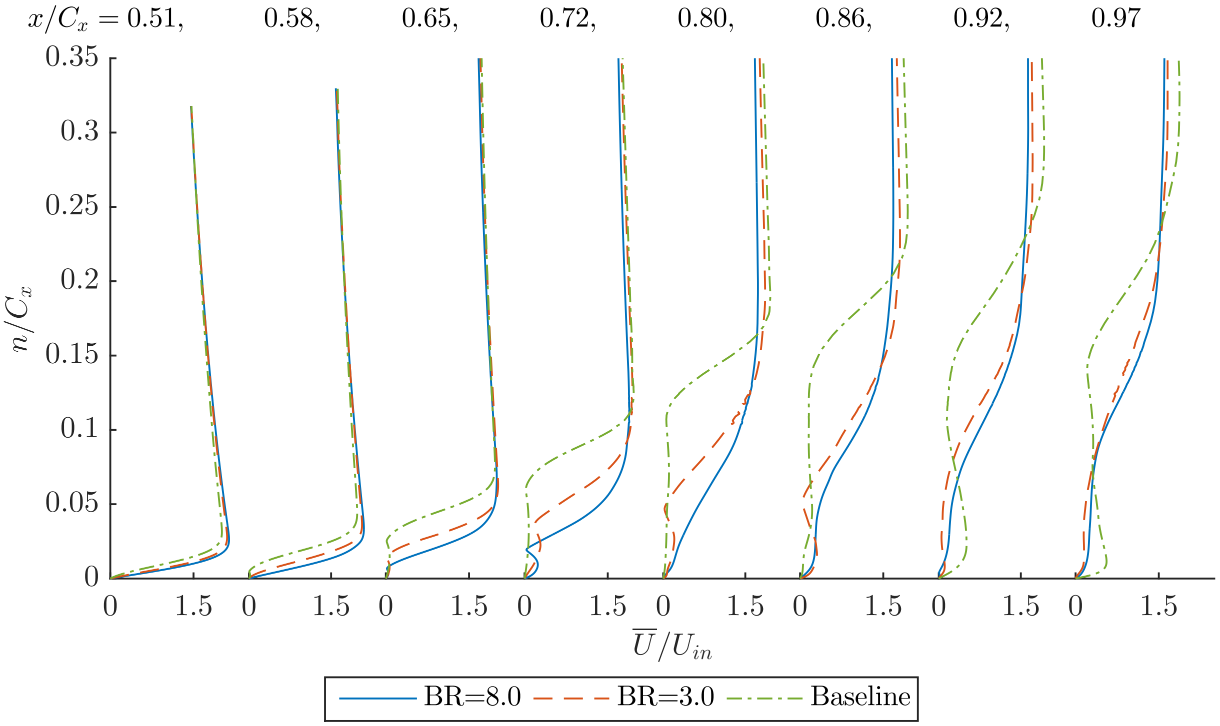

Figure 5.40: Time-averaged blade normal velocity magnitude profiles, comparing jets with $BR = 3.0$ and 8.0, $F^+ = 0.756$, and baseline flow case

change close to the blade suggesting that separation is about to occur in both cases. At $x/C_x = 0.72$ both VGJ cases show a reverse flow region indicating that they are both separated, however, the $BR = 8.0$ case shows a much smaller separated and reverse flow region definitely indicating a larger degree of control. The most telling result is at $x/C_x = 0.80$ where the higher BR case no longer contains any reverse flow indicating reattachment. This is in contrast to the lower $BR = 3.0$ case which doesn't reattach until $x/C_x = 0.92$. Further downstream the higher $BR = 8.0$ case never redevelops a significant velocity gradient close to the blade, indicative of a redeveloped boundary layer, but results do show that the separated region has been nearly eliminated.

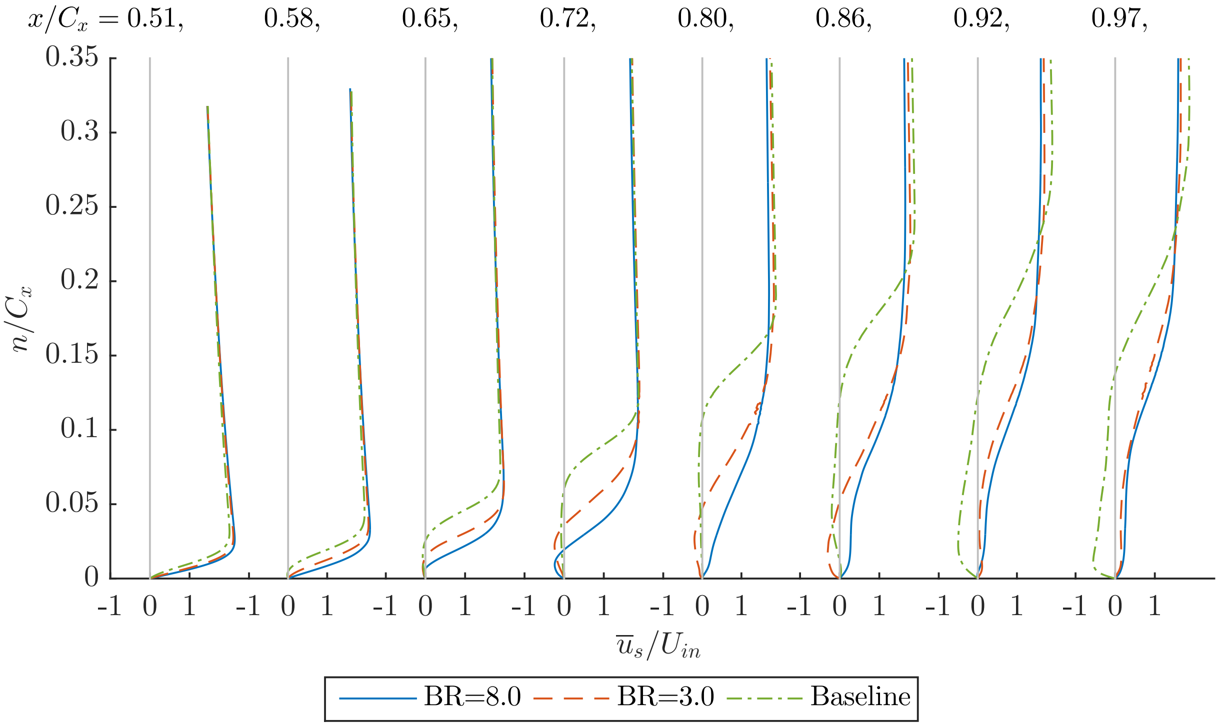

Figure 5.41: Time-averaged blade normal, tangent velocity profiles, comparing jets with $BR = 3.0$ and 8.0, $F^+ = 0.756$, and baseline flow case

5.7.5 Blade Normal RMS Fluctuating Velocity Magnitude

Fluctuating velocity magnitude values normal to the blade surface are shown in Fig. 5.42. These results show that the higher BR case contains a higher degree of unsteadiness at the stations: $x/C_x = 0.58$, 0.65, and 0.72. The larger BR creates a stronger VGJ which in turn provides a higher degree of unsteadiness in the boundary layer and separated flow region. This higher unsteadiness helps to transfer momentum into the separated flow region promoting flow reattachment, as seen in Fig. 5.41 for the higher BR case.

5.7.6 Near Jet Vortical Structures

The dramatic improvement in separation characteristics given by the $BR = 8.0$ VGJ warrants further investigation into the jet physics that are at work and how the formation of vorticies helps to prevent separation. In Figs. 5.43, 5.44, 5.45, and

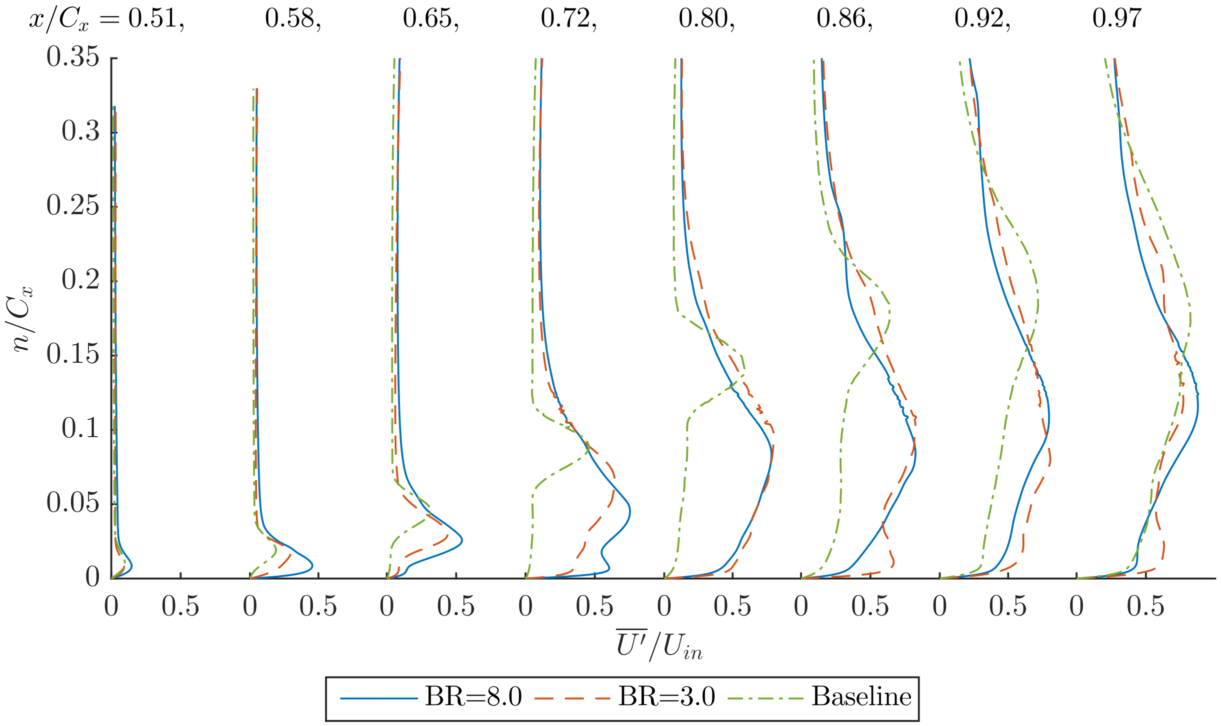

Figure 5.42: Time-averaged blade normal RMS fluctuating velocity magnitude profiles, comparing jets with $BR = 3.0$ and 8.0, $F^+ = 0.756$, and baseline flow case

5.46 eight cross-sectional planes are shown at various streamwise locations as labeled. These planes are normal to the turbine axial direction. That is, these planes are not normal to the blade surface. Each plane contains a colored contour of streamwise "X" vorticity with values indicated by the color legend in each image. These results are instantaneous flow results collected at 12 even intervals during a single VGJ pulse cycle. In the upper-right corner of each image is a quantity giving the time during the jet period (e.g., $t/T = 1/12$ is 1/12th of the jet period after the start of the pulsing cycle).

The first 3 results are shown in Fig. 5.43. The first image, at $t/T = 1/12$, is just after the VGJ has become active (and is still active at this point given 10% DC). At this first jet phase it is difficult to make out any singular vortical structures. At phase $t/T = 2/12$ the VGJs active phase has ended and so the plane closest to the jet at $x/C_x = 0.54$ shows very little streamwise vorticity as the VGJ's effects have convected downstream. At the $x/C_x = 0.565$ plane there is a large negative x-vorticity structure that has formed. This is a result of the stronger singular vortical structure typically produced by a VGJ as seen in Fig. 1.2. At phase $t/T = 3/12$ the strong negative vortical structure has moved further downstream to stations $x/C_x = 0.59\,\text{and}\,0.615$. The strength of the vortex is evident by its ability to penetrate downstream of the VGJ location.

Figure 5.44 shows the next 3 jet phases. As time progresses the large vorticity produced by the VGJ moves further downstream and away from the blade surface. The leading edge of this vortical structure convects downstream faster than the trailing edge of the same vortical structure. This results in the vortical structure stretching in the streamwise direction and increasing its streamwise span over the turbine blade surface. This will improve the ability of the streamwise vortex to entrain freestream momentum over a greater length of the blade suction surface, thus increasing separation mitigation. Also, the trailing edge of the main vortical structure remains close to the blade surface allowing momentum transfer into the regions most susceptible to flow separation. At the last phase, $t/T = 6/12$, we see the development of some counter rotating (positive x-vorticity) structures beginning to develop alongside the main vortical structure produced by the VGJ.

Figures 5.45 and 5.46 show the trailing edge of the main vortical structure moving downstream, albeit slowly. The counter-rotating vortex also becomes less elongated and forms a circular rotation region as can be seen in Fig. 5.46, $t/T = 10/12$, $x/C_x = 0.715$. Even at the last phase of the jet cycle ($t/T = 12/12$) the trailing edge of the vortical structure produced by the VGJ and the counter-rotating vortex are still present at $x/C_x = 0.715$. Thus the vortical structures produced by the VGJ only leave a small extent over the aft-suction surface where separation can re-form before the jet is pulsed again. The lingering vortical structures produced by the VGJ are a large part of why they remain effective even when turned “off.” Given a high enough VGJ pulse frequency, the jets can prevent the relaxation of the boundary layer between jet pulses.

5.7.7 Downstream Vorticity

Results for spanwise vorticity (z-vorticity) are shown in Fig. 5.47. These results show that the large BR produced large vortical structures that are then shed from the trailing edge of the blade. The spanwise vortical structures offer another perspective of the large degree of rotation produced by the VGJ which allows the mixing of high momentum freestream with the boundary layer to mitigate separation. These results also show the diffusion of the solution caused downstream of the blade. This is a result of the mesh stretching that was implemented downstream to prevent the reflection of pressure waves into the computational domain. This same technique was applied to the LPT problem by Rizzetta and Visbal (2005) and Poondru (2007).

5.7.8 Large Blowing Ratio Summary

The results in the previous sections show that increasing the BR from 3.0 to 8.0 did provide a great improvement in separation control. The original hypothesis was that separation could be nearly eliminated which was confirmed by the results shown. There is still a small degree of separation present, but the flow reattaches and provides an increase in the peak suction of the turbine blade.

Only one BR was simulated here in an attempt to find the limits of control given the other VGJ parameters. It would be informative to simulate other BRs approaching the value of 8.0 to ascertain if this case represents the limiting performance of the VGJ or if there is room for further improvement with higher BRs.

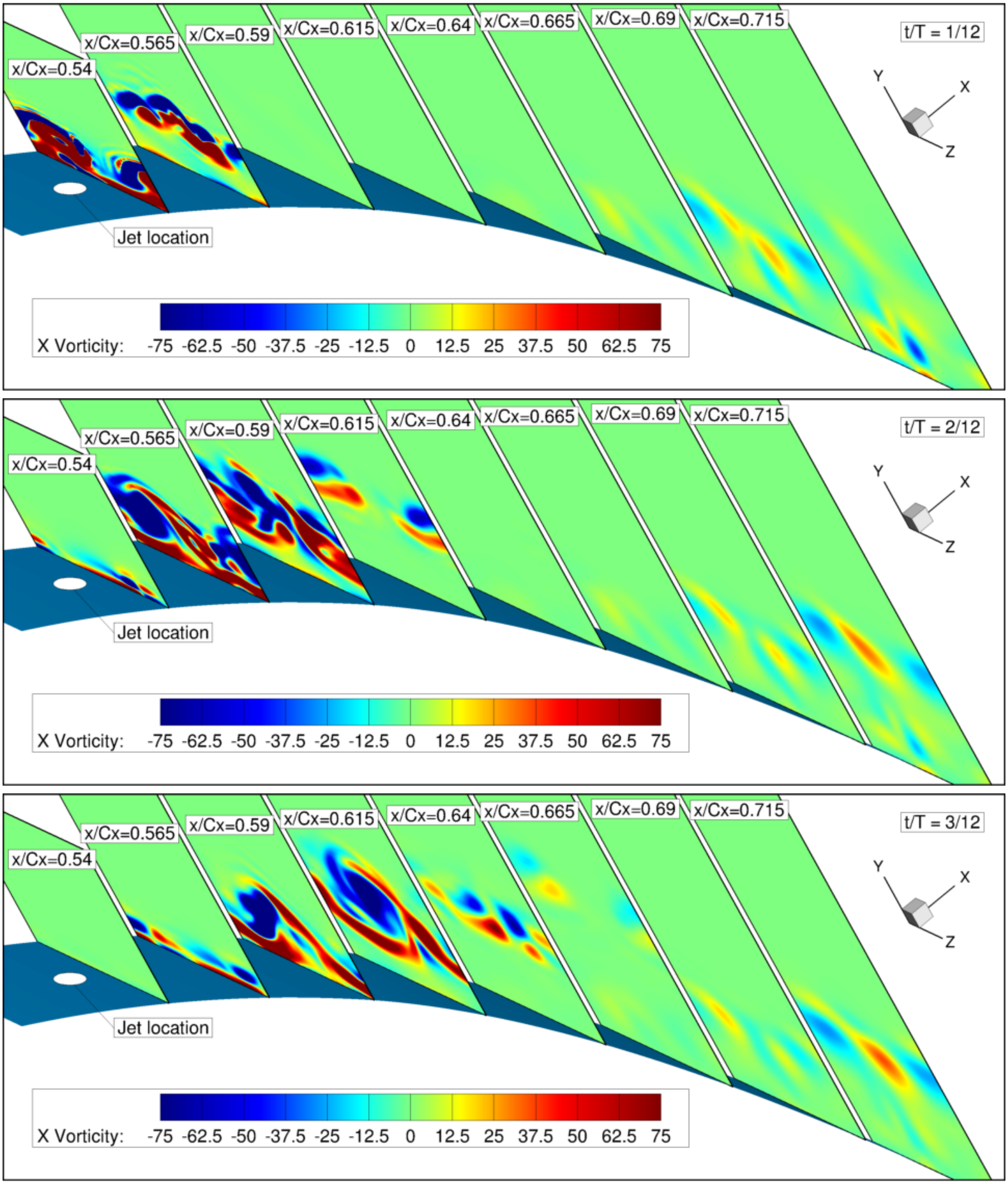

Figure 5.43: Instantaneous near-jet x-vorticity (jet phase: $t/T = 1/12,\ 2/12,\ 3/12$)

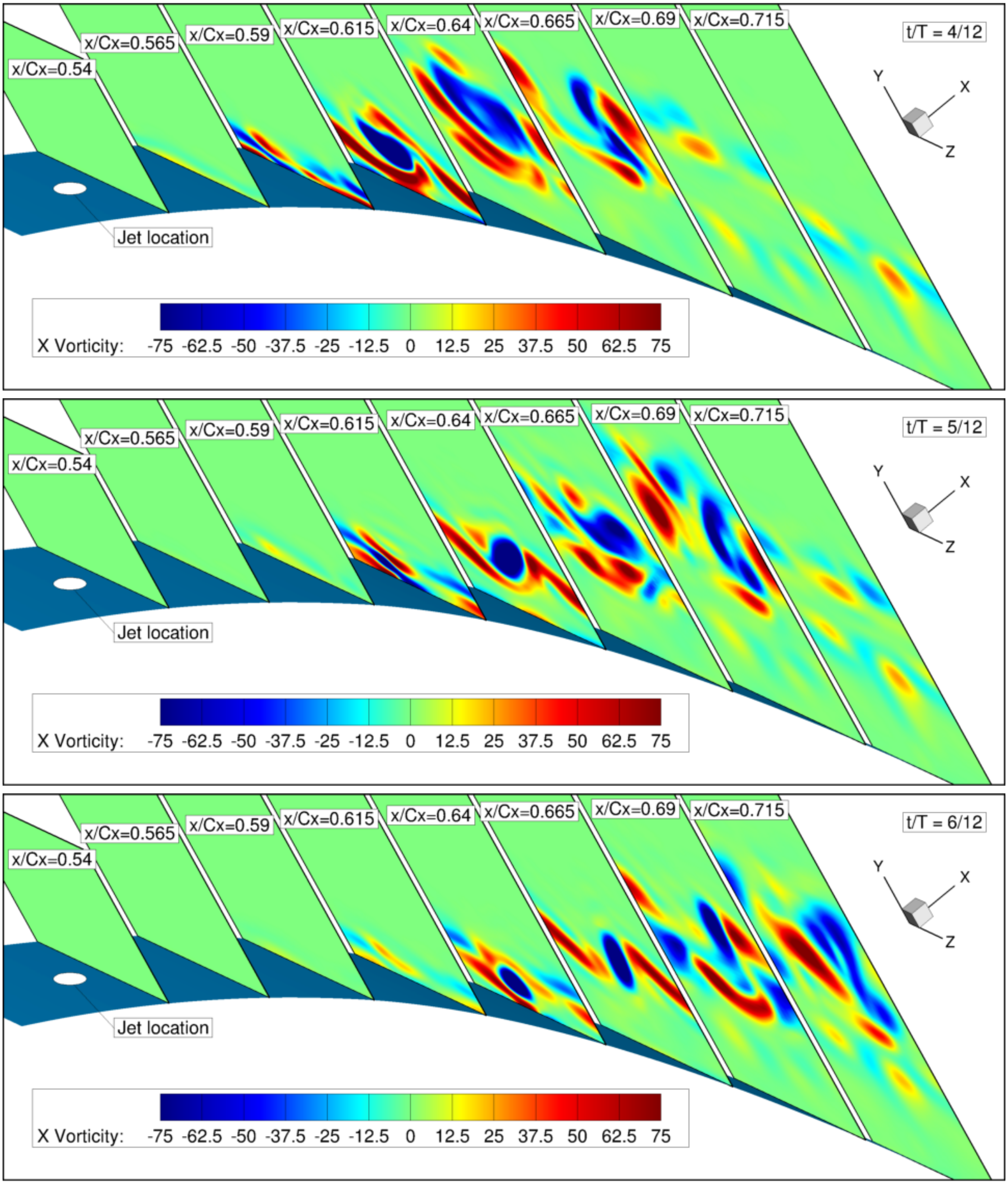

Figure 5.44: Instantaneous near-jet x-vorticity (jet phase: $t/T = 4/12$, $5/12$, $6/12$)

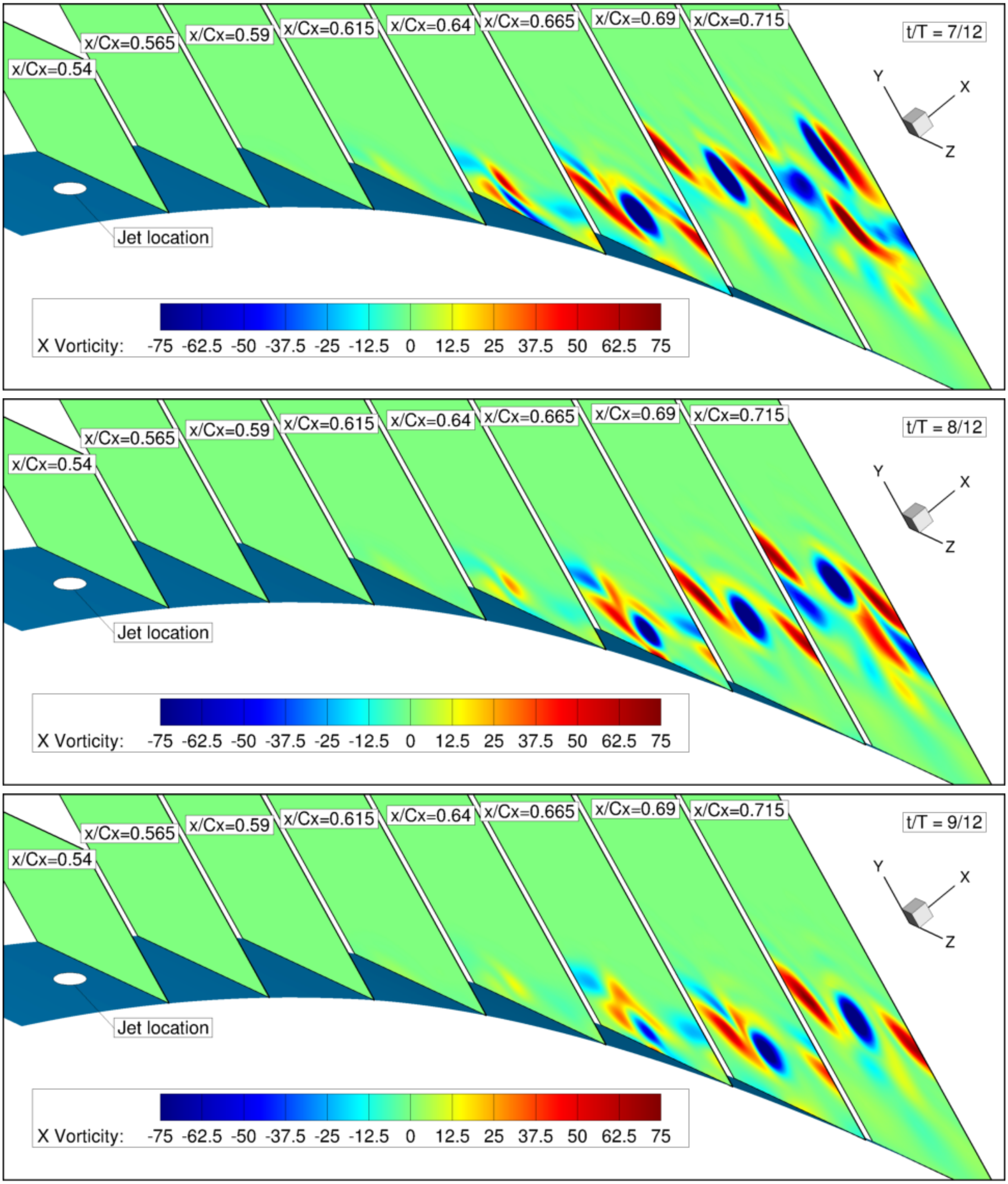

Figure 5.45: Instantaneous near-jet x-vorticity (jet phase: $t/T = 7/12$, $8/12$, $9/12$)

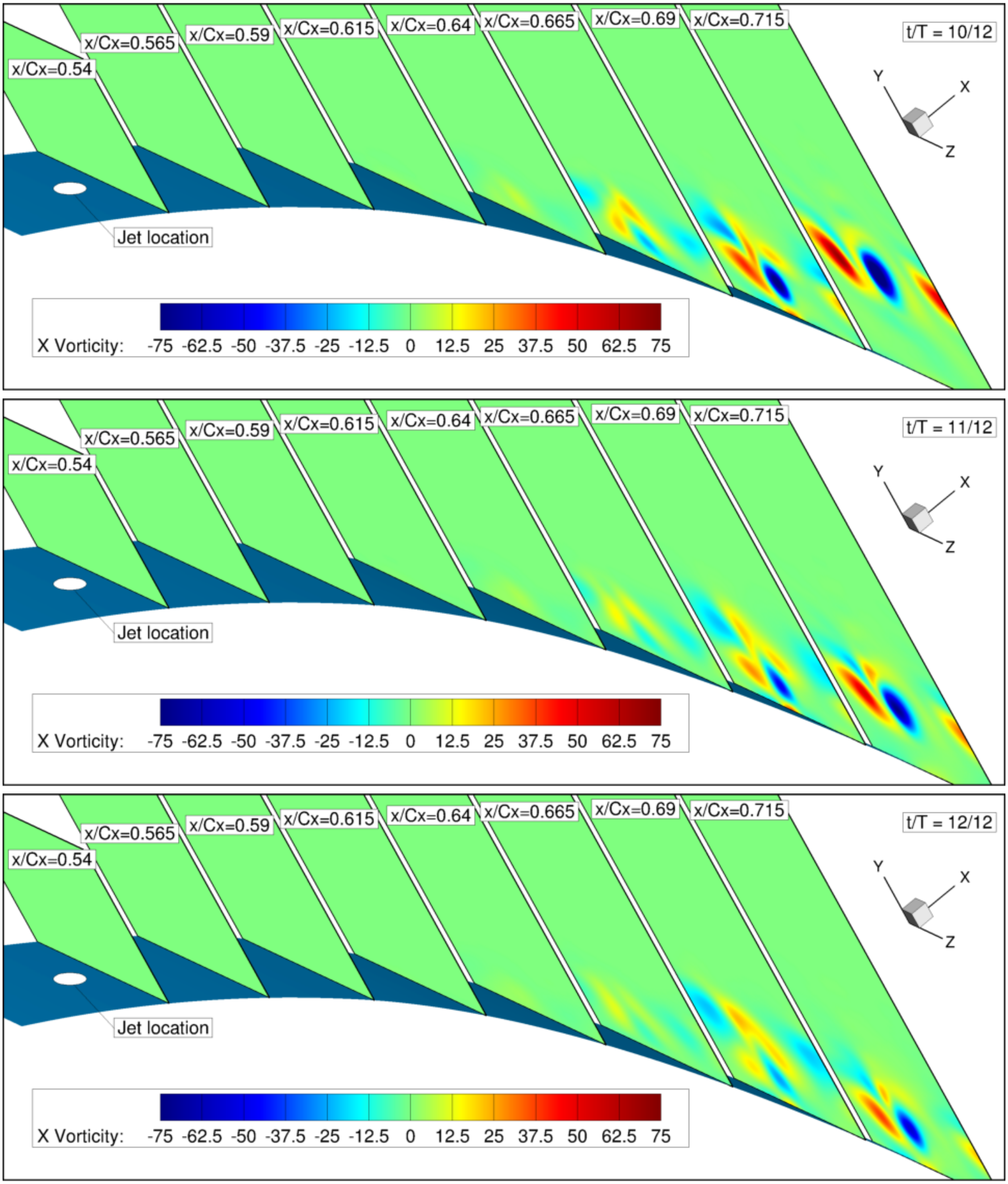

Figure 5.46: Instantaneous near-jet x-vorticity (jet phase: t/T = 10/12, 11/12, 12/12)

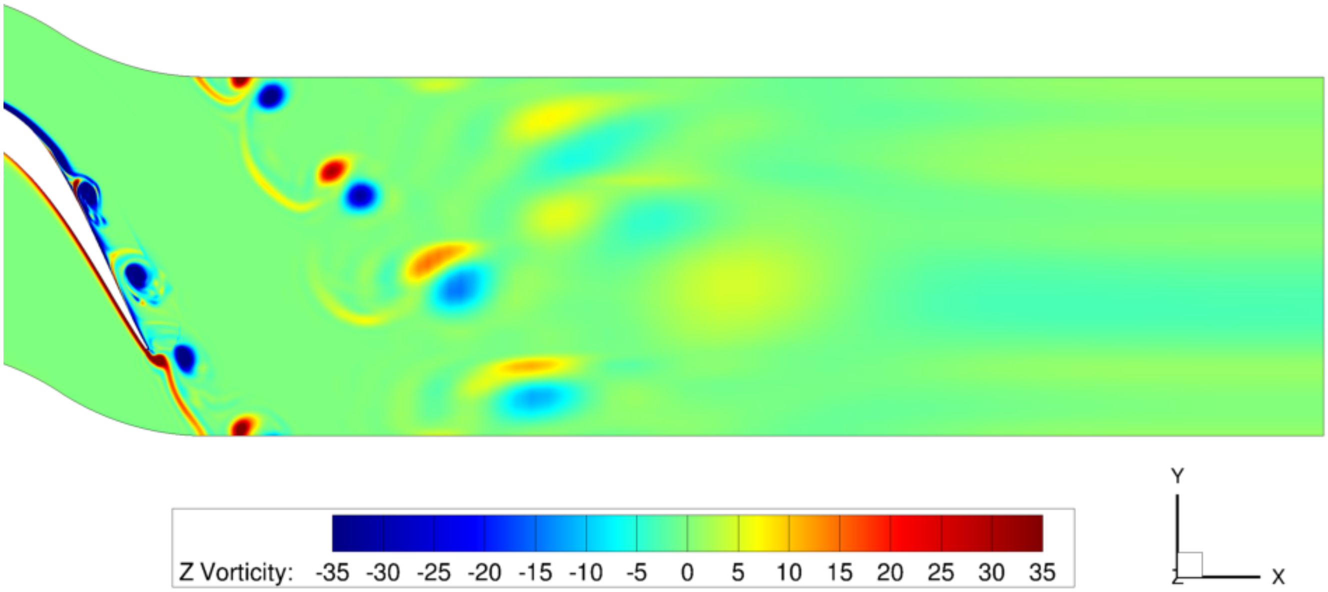

Figure 5.47: Instantaneous downstream z-vorticity

5.8 Chapter Summary

Low Reynolds number flow was simulated for the AFRL L2A blade. This blade was selected due to its aft-loaded characteristics which allow for the investigation of flow control strategies. Simulations were executed at a low Reynolds number, $Re_{in} = 10,000$, which causes a large degree of separation. The configuration of the jets was selected based on the setup used in Volino et al. (2009) and Volino et al. (2011) as these configurations covered the spectrum of no control to very successful flow control. Twelve jet configurations were considered. Two simulations were conducted moving two of these VGJ configurations upstream of the separation location. Computational grids were constructed in a very similar manner to the L1A blade meshes used in the simulations of Chapter 4.

Overall, the results of the simulations show that none of the DS VGJ configurations simulated provided a great degree of separation control. Moving the best performing DS VGJ configuration to a location upstream of separation provided a dramatic increase in flow control effectiveness even causing reattachment of the separation bubble near the blade trailing edge. Additionally, the most controlled cases were not those expected to be effective. It was predicted that the high jet frequency cases would be the most effective, but results indicated the opposite with the lowest jet frequency cases combined with high blowing ratio being the most effective. The reason for this unexpected behavior is discussed as a possible result of the low duty cycle simulated, and the fact that the jets were located inside the separated flow region. One US VGJ configuration with high frequency was investigated but only for one low blowing ratio which did not provide enough evidence to determine if the high-frequency jets would still be ineffective if moved upstream of the separation location. Also, the natural point of separation in the baseline case did not occur where expected when selecting the DS VGJ locations. This caused the DS jets to be positioned in a non-optimal setting and the separation control suffered because of this fact. Further studies on the location of natural separation, the sensitivity of VGJ streamwise location, varying duty cycle, and even more aggressive jet configurations (higher blowing ratio) are warranted.

One additional study at a high blowing ratio was conducted which showed improved performance with reattachment well upstream of the blade trailing edge, resulting in a very small separation bubble. More blowing ratios should be investigated to determine if this result is a limiting behavior or if even higher BR would provide more improvements.

Chapter 6

Conclusions

6.1 Conclusions

The low-Reynolds number, massively separated flow through a low-pressure turbine (LPT) cascade was studied numerically using the implicit large eddy simulation (ILES) technique of Rizzetta and Visbal (2005). This ILES technique was used in conjunction with high-order compact schemes for spatial derivatives and Padé-type low-pass filtering to remove poorly resolved wave numbers for implementing dissipation instead of the typical sub-grid-scale (SGS) models. This methodology solves the unfiltered Navier-Stokes equations which allow for a seamless transition between different flow regions and allows for a comprehensive flow solving technique capable of predicting separation and reattachment points which are of the utmost importance in separated LPT flow investigations. These flow solving characteristics are incorporated in a higher-order, parallel, Chimera, ILES version of FDL3DI (Gaitonde and Visbal, 1998) which was utilized for the current application. All simulations were executed on dual-topology, multi-block, structured meshes. Flow simulations were executed for the Air Force Research Laboratory (AFRL) L1A blade for comparisons with available experimental data and flow solver verification in the current study.

These simulations considered flow at $Re_{in} = 10,000$ with two jet configurations corresponding to poor and significant separation control. Following was the main thrust of the study conducting flow simulations for the AFRL L2A blade simulating twelve jet configurations at a single streamwise location, two other simulations moving two of these configurations to upstream positions, and a final simulation taking the best performing configuration and increasing the blowing ratio. All of these flow control simulations were compared with a non-controlled flow case ascertaining optimal jet parameters.

6.1.1 L1A Validation Study

Numerical simulations were executed using the L1A blade and select jet configurations present in the experimental studies of Volino et al. (2009, 2011). These simulations were executed at the lowest Re available in the studies ($Re_{in} = 10,000$) which provided the greatest amount of separation. Two cases were considered corresponding to a poorly and successfully controlled separated flow. For these simulations, three different sized meshes were used for a grid-independence study and compared with the experimental results. Flow solutions were analyzed in terms of time-averaged surface coefficient of pressure, blade normal profiles of velocity magnitude and root-mean-square fluctuating velocity magnitude, iso-images of cross-flow vorticity, flow streamlines, and spanwise vorticity. Phase-averaged blade normal velocity magnitude profiles were also investigated. Simulations compared well in qualitative respect with the trends largely capturing what occurred in the experiments. However, the quantitative values did not compare as well and are likely a direct result of differences between the experimental and numerical setup. Specifically, the simulations did not account for wind tunnel walls, which help turn the flow and induce secondary flow, and do not include freestream turbulence, which helps promote transition. Simulations indicated a larger degree of separation than experimental results. In comparing the two cases simulated, results show significantly reduced separation which is consistent with experimental results suggesting the flow physics of the VGJ were accurately captured. The poorly controlled case did not compare well between the different mesh sizes which is attributed to the highly unsteady flow in this separated flow case. The controlled case compared well between the mid-sized and refined mesh, providing the motivation for using the mesh sizes developed here in the flow control study.

6.1.2 L2A Flow Control

Active flow control was simulated for the L2A blade using jet parameters based on the experimental results examined in the L1A validation study. These simulations were conducted at a low inlet Re of $Re_{in} = 10,000$ with blowing ratios of 0.5, 1.0, 2.0, and 3.0. Cases were also simulated for three different jet frequencies: $F^+ = 0.756,\ 1.512, \text{and } 3.02$. This results in twelve different jet configurations simulated at a single streamwise location. Two additional simulations were conducted at an upstream location for two VGJ configurations ($BR = 3.0$, $F^+ = 0.756$ and $BR = 0.5$, $F^+ = 3.02$). A final simulation was executed with the low-frequency, upstream VGJ configuration increasing its blowing ratio ($BR = 8.0$, $F^+ = 0.756$). The meshing technique was based on the results of the L1A validation study. Results were presented for the coefficient of pressure, wake loss profiles, blade normal velocity magnitude, blade normal tangent velocity, blade normal root-mean-square velocity magnitudes, and turbulent kinetic energy frequency spectra in order to assess the efficacy of the jets. The best performing VGJ also displayed streamwise vorticity contours and downstream spanwise vorticity to investigate jet physics.

Results for the DS VGJs did not turn out as predicted with none of the cases simulated presenting a large degree of separation control. There was a small degree of separation control which unexpectedly was reduced as the jet frequency increased. The placement of the jets was based on a likely optimal location based on past research but ultimately resulted in the jet placement in the separated flow region. It was concluded that the combination of low duty cycle, low jet active time (high frequency), and location in the separation bubble in combination contributed to the ineffectiveness of the higher jet frequencies. The case providing the most effective separation control was at $BR = 3.0$ and $F^{+} = 0.756$ which resulted in the jet frequency and multiple harmonics being present in the turbulent kinetic energy frequency spectra. The presence of the jet frequency and multiple harmonics suggest that the vortical structures resulting from the VGJ were highly active in the flow just downstream of the VGJ. Higher frequency jets seemed to redistribute their frequency content into lower frequencies possible reducing the "effective" jet frequency experienced by the separated flow.

Due to the ineffectiveness of these DS VGJs, two other simulations were conducted taking the best and worst performing cases of the twelve jet configurations discussed above and moving them upstream of the separation location. The best performing DS VGJ was configured at $BR = 3.0$ and $F^{+} = 0.756$ (Case 4) while the worst performing case was at $BR = 0.5$ and $F^{+} = 3.02$ (Case 9). The Case 4 VGJ drastically improved its separation control when moved upstream while the Case 9 VGJ showed very little change. This shows that the ability to control separation is sensitive to the relative location of the VGJ and the separation location. The high frequency, Case 9, VGJ's ineffectiveness even at the upstream location suggests that another jet parameter caused the high-frequency jets to perform poorly in the current study. However, this jet had a very low BR and may have performed much better if configured with a large BR.

One final simulation was conducted to find the potential limits of flow control with the VGJs used in the current study. The best performing upstream VGJ ($BR = 3.0$ and $F^{+} = 0.756$) was configured the same way except that the blowing ratio was increased to $BR = 8.0$. This large increase did provide an improvement in separation control and nearly eliminated separation on the turbine blade. There was a small region of separated flow that remained but flow reattached after this separation bubble. Only a single large blowing ratio was simulated so it is difficult to determine if this was a limiting behavior or if an even larger blowing ratio would provide further improvements.

6.2 Recommendations for Future Work

The work conducted in this study resulted in a reduction in jet efficacy due to the sub-optimal location of the DS VGJs. A limited study was conducted moving select VGJ configurations upstream which showed a drastic improvement for one of the configurations. Additional study did show that further improvements can be obtained with large increases to VGJ blowing ratio. These facts along with other results contained in this study provide the motivation for the following list of recommended future work concerning LPT cascades:

- Simulations and experimental studies should be conducted to find the natural separation point of the L2A blade at various Re values. The plateau in the attached C_p profile likely will cause variations in the location of flow separation.
- Jet configurations in the current study should be investigated at various points upstream of the separation point to assess the sensitivity of the VGJ streamwise placement.
- Given the low effectiveness of high-frequency VGJs in this study, additional work can be done to investigate why these cases were ineffective. A more comprehensive study can be conducted with jets placed upstream of separation to eliminate this potential source of jet ineffectiveness. Also, other duty cycles can be investigated to understand the effect on VGJ efficacy and if this has any bearing on the effectiveness of high-frequency jets.

- A high blowing ratio was simulated in this study but given the single simulation it is difficult to determine if its ability to mitigate separation was a limiting behavior or if further improvement could be obtained with more aggressive jets. Therefore, multiple large blowing ratios should be simulated to identify the point of diminishing returns.

- VGJ pitch and skew angles were fixed in this study based on past research but it would be of interest to conduct an LPT simulation comparing various jet flow angles.

- In the literature most control setups only include the use of a single spanwise row of jets for control. This motivation is a result of the core understanding that separation control is largely a result of flow transition which only occurs once. Perhaps the presence of jet harmonics in the turbulent kinetic energy spectra can excite natural modes of the flow which could be accomplished with multiple jet rows. It would be an interesting study to pursue.

- The end-wall effects have been mentioned as being important sources of secondary losses which drastically reduce the effectiveness of front-loaded blade designs. Mid-span flow control simulations should be combined with means of controlling flow at the end-walls to get a more comprehensive picture of blade performance.

Additional recommendations pertain to the flow solver, FDL3DI, that was used in this study. These recommendations seek to address differences between the numerical and experimental setups as witnessed in this study.

- The solver needs to include the ability to simulate freestream turbulence. This can contribute to the natural separation location and the flow's propensity for the transition.

- The options for boundary spatial discretizations are shown in Table 2.3. There has not been an exhaustive study comparing these options resulting in choices being made on historical use. These should be evaluated for their use in the LPT problems.

6.3 Significance of Research

This study provided the first set of numerical results for the L2A turbine blade of which the the author is aware. Additionally, it was the first attempt of incorporating flow control for this blade. The conclusions of this study are important for the future development of these "high-lift" blades and contribute to the literature regarding flow control for LPTs in general. Understanding the aerodynamics of these flows and how flow control can benefit them is important in further increasing the efficiency of modern gas turbine engines. This industry has made great advancements in the 20th century which have greatly affected the lives of everyone. The 21st century seems a promising place to continue these efforts.

Bibliography

Abu-Ghannam, B. J. and R. Shaw, (1980) “Natural Transition of Boundary Layers - The Effects of Turbulence, Pressure Gradient, and Flow History,” *IMechE Journal of Mechanical Engineering Science*, Vol. 22, No. 5, pp. 213–228.

Baldwin, B. S. and H. Lomax, (1978) “Thin Layer Approximation and Algebraic Model for Separated Turbulent Flow,” In *16th Aerospace Sciences Meeting*, Paper No. AIAA 1978-257.

Beam, R. and R. Warming, (1978) “An Implicit Factored Scheme for the Compressible Navier-Stokes Equations,” *AIAA Journal*, Vol. 16, No. 4, pp. 393–402.

Benek, J. A., J. L. Steger, F. C. Dougherty and P. G. Buning, (1986) “Chimera: A Grid-Embedding Technique,” Arnold Engineering Development Center, Technical Report: AEDC-TR-85-64.

Benek, J. A., J. Steger and F. C. Dougherty, (1983) “A Flexible Grid Embedding Technique with Application to the Euler Equations,” In *6th Computational Fluid Dynamics Conference Danvers*, Paper No. AIAA 83-1944.

Bohl, D. and R. Volino, (2006) “Experiments With Three-Dimensional Passive Flow Control Devices on Low-Pressure Turbine Airfoils,” *ASME Journal of Turbomachinery*, Vol. 128, pp. 251–260.

Bons, J., J. Pluim, K. Gompertz, M. Bloxham and J. Clark, (2008) “The Application of Flow Control to an Aft-Loaded Low Pressure Turbine Cascade with Unsteady Wakes," In *ASME Turbo Expo 2008: Power for Land, Sea and Air*, Paper No. GT2008-50864.

Bons, J., R. Sondergaard and R. Rivir, (1999) "Control of Low-Pressure Turbine Separation using Vortex Generator Jets," In *37th Aerospace Sciences Meeting and Exhibit*, Paper No. AIAA 99-0367.

Bons, J., R. Sondergaard and R. Rivir, (2001) "The Fluid Dynamics of LPT Blade Separation Control Using Pulsed Jets," In *Turbo Expo 2001: International Gas Turbine Conference*, Paper No. 2001-GT-0190.

Bons, J., R. Sondergaard and R. Rivir, (2002) "The Fluid Dynamics of LPT Blade Separation Control Using Pulsed Jets," *ASME Journal of Turbomachinery*, Vol. 124, pp. 77–85.

Chien, K. Y., (1982) "Predictions of Channel and Boundary-Layer Flows with a Low-Reynold's Number Turbulent Model," *AIAA Journal*, Vol. 20, No. 1, pp. 33–38.

Dorney, D. and D. Ashpis, (1998) "Study of Low Reynolds Number Effects on the Losses in Low-Pressure Turbine Blade Rows," In *34th Joint Propulsion Conference and Exhibit*, Paper No. AIAA-98-3575.

Gaitonde, D., J. Shang and J. Young, (1997) "Practical Aspects of High-Order Accurate Finite-Volume Schemes for Electromagnetics," In *35th AIAA Aerospace Sciences Meeting and Exhibit*, Paper No. AIAA 97-0363.

Gaitonde, D. and M. Visbal, (1998) "High-Order Schemes for Navier-Stokes Equations: Algorithm and Implementation into FDL3DI," Air Force Research Laboratory, Technical Report: AFRL-VA-WP-TR-1998-3060.

Gaitonde, D. and M. Visbal, (2000) "Pade-Type Higher-Order Boundary Filters for the Navier-Stokes Equations," *AIAA Journal*, Vol. 38, No. 11, pp. 2103–2112.

Galbraith, M., (2009) "Implicit Large Eddy Simulation of Low-Reynolds-Number Transitional Flow Past the SD7003 Airfoil," Master's Thesis, University of Cincinnati, Cincinnati, OH.

Gomez, R. J., D. Vicker, S. E. Rogers, M. J. Aftosmis, W. M. Chan, R. Meakin and S. Murman, (2004) "STS-107 Investigation Ascent CFD Support," Paper No. AIAA 2004-2226.

Gordnier, R., (1995) "Computation of Delta-Wing Roll Maneuvers," *Journal of Aircraft*, Vol. 32, No. 3, pp. 486–492.

Gordnier, R. and M. Visbal, (1998) "Numerical Simulation of Delta-Wing Roll," *Aerospace Science and Technology*, Vol. 2, No. 6, pp. 347–357.

Gross, A. and H. Fasel, (2007) "Investigation of Low-Pressure Turbine Separation Control," In *45th AIAA Aerospace Sciences Meeting and Exhibit*, Paper No. AIAA 2007-520.

Gross, A. and H. Fasel, (2008) "Strategies for Simulating Flow Through Low-Pressure Turbine Cascade," *ASME Journal of Fluids Engineering*, Vol. 130, pp. 111105–1 – 111105–13.

Halstead, D.E., D.C. Wisler, T.H. Okiishi, G.J. Walker, H.P. Hodson and H.W. Shin, (1997) "Boundary Layer Development in Axial Compressors and Turbines Part 1 of 4: Composite Picture," *Journal of Turbomachinery*, Vol. 119, pp. 114–127.

Horton, H. P., (1968) "Laminar Separation Bubbles in Two and Three Dimensional Incompressible Flow," PhD Thesis, Queen Mary College, London, England.

Howell, R.J., H.P. Hodson, V. Schulte, R.D. Stieger, H. Schiffer, F. Haselbach and N.W. Harvery, (2002) "Boundary Layer Development in the BR710 and BR715 LP Turbines-The Implementation of High-Lift and Ultra-High-Lift Concepts," *Journal of Turbomachinery*, Vol. 124, pp. 385–392.

Huang, J., T. Corke and F. Thomas, (2003) "Plasma Actuators for Separation Control of Low Pressure Turbine Blades," In *41st Aerospace Sciences Meeting and Exhibit*, Paper No. AIAA 2003-1027.

Hung, Ching-mao, (2002) "Definition of Contravariant Velocity Components," In *AIAA 3rd Theoretical Fluid Mechanics Meeting*, Paper No. AIAA 2002-3202.

Jameson, A., S. Wolfgang and E. Turkel, (1981) "Numerical Solution of the Euler Equations by Finite Volume Methods Using Runge Kutta Time Stepping Schemes," In *14th Fluid and Plasma Dynamics Conference*, Paper No. AIAA 81-1259.

Johnston, J. and M. Nishi, (1999) "Vortex Generator Jets - Means for Flow Separation Control," *AIAA Journal*, Vol. 28, No. 6, pp. 989–994.

Jurgens, H. M. and Zingg D. W., (1995) "Implementation of a High-Accuracy Finite-Difference Scheme for Linear Wave Phenomena," In *Proceedings of the International Conference on Spectral and High-Order Methods*, Vol. 95.

Kral, Linda D., John F. Donovan, Alan B. Cain and Andrew W. Cary, (1997) "Numerical Simulation of Synthetic Jet Actuators," In *4th Shear Flow Control Conference*, Paper No. AIAA 1997-1824.

Kreiss, H. O., (1970) "Initial Boundary Value Problem for Hyperbolic Systems," *Communications on Pure and Applied Mathematics*, Vol. 23, pp. 277–298.

Lake, J., (1999) "Flow Separation Prevention on a Turbine Blade in Cascade at

Low Reynolds Number," PhD Thesis, Air Force Institute of Technology, Wright-Patterson AFB, Ohio.

Lele, S., (1992) "Compact Finite Difference Schemes with Spectral-like Resolution," *Journal of Computational Physics*, Vol. 103, pp. 16–42.

Lindemuth, I. and J. Killeen, (1973) "Alternating Direction Implicit Techniques for Two-Dimensional Magnetohydrodynamics Calculations," *Journal of Computational Physics*, Vol. 13, pp. 181–208.

Lyall, E., P. King, R. Sondergaard, J. Clark and M. McQuilling, (2011) "An Investigation of Reynolds Lapse Rate for Highly Loaded Low Pressure Turbine Airfoils with Forward and Aft Loading," In *ASME Turbo Expo 2011*, Paper No. GT2011-46328.

Mayle, R.E., (1991) "The Role of Laminar-Turbulent Transition in Gas Turbine Engines," *ASME Journal of Turbomachinery*, Vol. 113, pp. 509–537.

McDonald, H. and W. R. Briley, (1975) "Three-Dimensional Supersonic Flow of a Viscous or Inviscid Gas," *Journal of Computational Physics*, Vol. 19, pp. 150–178.

McQuilling, M., (2007) "Design and Validation of a High-Lift Low-Pressure Turbine Blade," PhD Thesis, Wright State University, Fairborn, OH.

McQuilling, M., M. Wolff, S. Fonov, J. Crafton and R. Sondergaard, (2010) "Experimental Investigation of a High-Lift Low-Pressure Turbine Suction Surface," *AIAA Journal*, Vol. 48, No. 11, pp. 2465–2471.

Memory, C., K. Gompertz, Jen Ping Chen and J. Bons, (2010) "Numerical Simulations of Vortex Generating Jets on Low Pressure Turbine Blades," In *48th AIAA Aerospace Sciences Meeting*, Paper No. AIAA 2010-90.

Message Passing Interface Forum, (1994) "MPI: A Message-Passing Interface Standard," University of Tenessee, Computer Science Department, Technical Report: CS-94-230.

Murawski, C.G., T.W. Simon, R.J. Volino and K. Vafai, (1997) "Experimental Study of the Unsteady Aerodynamics in a Linear Cascade with Low Reynolds Number Low Pressure Turbine Blades," In *International Gas Turbine and Aeroengine Congress and Exhibition*, Paper No. 97-GT-95.

Murman, Scott M., Yehia M. Rizk and Lewis B. Schiff, (2000) "Coupled Numerical Simulation of the External and Engine Inlet Flows for the F-18 at Large Incidence," *Aircraft Design*, Vol. 3, pp. 65–77.

Poinsot, T. J. and S. K. Lele, (1992) "Boundary Conditions for Direct Simulations of Compressible Viscous Flows," *Journal of Computational Physics*, Vol. 101, pp. 104–129.

Poondru, S., (2007) "Large-Eddy Simulation and Active Flow Control of Low-Reynolds Number Flow through a Low-Pressure Turbine Cascade," PhD Thesis, University of Cincinnati, Cincinnati, Ohio.

Pope, Stephen B., (2000). *Turbulent Flows.* 1st ed. Cambridge University Press.

Praisner, T. and J. Clark, (2007) "Predicting Transition in Turbomachinery - Part I: A Review and New Model Development," *ASME Journal of Turbomachinery*, Vol. 129, pp. 1–13.

Prewitt, Nathan C., Davy M. Belk and Wei Shyy, (2000) "Parallel Computing of Overset Grids for Aerodynamic Problems with Moving Objects," *Progress in Aerospace Sciences*, Vol. 36, pp. 117–172.

Pulliam, T. H. and D. S. Chaussee, (1981) “A Diagonal Form of an Implicit Approximate-Factorization Algorithm,” *Journal of Computational Physics*, Vol. 39, No. 2, pp. 347–363.

Pulliam, T. H. and J. L. Steger, (1980) “Implicit Finite-Difference Simulations of Three-Dimensional Compressible Flow,” *AIAA Journal*, Vol. 18, No. 2, pp. 159–167.

Rivir, R., R. Sondergaard, J. Bons and J. Lake, (2000) “Passive and Active Control of Separation in Gas Turbines,” In *Fluids 2000*, Paper No. AIAA 2000-2235.

Rizzetta, D. and M. Visbal, (2002) “Application of Large-Eddy Simulation to Supersonic Compression Ramps,” *AIAA Journal*, Vol. 40, No. 8, pp. 1574–1581.

Rizzetta, D. and M. Visbal, (2003*a*) “Large-Eddy Simulation of Supersonic Cavity Flowfields Including Flow Control,” *AIAA Journal*, Vol. 41, No. 8, pp. 1452–1462.

Rizzetta, D. and M. Visbal, (2003*b*) “Numerical Investigation of Transitional Flow Through a Low-Presure Turbine Cascade,” In *33rd AIAA Fluid Dynamics Conference and Exhibit*, Paper No. AIAA 2003-3587.

Rizzetta, D. and M. Visbal, (2005) “Numerical Simulation of Separation Control for Transitional Highly-Loaded Turbine Blades,” *AIAA Journal*, Vol. 43, No. 9, pp. 1958–1967.

Rizzetta, D., M. Visbal and D. Gaitonde, (2001) “Large-Eddy Simulation of Supersonic Compression-Ramp Flow by High-Order Method,” *AIAA Journal*, Vol. 39, No. 12, pp. 2283–2292.

Rizzetta, D., M. Visbal and G. Blaisdell, (2003) “A Time-Implicit High-Order Compact Differencing and Filtering Scheme for Large-Eddy Simulation,” *International Journal for Numerical Methods in Fluids*, Vol. 42, No. 6, pp. 665–693.

Rizzetta, D., M. Visbal and M. Stanek, (1999) "Numerical Investigation of Synthetic-Jet Flowfields," *AIAA Journal*, Vol. 37, No. 8, pp. 919–927.

Rogers, S., N. Suhs and W. Dietz, (2003) "PEGASUS 5: An Automated Perprocessor for Overset-Grid Computational Fluid Dynamics," *AIAA Journal*, Vol. 41, No. 6, pp. 1037–1045.

Saravanamuttoo, H., G. Rogers, H. Cohen and Straznicky P., (2009). *Gas Turbine Theory.* Pearson Education Limited.

Sharma, O., R. Ni and S. Tanrikut, (1994) "Unsteady Flow in Turbines," In *AGARD Lecture Series 195*, Paper No. AGARD-LS-195.

Sherer, S., M. Visbal and M. Galbraith, (2006) "Automated Perprocessing Tools for Use with a High-Order Overset-Grid Algorithm," In *44th AIAA Aerospace Sciences Meeting and Exhibit*, Paper No. AIAA 2006-1147.

Smagorinsky, J., (1963) "General Circulation Experiments with the Primitive Equations," *Monthly Weather Review*, Vol. 91, No. 3, pp. 99–164.

Sondergaard, R., (2008) "LPT Flow Control at AFRL," In *38th Fluid Dynamics Conference and Exhibit*, Paper No. AIAA 2008-4156.

Sondergaard, R., R. Rivir and J. Bons, (2002) "Control of Low-Pressure Turbine Separation Using Vortex-Generator Jets," *Journal of Propulsion and Power*, Vol. 18, No. 4, pp. 889–895.

Sondergaard, Rolf, (2012) "Private Communication".

Steger, J., (1978) "Implicit Finite-Difference Simulation of Flow about Arbitrary Two-Dimensional Geometries," *AIAA Journal*, Vol. 16, No. 7, pp. 679–686.

Steger, Joseph L, F Carroll Dougherty and John A Benek, (1983) "A Chimera Grid Scheme," In *Advances in Grid Generation; Proceedings of the Applied Mechanics, Bioengineering, and Fluids Engineering Conference*, pp. 59–69.

Tannehill, John C., Dale A. Anderson and Richard H. Pletcher, (1997). *Computational Fluid Mechanics and Heat Transfer*. 2nd ed. Taylor and Francis.

Thomas, P. D. and C. K. Lombard, (1978) "Geometric Conservation Law and Its Application to Flow Computations on Moving Grids," *AIAA Journal*, Vol. 17, No. 10, pp. 1030–1037.

Thompson, Joe F., Z. U. A. Warsi and C. Wayne Mastin, (1985). *Numerical Grid Generation: Foundations and Applications*. North-Holland.

Towne, C. E., J. R. Schwab and T. T. Bui, (1993) "Proteus Two-Dimensional Navier-Stokes Computer Code - Version 2.0; Volume 1 - Analysis Description," National Aeronautics and Space Administration, Technical Report: NASA-TM-106336.

Vichnevetsky, R., (1974) "Numerical Filtering for Partial Differential Equations," Numerical Applications Memorandum, Technical Report: NAM 156.

Vinokur, M., (1989) "An Analysis of Finite-Difference and Finite-Volume Formulations of Conservation Laws," *Journal of Computational Physics*, Vol. 81, pp. 1–52.

Visbal, M. and D. Gaitonde, (1998) "High-Order Accurate Methods for Unsteady Vortical Flows on Curvilinear Meshes," In *36th AIAA Aerospace Sciences Meeting and Exhibit*, Paper No. 1998-131.

Visbal, M. and D. Gaitonde, (1999) "High-Order-Accurate Methods for Complex Unsteady Subsonic Flows," *AIAA Journal*, Vol. 37, No. 10, pp. 1231–1239.

Visbal, M. and D. Gaitonde, (2001) "Very High-Order Spatially Implicit Scheme for Computational Acoustics on Curvilinear Meshes," *Journal of Computational Acoustics*, Vol. 9, No. 4, pp. 1259–1286.

Visbal, M. and D. Gaitonde, (2002) "On the Use of Higher-Order Finite-Difference Schemes on Curvilinear and Deforming Meshes," *Journal of Computational Physics*, Vol. 181, pp. 155–185.

Volino, R., (2003*a*) "Passive Flow Control on Low-Pressure Turbine Airfoils," *ASME Journal of Turbomachinery*, Vol. 125, pp. 754–764.

Volino, R., (2003*b*) "Separation Control on Low-Pressure Turbine Airfoils Using Synthetic Vortex Generator Jets," *ASME Journal of Turbomachinery*, Vol. 125, pp. 765–777.

Volino, R., (2008) "Separated Flow Measurements on a Highly Loaded Low-Pressure Turbine Airfoil," In *ASME Turbo Expo 2008: Power for Land, Sea, and Air*, Paper No. GT2008-51445.

Volino, R., (2010) "Separated Flow Measurements on a Highly Loaded Low-Pressure Turbine Airfoil," *ASME Journal of Turbomachinery*, Vol. 132, pp. 011007–1 – 011007–10.

Volino, R. and L. Hultgren, (2001) "Measurements in Separated and Transitional Boundary Layers Under Low-Pressure Turbine Airfoil Conditions," *ASME Journal of Turbomachinery*, Vol. 123, pp. 189–197.

Volino, R., O. Kartuzova and M. Ibrahim, (2009) "Experimental and Computational Investigations of Low-Pressure Turbine Separation Control using Vortex Generator Jets," In *ASME Turbo Expo 2009: Power for Land, Sea and Air*, Paper No. GT2009-59983.

Volino, R., O. Kartuzova and M. Ibrahim, (2011) “Separation Control on a Very High Lift Low Pressure Turbine Airfoil Using Pulsed Vortex Generator Jets,” *Journal of Turbomachinery*, Vol. 133, pp. 041021–1 – 041021–13.

VonHagen, William, (2011) “Private Communication”.

Weiss, A. and L. Fottner, (1995) “The Influence of Load Distribution on Secondary Flow in Straight Turbine Cascades,” *ASME Journal of Turbomachinery*, Vol. 117, pp. 133–141.

Wilson, D. G. and T. Korakianitis, (1998). *The Design of High-Efficiency Turbomachinery and Gas Turbines.* 2nd ed. Upper Saddle River, New Jersey Prentice Hall Inc.

Wisler, D., (1998) “The Technical and Economic Relevance of Understanding Boundary Layer Transition in Gas Turbine Engines,” In *Minnowbrook II 1997 Workshop on Boundary Layer Transition in Turbomachines*, Paper No. NASA/CP-1998-206958.

Zhang, X., M. Vera, H. Hodson and N. Harvey, (2006) “Separation and Transition Control on an Aft-Loaded Ultra-High-Lift LP Turbine Blade at Low Reynolds Numbers: Low-Speed Investigation,” *ASME Journal of Turbomachinery*, Vol. 128, pp. 517–527.